NAVAL POSTGRADUATE SCHOOL

MONTEREY, CALIFORNIA

THESIS

RESIDUAL-MEAN ANALYSIS OF THE AIR-SEA FLUXES AND ASSOCIATED OCEANIC MERIDIONAL OVERTURNING

by

Pierre-Yves Daré

December 2006

Thesis Co-advisors: Timour Radko
Qing Wang

Approved for public release; distribution is unlimited

THIS PAGE INTENTIONALLY LEFT BLANK

REPORT DOCUMENTATION PAGE		Form Approved OMB No. 0704-0188

1. AGENCY USE ONLY *(Leave blank)*	2. REPORT DATE December 2006	3. REPORT TYPE AND DATES COVERED Master's Thesis

4. TITLE AND SUBTITLE Residual-Mean Analysis of the Air-Sea Fluxes and Associated Oceanic Meridional Overturning	5. FUNDING NUMBERS
6. AUTHOR(S) Pierre-Yves Daré	
7. PERFORMING ORGANIZATION NAME(S) AND ADDRESS(ES) Naval Postgraduate School Monterey, CA 93943-5000	8. PERFORMING ORGANIZATION REPORT NUMBER
9. SPONSORING /MONITORING AGENCY NAME(S) AND ADDRESS(ES) N/A	10. SPONSORING/MONITORING AGENCY REPORT NUMBER

11. SUPPLEMENTARY NOTES The views expressed in this thesis are those of the author and do not reflect the official policy or position of the Department of Defense or the U.S. Government.

12a. DISTRIBUTION / AVAILABILITY STATEMENT Approved for public release; distribution is unlimited	12b. DISTRIBUTION CODE

13. ABSTRACT (maximum 200 words)

The dynamic response of the oceanic mixed-layer to the thermodynamic forcing at the sea surface is analyzed in order to describe the pattern of the oceanic meridional overturning. The technique proposed in this study is based on residual-mean theory, which takes into account the transport of buoyancy and tracers by transient eddies. From the observed air-sea density flux and mixed-layer density distributions, we estimate the two components of the Meridional Overturning Circulation (MOC) corresponding to the adiabatic (along-isopycnal) advection and the diabatic (cross-isopycnal) flux. Calculations are performed for the global ocean and, additionally, for each oceanic basin. The proposed method extends the Walin (1982) mass transformation theory, and permits, for the first time, assessment of the strength of the MOC adiabatic component from the sea surface data.

This study offers a statistical description of the atmospheric and oceanic databases and gives some suggestions for the choice of specific datasets. In particular, the two most reliable atmospheric climatology databases (ECMWF and NCEP/NCAR re-analyses) are compared, and the impact of their inaccuracies on the MOC calculations is evaluated.

14. SUBJECT TERMS Thermohaline Circulation, Meridional Overturning Circulation, Residual-Mean Theory, Air-Sea Fluxes, Surface Density Flux , Mixed-Layer Density, ECMWF, NCEP/NCAR	15. NUMBER OF PAGES 101
	16. PRICE CODE

17. SECURITY CLASSIFICATION OF REPORT	18. SECURITY CLASSIFICATION OF THIS PAGE	19. SECURITY CLASSIFICATION OF ABSTRACT	20. LIMITATION OF ABSTRACT
Unclassified	Unclassified	Unclassified	UL

NSN 7540-01-280-5500 Standard Form 298 (Rev. 2-89)
Prescribed by ANSI Std. 239-18

THIS PAGE INTENTIONALLY LEFT BLANK

Approved for public release; distribution is unlimited

RESIDUAL-MEAN ANALYSIS OF THE AIR-SEA FLUXES AND ASSOCIATED OCEANIC MERIDIONAL OVERTURNING

Pierre-Yves Daré
Lieutenant, French Navy
M.S., French Naval Academy, 2000

Submitted in partial fulfillment of the
requirements for the degrees of

MASTER OF SCIENCE IN PHYSICAL OCEANOGRAPHY
AND
MASTER OF SCIENCE IN METEOROLOGY

from the

NAVAL POSTGRADUATE SCHOOL
December 2006

Author: Pierre-Yves Daré

Approved by: Timour Radko
Thesis Co-Advisor

Qing Wang
Thesis Co-Advisor

Mary L. Batteen
Chairman, Department of Oceanography

Philip A. Durkee
Chairman, Department of Meteorology

THIS PAGE INTENTIONALLY LEFT BLANK

ABSTRACT

The dynamic response of the oceanic mixed-layer to the thermodynamic forcing at the sea surface is analyzed in order to describe the pattern of the oceanic meridional overturning. The technique proposed in this study is based on residual-mean theory, which takes into account the transport of buoyancy and tracers by transient eddies. From the observed air-sea density flux and mixed-layer density distributions, we estimate the two components of the Meridional Overturning Circulation (MOC) corresponding to the adiabatic (along-isopycnal) advection and the diabatic (cross-isopycnal) flux. Calculations are performed for the global ocean and, additionally, for each oceanic basin. The derived method extends the Walin (1982) water mass transformation theory, and permits, for the first time, assessment of the strength of the MOC adiabatic component from the sea surface data.

This study offers a statistical description of the atmospheric and oceanic databases and gives some suggestions for the choice of specific datasets. In particular, the two most reliable atmospheric climatology databases (ECMWF and NCEP/NCAR re-analyses) are compared, and the impact of their inaccuracies on the MOC calculations is evaluated.

The results presented in this paper are consistent with the pattern of the thermohaline circulation estimated from in-situ measurements and models. They also support the previous estimates of diapycnal volume flux by the Walin-type calculations. Furthermore, they suggest that the global thermohaline circulation is dominated by the adiabatic advection in the ocean interior.

One of the goals of the data analysis and numerical modeling effort is to explain the role of the mesoscale variability in the dynamic coupling of the ocean and the atmosphere. Properties of the ocean thermal fronts and eddies determine the Undersea Warfare (USW) tactics in the areas of high mesoscale activity, and therefore our efforts to predict their distribution and strength are directly related to the Navy research interests.

THIS PAGE INTENTIONALLY LEFT BLANK

TABLE OF CONTENTS

THIS PAGE INTENTIONALLY LEFT BLANK

LIST OF FIGURES

LIST OF TABLES

THIS PAGE INTENTIONALLY LEFT BLANK

ACKNOWLEDGMENTS

I would like to express my warm thanks to Dr. Timour Radko and Dr. Qing Wang for their continuous support, their advice, and the expertise they provided throughout the months I worked on my thesis. I would like also to thank them and the NPS faculty for the time and the knowledge they shared with me during the two years I have spent in Monterey. I am deeply grateful for the strong educational involvement of all the professors and their assistants, of the classes I attended.

My thanks are also addressed to all the NPS faculty members who offered some of their precious time for my thesis research. Among them, I would particularly emphasize my gratitude towards Chenwu Fan, Dr. Tom Murphree, Arlene Guest, Bob Creasey, Mike Cook, Dr. Robin Tokmakian, and Dr. Igor Kamenkovich.

Finally, I especially want to thank my beloved wife Sophie and son Baptiste, who have constantly supported me throughout my studies at the Naval Postgraduate School.

THIS PAGE INTENTIONALLY LEFT BLANK

I. INTRODUCTION

The ocean plays a major role in the climate system since it is the main absorber of solar energy and therefore constitutes the direct source of most of the energy in the atmosphere. Thus, a complete understanding of the complex interactions and feedbacks between the ocean and the atmosphere is essential for forecasting any climate variation.

The interconnections between the heat and moisture fluxes at the sea surface and the oceanic and atmospheric circulations determine the equilibrium state of the climate system. Of particular importance are the meridional transports of energy by winds and currents (wind- and density-driven). As a consequence, fluctuations in the density-driven oceanic Meridional Overturning Circulation (MOC), also referred to as thermohaline circulation, may lead to major climate variations. The MOC has recently become a subject of great interest in the context of the currently observed global warming in polar regions.

One of the biggest uncertainties in the theory of the MOC is associated with the relative importance of the interior mixing and the adiabatic advection for its establishment and maintenance. The classical theories use purely diffusive models to depict the thermohaline circulation: Stommel (1961) emphasized the importance of the thermodynamic forcing on the individual density components, and Munk (1966) described the vertical mixing as the means for communicating the buoyancy anomaly from the surface into the ocean interior. Even more recent comprehensive discussions (Welander 1986, and Whitehead 1995) upheld such a description of the MOC.

However, several new theoretical and observational findings cast some doubt on the ability of these purely diffusive models to explain the magnitude and pattern of the meridional overturning. Indeed, although numerical simulations of the Atlantic exhibit a dependence of the MOC on diapycnal diffusivity (Bryan 1987, among others), most diffusive models have to rely on very high values of vertical mixing ($5-10\text{x}10^{-5} m^2 s^{-1}$) to reproduce oceanic overturning of realistic strength. Yet these high values are not supported by the microstructure and tracer dispersion measurements which instead suggest the thermocline diffusivity on the order of $1\text{x}10^{-5} m^2 s^{-1}$ (Ledwell et al. 1993;

Toole et al. 1994). This has led to an alternative adiabatic view of the meridional overturning, which emphasizes the importance of the advection along isopycnal surfaces, induced by wind forcing and eddy transfer (Toggvieler and Samuels 1998; Gnanadesikan 1999; Marshall and Radko 2003; Radko 2006). The relative importance of the interior mixing and adiabatic advection for the MOC establishment and maintenance has become the subject of a vigorous ongoing debate.

The classical representation of the MOC, shown in Fig. 1 and Fig. 2, focuses on the abyssal circulation driven by a few deepwater sources where deep convection occurs, and a large-scale upwelling that compensates for the localized downward flux (Stommel 1961). The modern theory of meridional overturning (Webb and Suginohara 2001; Bocaletti et al. 2005; among others) identifies and describes at least two distinct dynamic components of circulation, which are the shallow overturning cells in the main thermocline and the deep circulation in the abyssal ocean. In the abyssal regions, shielded from the direct influence of wind, small-scale mixing processes are necessary to re-supply the potential energy removed in the interior by the overturning and eddy-generating process (Wunsh and Ferrari 2004). On the other hand, the dynamics of the strongly stratified thermocline and the associated shallow overturning are controlled by the ventilation of water masses along the isopycnals that outcrop at the sea-surface (Luyten et al., 1983); therefore, the role of diapycnal mixing in the maintenance of the upper cell is questionable (Marshall et al. 2002). Indeed, unlike the abyssal regions, the thermocline is directly influenced by the surface winds, which provide the energy for the meridional overturning and make it possible to close the circulation even in the absence of vertical diffusion below the mixed-layer.

Traditional views on the oceanic overturning tended to emphasize the dynamics of the deep overturning circulation (Roemmich and Wunsh 1985; Munk and Wunsh 1998) and its major role in the meridional heat transport. However, the relative significance of the upper and deep circulation cells should be re-evaluated in the context of the recent suggestion (Boccaletti et al. 2005) that the meridional transport of heat is controlled by the processes operating in the upper ocean. In an attempt to meaningfully quantify partitioning of the oceanic heat flux between the deep and shallow overturning cells, these authors introduced the “heatfunction” which identifies the components of

circulation that effectively contribute to the total meridional heat flux. As shown in Fig. 3, diagnostics of a numerical model (Boccaletti et al. 2005) have pointed out that the heatfunction maxima are associated with a surface intensified flow largely limited to the central thermocline. This suggests that the meridional heat transport is dominated by the contribution from the upper branch of the MOC, the dynamics of which are still poorly understood (Samelson 2004).

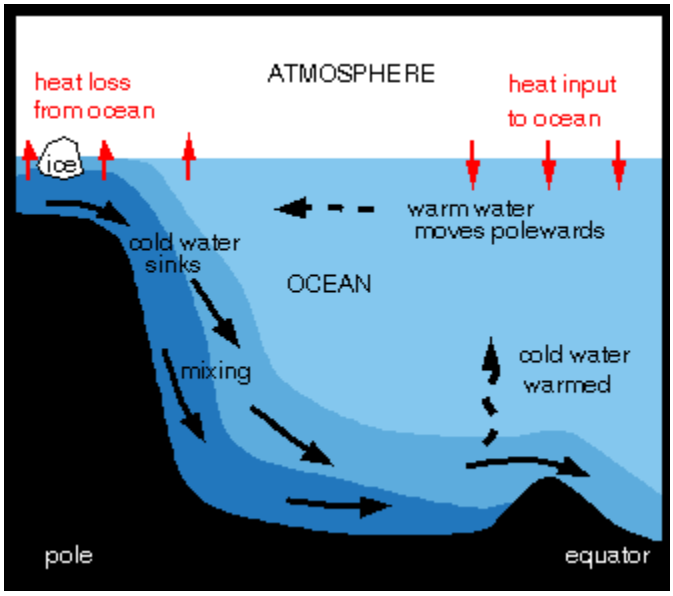

Figure 1. Schematic of the MOC (from *http://www.liv.ac.uk/physocean/research.htm*).

Although the global characteristics of the oceanic overturning can be estimated from the air-sea fluxes (Trenberth and Caron 2001), the vertical pattern of the MOC is difficult to reconstruct from observations or models. Sparse oceanographic measurements allow only a crude partitioning of the MOC in terms of the volume fluxes in the shallow, intermediate, and deep waters (Talley 2003). All numerical modeling studies rely on the assumed parameterizations of diapycnal fluxes, and the magnitude and functional dependencies of these fluxes are still a greatest source of uncertainty. This difficulty, for instance, precludes a reliable quantitative estimate of the relative importance of the

adiabatic advection and cross-isopycnal diffusion for maintenance of the MOC. A successful approach in analyzing the meridional overturning was proposed by Walin (1982), who deduced the integrated rates of water mass transformation at isopycnal surfaces from the air-sea buoyancy fluxes and surface density data. Walin's technique was extended and applied to the Atlantic (Speer and Tziperman 1992; Donners et al. 2005) and the global ocean (Speer et al. 1995). The water mass transformation at a given buoyancy surface is directly linked to the cross-isopycnal mass flux (Tziperman, 1986), and this provides an estimate of the strength of the diapycnal (and therefore inherently diabatic) component of the oceanic circulation.

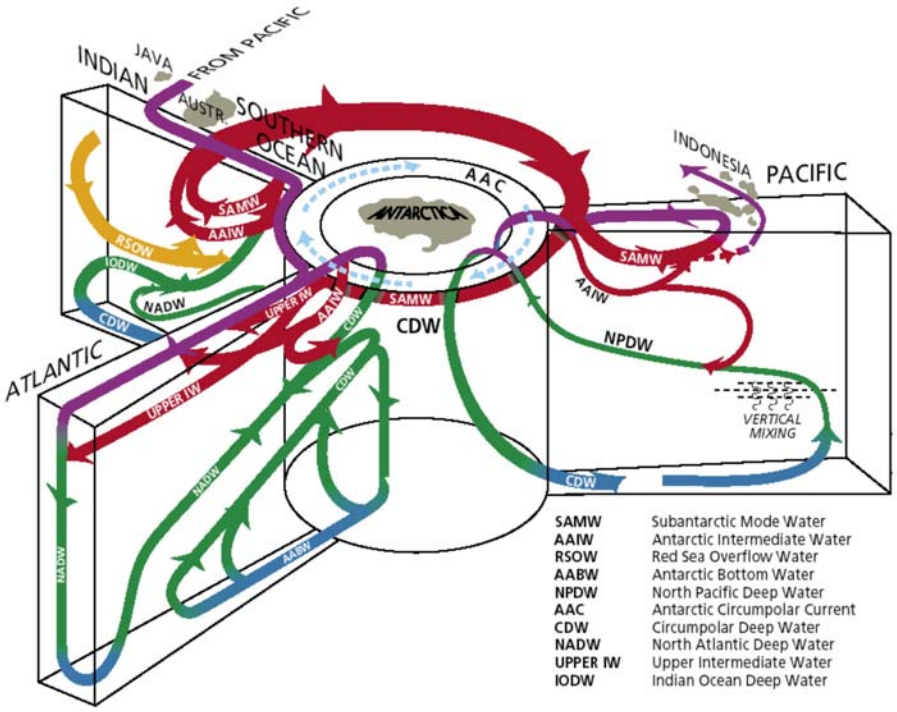

Figure 2. Classical representation of the global thermohaline circulation and its associated oceanic conveyor belt (from *Aguado and Burt, Understanding Weather and Climate).*

Assessing the adiabatic pole-to-pole component of the MOC is more challenging since the movement of fluid along the isopycnal surfaces does not significantly involve the interior water mass transformation. Another complication results from the presence of mesoscale eddies whose contribution to the overall overturning has to be taken into account. It is now widely accepted that the eddy transfer of buoyancy and tracers in the upper ocean is often comparable in magnitude to the advection by the time-mean flow (e.g. Radko and Marshall 2004; Henning and Vallis 2004). Since eddies generally tend to counteract the Eulerian transport, the residual flow (sum of the mean and eddy-induced circulations) is considerably different from the mean. Nevertheless, attempts have been made to diagnose the residual overturning circulation from the air-sea fluxes and surface buoyancy distribution (Speer et al. 2000; Karsten and Marshall 2002; Marshall and Radko 2003). These studies focused on the southern ocean, where predominantly zonal flow of the Antarctic Circumpolar Current justified the use of a simplified two-dimensional framework. A clear way of diagnosing the vertical structure of the global pole-to-pole MOC from the air-sea fluxes for complicated three-dimensional geometries of the isopycnals is still lacking.

The purpose of this study is to combine Walin's technique with the ideas of the residual circulation theory to quantify both the diabatic and the adiabatic components of the meridional overturning. More precisely, the along- and cross-isopycnal residual fluxes in the whole ocean and in each basin (Atlantic, Pacific, and Indian) will be estimated from the air-sea fluxes and mixed-layer buoyancy distribution. The technique presented here offers for the first time a quantitative assessment of the adiabatic component of the MOC which is based entirely on the sea surface data.

The coordinate system introduced in this study is somewhat similar to the isentropic framework often used by meteorologists. Here, however, the isentrope field cannot represent the density distribution, since the seawater potential density also depends significantly on salinity. In addition, contrary to the isentropic circulation, the thermodynamic forcing in this MOC model is restricted to the sea-surface and the associated oceanic boundary layer. The circulation in the ocean interior is assumed to be a linear response to mixed-layer dynamics induced by the air-sea fluxes.

The formulation of the diagnostic technique is presented in section II. Section III compares the different databases and suggests the choice of specific datasets. In section IV, the diagnostic model is applied to the global ocean and separately to the Atlantic, Pacific, and combined Indian-Pacific basins. Finally, the main results and the MOC characteristics are discussed in the conclusion (section V).

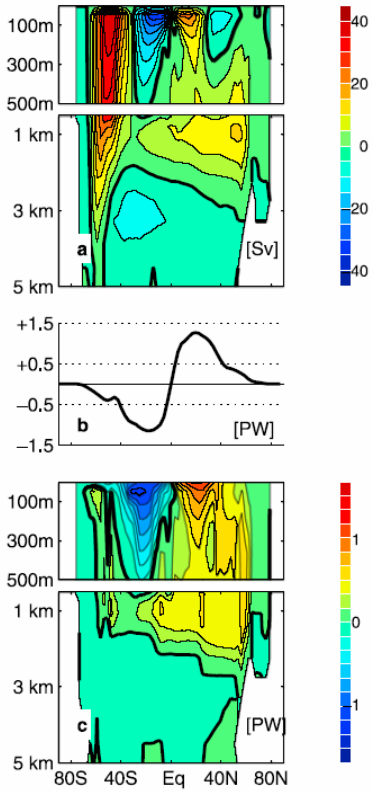

Figure 3. (a) Stream function related to the zonally-averaged flow inferred from the M.I.T. global circulation model. The distribution of meridional volume transport, given in Sv ($10^6 m^3 s^{-1}$), is defined by the stream function since seawater is nearly incompressible. Red shading corresponds to clockwise flow and blue to counter-clockwise flow. Contour interval is 5 Sv. (b) Zonal averages of the total heat transport of the global circulation model. (c) Meridional heat function in PW (10^{15} W) inferred from the global circulation model. Red shading corresponds to northward heat transport and blue to southward heat transport. Contour interval is 0.17 PW (from Boccaletti et al. 2005).

II. FORMULATION

The two surface properties used to reconstruct the large scale meridional overturning in the ocean are the mixed-layer density anomaly (σ_m) and the air-sea density flux (B). The dimensionless mixed-layer density anomaly (σ_m) is related to the mixed-layer density ρ_m (in $kg\ m^{-3}$) as follows:

$$\rho_m = 1000 + \sigma_m$$

And the sea surface density flux (B) is conventionally defined as:

$$B = -\frac{\alpha H}{C_p} + \beta \rho_0 \frac{(E-P)S}{1-S} \tag{1}$$

where (α, β) are the expansion/contraction coefficients of seawater, ρ_0 is the standard seawater density, H is the heat flux from the atmosphere into the ocean, E and P are the evaporation and precipitation rates, S is the salinity, and C_p is the specific heat capacity of water. The technique utilizes the observational data based on meteorological re-analysis (density flux at the sea surface) and Levitus database (seawater density) to reconstruct the pattern of the meridional overturning.

For the computations in the Atlantic, Pacific, and combined Indian-Pacific oceans, we consider the density range where all isopycnals are zonally bounded by land, as sketched in Fig. 4. Confining the analysis to these water masses greatly simplifies the interpretation of the diagnostic results and accurately describes the upper ocean. For the global ocean, computations are extended to the maximum value of mixed-layer density anomaly.

A. RESIDUAL FLUX AT THE BOTTOM OF THE MIXED-LAYER

It has been shown (Andrews and McIntyre 1976) that the distribution of density and tracers in the eddying flows cannot be given by only the Eulerian mean circulation, but the distribution also involves the eddy-induced advection, a process similar to the Stokes drift. Therefore, the starting point is the time-mean density equation that takes

into account the eddy fluxes as follows:

$$\vec{V} \cdot \nabla \sigma + \nabla(\overline{\vec{V}'\sigma'}) = \frac{\partial B}{\partial z} \tag{2}$$

where σ is the time-mean density anomaly, primes denote the perturbations from this mean due to transient eddies, and *B* represents the vertical density flux due to small-scale processes and air-sea fluxes. While we mostly associate the eddy fluxes with the mesoscale variability, it is convenient to include in it all transient processes, such as the effects of the seasonal cycle and variation in the mixed-layer depth.

The eddy fluxes in Eq. (2) can be broken down into two distinct components (Radko and Marshall 2006):

- The adiabatic advection by the eddy-induced velocity of the residual mean theory ($\vec{V}^*$), which is assumed to be non-divergent ($\nabla \cdot \vec{V}^* = 0$);

- The remaining diabatic component that can be written without loss of generality as the vertical convergence of the vertical flux $\left(-\frac{\partial B_{eddy}}{\partial z} \right)$.

As a result of this transformation, Eq. (2) becomes:

$$\vec{V}_{res} \cdot \nabla \sigma = \frac{\partial \tilde{B}}{\partial z} \tag{3}$$

where the residual velocity $\vec{V}_{res} = \vec{V} + \vec{V}^*$ represents the advection of density and tracers by both mean field and adiabatic eddies, and $\tilde{B} = B + B_{eddy}$ includes the diabatic effects of the small-scale mixing and eddies.

Following Marshall and Radko (2003), we separately discuss the dynamics of the thin, vertically homogeneous mixed-layer ($-h_m < z < 0$) and the stratified interior ($z < -h_m$). In the mixed-layer the residual buoyancy equation reduces to:

$$u_{res} \frac{\partial \sigma_m}{\partial x} + v_{res} \frac{\partial \sigma_m}{\partial y} = \frac{\partial \tilde{B}}{\partial z} \tag{4}$$

where σ_m is the mixed-layer density anomaly. Hence, the integration of Eq. (4) over the depth of the mixed-layer results in:

$$U\frac{\partial \sigma_m}{\partial x}+V\frac{\partial \sigma_m}{\partial y}=B_0+B_{mle}-\tilde{B}\Big|_{z=-h_m} \tag{5}$$

with $U=\int_{-h_m}^{0} u_{res}dz$, $V=\int_{-h_m}^{0} v_{res}dz$, B_0 being the air-sea density flux, B_{mle} a contribution from the diabatic eddies in the mixed-layer, and $\tilde{B}\Big|_{z=-h_m}$ the vertical density flux due to diabatic processes immediately below the mixed-layer.

In the mixed-layer buoyancy equation (5), the total density flux on the right-hand side is clearly dominated by the direct air-sea forcing B_0. The estimates in Radko and Marshall (2006), in the context of the ACC, suggest that the sea surface flux B_0 exceeds B_{mle} by an order of magnitude; the diabatic eddy fluxes play an even lower role on planetary scales (Radko 2006) that are the primary focus of this study. In addition, both small-scale mixing and the diabatic eddy effects are greatly reduced below the mixed-layer and therefore $B_0 >> \tilde{B}\Big|_{z=-h_m}$. Hence, Eq.(5) may be approximated by:

$$U\frac{\partial \sigma_m}{\partial x}+V\frac{\partial \sigma_m}{\partial y}=B_0 \tag{6}$$

The integration of the residual continuity equation over the depth of the mixed-layer, associated with the boundary condition that the vertical component of the residual velocity vanishes at the sea surface, leads to:

$$\frac{\partial U}{\partial x}+\frac{\partial V}{\partial y}=w_{res}\Big|_{z=-h_m} \tag{7}$$

For convenience, in following equations, $w_{res}\Big|_{z=-h_m}$ will be written as w_{res}.

The next step consists of introducing a convenient measure of the strength of the residual flow that enters (escapes) the mixed-layer at a given sea surface density range. Consider a thin strip of fluid bounded by two nearby isopycnal surfaces (σ and $\sigma+\Delta\sigma$) as indicated by the shaded area in the schematic in Fig. 4. The integral of w_{res} over this area (S) is defined by:

$$G(\sigma)=\iint_S w_{res}dS \tag{8}$$

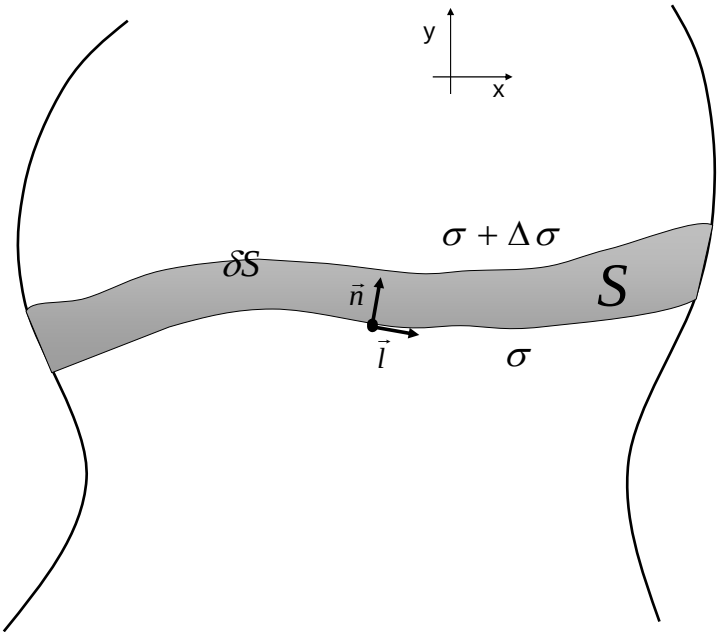

Figure 4. Schematic diagram illustrating the proposed diagnostic framework.

The area of integration in Eq. (8) extends from one intersection with the coastal boundary to another if the buoyancy contours are blocked by the land [see the schematic diagram in Fig. 4], and it otherwise may include contributions from several ocean basins. For closed surface density contours, for instance in the re-entrant Antarctic Circumpolar Current, the integral pertains to the entire area between contours σ and $\sigma + \Delta\sigma$.

The goal of the following derivation is to express G in terms of observed quantities. By using the relation between w_{res} and U and V provided in Eq. (7), and Green's theorem, the area integral $G(\sigma)$ can be expressed by:

$$G(\sigma) = \iint_S w_{res} dS = \iint_S \left(\frac{\partial U}{\partial x} + \frac{\partial V}{\partial y} \right) dS = \oint_{\partial S} (U dy - V dx) \tag{9}$$

where ∂S is the boundary of the region S. Note that the direction for the loop integral is counterclockwise.

Assuming no flux across the coastal boundaries for zonally blocked flows (or the exact cancellation of the zonal fluxes in case of a re-entrant flow), the integral in Eq. (9)

may be simplified to:

$$G(\sigma) = \int_{\sigma} (Udy - Vdx) - \int_{\sigma+\Delta\sigma} (Udy - Vdx) \tag{10}$$

where the integration along the isopycnals is in the positive *x*-direction.

By introducing the unit vector normal to the buoyancy contours $\vec{n} = \frac{\nabla \sigma_m}{|\nabla \sigma_m|}$, Eq. (10) can be conveniently rewritten:

$$G(\sigma) = \int_{\sigma+\Delta\sigma} \vec{U} \cdot \vec{n} \; dl - \int_{\sigma} \vec{U} \cdot \vec{n} \; dl \tag{11}$$

with $\vec{U} = (U, V)$ and l being the arc length along the mixed-layer density contours.[1]

Eq. (11) is readily interpreted as follows: the area-integrated vertical residual flux at the bottom of the mixed-layer in a steady state is equal to the sum of the lateral residual fluxes into this area. This statement is consistent with a simplified mass budget in the volume defined by the two isopycnal surfaces within the mixed-layer, as depicted by the schematic diagram in Fig. 5. This mass budget is here expressed as a simple volume budget since the density is almost constant within the considered volume and the contribution of evaporation/precipitation at the sea surface to the volume balance is neglected.

Taking the limit $\Delta\sigma \to 0$, Eq. (11) becomes:

$$G(\sigma) = \frac{\partial F}{\partial \sigma} \cdot \Delta\sigma \tag{12}$$

where

$$F(\sigma) = \int_{\sigma} \vec{U} \cdot \vec{n} \; dl \tag{13}$$

[1] While the schematic in Fig. 4 and the related discussion represents the case in which density increases northward (the configuration relevant for the Northern hemisphere), it can be readily shown that our formulation applies to both Northern and Southern hemispheres.

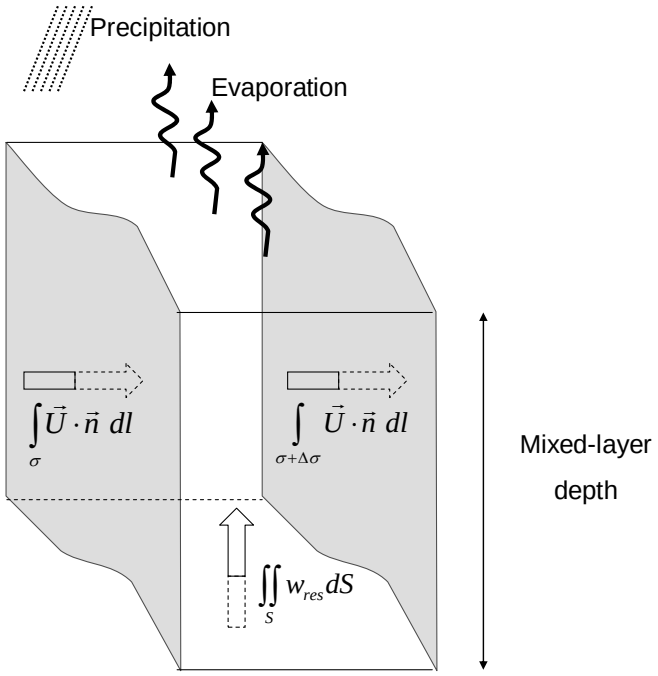

Figure 5. Physical interpretation of Eq. (11): mass budget in the volume delimited by the isopycnal surfaces σ and $\sigma + \Delta\sigma$ within the mixed-layer.

Eq. (6) may be written as $\vec{U} \cdot \vec{n} = \dfrac{B_0}{|\nabla \sigma_m|}$ and then substituted in Eq. (13) to obtain the following expression of *F*:

$$F(\sigma) = \int_{\sigma} \frac{B_0}{|\nabla \sigma_m|} dl \tag{14}$$

Since the air-sea fluxes and the sea surface density are easily accessible from data, the preceding analysis offers a simple procedure for estimating the total residual volume flux that enters (escapes) the mixed layer from (into) the ocean interior within the surface area $S(\sigma_1 < \sigma < \sigma_2)$ that is bounded by the two density contours σ_1 and σ_2 $(\sigma_2 > \sigma_1)$:

$$V(\sigma_1, \sigma_2) = \iint_{S(\sigma_1 < \sigma < \sigma_2)} w_{res} dS = \int_{\sigma_1}^{\sigma_2} \frac{G(\sigma)}{\Delta\sigma} d\sigma = F(\sigma_2) - F(\sigma_1) \tag{15}$$

where $F(\sigma)$ is given by Eq. (14).

B. ALTERNATIVE METHOD

Instead of computing $F(\sigma)$ along the ispopycnals σ_1 and σ_2, $V(\sigma_1,\sigma_2)$ may be obtained by an alternative method using the area integration over the surface bounded by two isopycnals. This alternative technique is similar to that in Walin's (1982) formulation.

By introducing the expression for *F* [Eq. (14)] into Eq. (11), we evaluate the vertical residual flow that enters (escapes) the mixed-layer over the area *S* (defined above and sketched in Fig. 4):

$$G(\sigma)=\iint_S w_{res}\,dS = F(\sigma+\Delta\sigma)-F(\sigma)=\int_{\sigma+\Delta\sigma}\frac{B_0}{|\nabla\sigma_m|}dl-\int_{\sigma}\frac{B_0}{|\nabla\sigma_m|}dl \tag{16}$$

Alternatively, Eq. (16) may be expressed as:

$$G(\sigma)=\frac{1}{\Delta\sigma}\left(\int_{\sigma+\Delta\sigma}B_0\frac{\Delta\sigma}{|\nabla\sigma_m|}dl-\int_{\sigma}B_0\frac{\Delta\sigma}{|\nabla\sigma_m|}dl\right)=\frac{1}{\Delta\sigma}\left(\int_{\sigma+\Delta\sigma}B_0 L dl-\int_{\sigma}B_0 L dl\right) \tag{17}$$

where $L=\dfrac{\Delta\sigma}{|\nabla\sigma_m|}$ is, approximately, the distance between the two isopycnal contours σ and $\sigma+\Delta\sigma$. Therefore, Eq. (17) becomes:

$$G(\sigma)\approx\frac{1}{\Delta\sigma}\left(\iint_S B_0(\sigma+\Delta\sigma)dS-\iint_S B_0(\sigma)dS\right) \tag{18}$$

Taking the limit $\Delta\sigma\to 0$, we arrive at:

$$G(\sigma)=\iint_S w_{res}\,dS\approx\frac{\partial^2}{\partial\sigma^2}\left(\iint_S B_0 dS\right).\Delta\sigma \tag{19}$$

and finally obtain the alternative expression for $V(\sigma_1,\sigma_2)$:

$$V(\sigma_1,\sigma_2)=\int_{\sigma_1}^{\sigma_2}\frac{G(\sigma)}{\Delta\sigma}d\sigma=\frac{\partial}{\partial\sigma}\left(\iint_{S(\sigma)}B_0 dS\right)\Bigg|_{\sigma=\sigma_2}-\frac{\partial}{\partial\sigma}\left(\iint_{S(\sigma)}B_0 dS\right)\Bigg|_{\sigma=\sigma_1} \tag{20}$$

where $S(\sigma)$ is the area bounded by the mixed-layer density contour $\sigma_m = \sigma$ and a reference isopycnal σ_0 located in the same hemisphere and verifying $\sigma_0 < \sigma$. Note that the exact value of that reference density does not affect Eq. (21); therefore, for convenience, we may define σ_0 as the minimum density with distinct non-intersecting northern and southern contours, as depicted in Fig. 6a.

The alternative method leads to the following expression for *F*:

$$F(\sigma) = \frac{\partial}{\partial \sigma} \iint_{S(\sigma)} B_0 dS \tag{21}$$

While this expression is identical to the water mass transformation function (Walin 1982), its role and interpretation in the model derived here are less conventional. First, we note that unlike Walin's model and its previous extensions, this formulation takes into account the volume transfer driven by the adiabatic component of mesoscale eddies. More importantly, in this study, function $F(\sigma)$ is defined [Eq. (13)] in terms of a horizontal volume flux in the mixed-layer crossing a given isopycnal surface σ. This connection makes it possible to calculate the net residual volume flux that escapes (enters) the mixed-layer from (into) the ocean interior within an area bounded by two density contours [Eq. (15) and Eq. (20)]. Walin (1982) did not separate the water mass transformation within the mixed-layer from that occurring in the ocean interior.

It is also essential to note that the foregoing model makes it possible to distinguish the density forcing in the Northern and Southern Hemispheres. On the contrary, the original Walin's formulation involved the total transformation at a given interior isopycnal surface, in which contributions from the air-sea density fluxes in both hemispheres were grouped together.

C. DIAPYCNAL VOLUME FLUX

As defined above, σ_0 denotes the minimum value of mixed-layer density for which the studied basin contains two non-intersecting isopycnal contours. As shown in Fig. 6a, for every $\sigma > \sigma_0$ there are two distinct values of F corresponding to the southern and northern density contours; these are denoted as $F_S(\sigma)$ and $F_N(\sigma)$ respectively.

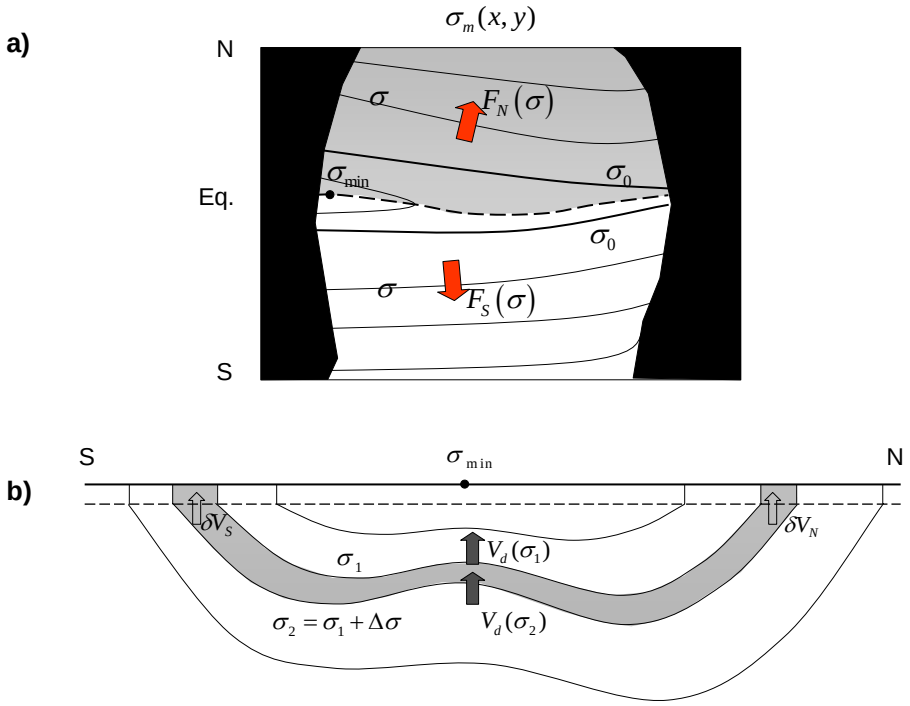

Figure 6. Schematic representation of the density structure in a zonally bounded ocean. (a) Mixed-layer density distribution. For each value of $\sigma > \sigma_0$ there are two non-intersecting contours of surface density; one in the northern part (indicated by the gray shading) and one in the southern part (not shaded). (b) The vertical meridional cross-section of density. The residual flux entering the density layer bounded by the isopycnals σ_1 and σ_2 from the mixed layer ($\delta V_S + \delta V_N$) is balanced by the diapycnal flux [$V_d(\sigma_2) - V_d(\sigma_1)$].

Since the residual flow is assumed to be non-divergent, the total residual flux (V_d) that crosses the isopycnal σ in the ocean interior (see the schematic in Fig. 6b) is exactly equal to the flux from the ocean interior into the mixed-layer within the area

defined by the condition $\sigma_m < \sigma$:

$$V_d(\sigma) = \iint\limits_{\sigma'<\sigma} G(\sigma')d\sigma' = F_S(\sigma) + F_N(\sigma) \qquad \text{for } \sigma > \sigma_0. \tag{22}$$

The sign convention in Fig. 6 is such that V_d is positive (negative) for an upward (downward) integrated flux across the isopycnal in the ocean interior.

D. ADIABATIC ADVECTION

The next step (and the key strength of the proposed technique) is to quantify the magnitude and pattern of the isopycnal pole-to-pole MOC component, caused by the adiabatic interior advection, from the surface data. For this, the residual volume flux entering (escaping) the mixed-layer from (into) the interior is computed separately in the Northern and Southern Hemispheres.

The highest value of potential density that can be found in the mixed-layer is denoted by $\sigma_{\max}$, and σ is an arbitrary value within the interval $[\sigma_0, \sigma_{\max}]$. For each hemisphere, Eq. (15) is used to express, in terms of F, the net residual flux at the bottom of the mixed-layer within a density range of $[\sigma, \sigma_{\max}]$, as follows:

$$\begin{cases} V_N(\sigma) = \iint\limits_{\substack{S(\sigma<\sigma'<\sigma_{\max}) \\ \text{north}}} w_{res}\,dS = F_N(\sigma_{\max}) - F_N(\sigma) \\ V_S(\sigma) = \iint\limits_{\substack{S(\sigma<\sigma'<\sigma_{\max}) \\ \text{south}}} w_{res}\,dS = F_S(\sigma_{\max}) - F_S(\sigma) \end{cases} \tag{23}$$

Since the residual flow is non-divergent, the sum of all fluxes entering the interior volume bounded by the isopycnals $\sigma_{\max}$ and σ is zero [see the schematic in Fig. 6b]:

$$V_d(\sigma_{\max}) - V_d(\sigma) - V_N(\sigma) - V_S(\sigma) = 0 \tag{24}$$

Note that in the absence of any cross-isopycnal flows, Eq. (21) would reduce to $V_N(\sigma) = -V_S(\sigma)$, which simply means that all the water subducted in the Southern (Northern) Hemisphere upwells in the Northern (Southern) one. In this case, the isopycnal flux throughout the density layer $[\sigma, \sigma_{\max}]$ is uniform and the adiabatic volume transport is $V_a(\sigma) = V_N(\sigma) = -V_S(\sigma)$.

However, in reality, the diapycnal flux across any isopycnal surface is not zero, and consequently $V_N(\sigma)$ is not equal to $V_S(\sigma)$. Therefore, the isopycnal flux cannot be precisely determined from V_S and V_N, and we need to define a way to assess the magnitude of V_a. It is reasonable to assume that representative values of V_a lie in between $V_N(\sigma)$ and $-V_S(\sigma)$. Thus, without any additional assumptions, the simplest and most consistent estimate of the isopycnal flux V_a within the density range $[\sigma, \sigma_{\max}]$ is given by the linear average of the two net residual fluxes at the bottom of the mixed-layer:

$$V_a(\sigma) = \frac{1}{2}\left[V_N(\sigma) - V_S(\sigma)\right] \tag{25}$$

Note that, with this definition, a positive value of V_a is associated with a downward residual flux at the base of the mixed layer in the Southern Hemisphere and its corresponding upward flux in the Northern Hemisphere. While this definition seems somewhat arbitrary at first sight, its application to the global overturning circulation model, described in section IV-D, indicates that it is surprisingly accurate in predicting the actual inter-hemispheric volume exchange.[2]

Since the length of the mixed-layer density contours inevitably reduces to zero as the value of density approaches its highest possible value ($\sigma \to \sigma_{\max}$), we may assume that $F_N(\sigma_{\max}) \approx F_S(\sigma_{\max}) \approx 0$ in Eq. (23), and therefore Eq. (25) reduces to:

$$V_a(\sigma) = \frac{1}{2}\left[F_S(\sigma) - F_N(\sigma)\right] \tag{26}$$

It is important to note that the expression above is most relevant for the case of a global ocean circulation. On the contrary, for computations within each basin, where we only consider the isopycnal contours zonally bounded by land, a better way to define V_S and V_N than that expressed in Eq. (23) may be:

[2] Note that σ in the preceding formulation cannot be less than σ_0, and therefore Eq. (25) does not describe the overturning in the upper tropical thermocline where $\sigma < \sigma_0$. However the region corresponding to this density range occupies only a small fraction of the thermocline, with a maximum depth of 200 m, and thus its relative contribution to the overall overturning is expected to be negligible.

$$\begin{cases} V_N(\sigma) = \iint\limits_{\substack{S(\sigma_0<\sigma'<\sigma) \\ \text{north}}} w_{res}\, dS = F_N(\sigma) - F_N(\sigma_0) \\ V_S(\sigma) = \iint\limits_{\substack{S(\sigma_0<\sigma'<\sigma) \\ \text{south}}} w_{res}\, dS = F_S(\sigma) - F_S(\sigma_0) \end{cases} \tag{27}$$

With this definition, the integration is carried out over the area defined by the mixed-layer density range $[\sigma_0, \sigma]$, which is more representative of the considered oceanic basin than the density interval $[\sigma, \sigma_{\max}]$. Moreover, with the alternative definition of V_S and V_N provided in Eq. (27), the adiabatic flux V_a defined in Eq. (25) now represents the isopycnal volume transport within the density range $[\sigma_0, \sigma]$.

E. ADIABATIC FLUX RATIO

$V_a(\sigma)$ in Eq. (26) represents the integrated isopycnal volume flux over the density interval $[\sigma, \sigma_{\max}]$. Therefore, the fraction of this adiabatic volume flux within the density layer $[\sigma, \sigma + \Delta\sigma]$ is $\left|\frac{\partial V_a}{\partial \sigma}\right| \Delta\sigma$, where $\Delta\sigma$ is the density increment.

One of the objectives of this study is to compare the diapycnal and isopycnal components of the overturning circulation, and some quantification of their relative strengths is obtained through the following parameter:

$$\gamma = \frac{\left\langle \frac{\partial V_a}{\partial \sigma} \right\rangle \Delta\sigma_m}{\langle V_d \rangle} \tag{28}$$

where $\left\langle \frac{\partial V_a}{\partial \sigma} \right\rangle = \underset{\sigma_0<\sigma<\sigma_{\max}}{rms} \left|\frac{\partial V_a}{\partial \sigma}\right|$, $\langle V_d \rangle = \underset{\sigma_0<\sigma<\sigma_{\max}}{rms} |V_d(\sigma)|$, and $\Delta\sigma_m = \sigma_{\max} - \sigma_0$.

Parameter γ is referred to hereafter as the adiabatic flux ratio. If $\gamma >> 1$, the interior flow is largely adiabatic, whereas $\gamma << 1$ indicates the importance of the interior diffusive processes for maintenance of the MOC.

F. EKMAN FLUX

As defined above, the residual flux includes the mean circulation and the eddy-contribution. The Ekman flux, which is generated by the mechanical forcing by the surface winds, dominates the lateral mean flux in the mixed-layer. Therefore, in regions where the eddy activity is weak, the residual flux may be almost equal to the Ekman flux.

In particular, the Ekman pumping velocity at the bottom of the Ekman layer is given by:

$$w_E = \frac{\partial}{\partial x}\left(\frac{\tau_{0y}}{\rho_0 f}\right) - \frac{\partial}{\partial y}\left(\frac{\tau_{0x}}{\rho_0 f}\right) = curl\left(\frac{\vec{\tau}}{\rho_0 f}\right) \tag{29}$$

where τ_{0x} and τ_{0y} are respectively the zonal and meridional components of the wind stress $\vec{\tau}$ at the sea surface, ρ_0 is the reference seawater density, and *f* is the Coriolis parameter.

In a similar way to the expression of the net residual flux at the bottom of the mixed-layer [Eq. (23)], we may define for each hemisphere the net Ekman flux at the bottom of the Ekman layer within a density range of $[\sigma, \sigma_{\max}]$, as follows:

$$\begin{cases} V_{N-EK}(\sigma) = \underset{\substack{S(\sigma<\sigma'<\sigma_{\max}) \\ \text{north}}}{\iint} w_E dS \\ V_{S-EK}(\sigma) = \underset{\substack{S(\sigma<\sigma'<\sigma_{\max}) \\ \text{south}}}{\iint} w_E dS \end{cases} \tag{30}$$

As mentioned in Section II-D, in the case of a specific oceanic basin, where only the isopycnal contours zonally bounded by the land are considered, we estimate the overturning circulation in the density range $[\sigma_0, \sigma]$. Therefore, the alternative expressions of the northern and southern Ekman fluxes are in this case:

$$\begin{cases} V_{N-EK}(\sigma) = \underset{\substack{S(\sigma_0<\sigma'<\sigma) \\ \text{north}}}{\iint} w_E dS \\ V_{S-EK}(\sigma) = \underset{\substack{S(\sigma_0<\sigma'<\sigma) \\ \text{south}}}{\iint} w_E dS \end{cases} \tag{31}$$

Finally, by analogy to the previous definitions relative to the residual flux, we may define the Ekman adiabatic advection (wind-driven component of V_a):

$$V_{a-EK}(\sigma) = \frac{1}{2}\left[V_{N-EK}(\sigma) - V_{S-EK}(\sigma)\right] \tag{32}$$

The comparison of $V_{a-EK}(\sigma)$ and $V_a(\sigma)$ allows us to assess the role of the wind stress in the establishment and maintenance of the MOC.

III. PARAMETER DEFINITION AND DATABASE DESCRIPTION

The technique described in the previous chapter offers a quantitative description of the two components (adiabatic and diapycnal) of the MOC based on sea surface observations. The next step consists of choosing the datasets in order to provide an accurate assessment of the oceanic overturning.

Since the MOC varies on time-scales which greatly exceed the typical scale of the air-sea fluxes (diurnal cycles), the model used in this study must rely on long-term means of observed parameters, and the computations carried out below use climatology datasets. This approach is consistent with the variability of the studied phenomena and secondly it allows the analysis of climate variations, which is one of the main motivations for studying the MOC.

The computations in this study use annual means for all quantities and it is essential, throughout the data description, to examine whether the climatology averages accurately represent the reality.

A. MIXED-LAYER DENSITY

1. Definition

One of the quantities used in the computation of the residual flux is the mixed-layer density anomaly (σ_m). The mixed-layer density is conceptually well-defined: the intense mixing within the mixed-layer (ML) makes the seawater density vertically uniform. Therefore, in the conceptual models, the density field at any depth above the pycnocline accurately represents the ML density distribution.

However, in reality, the annual-mean density is not vertically uniform in the mixed-layer and the choice of one particular depth to characterize the ML properties is not trivial. This choice is made more difficult by the large seasonal and spatial variability of the ML depth. Indeed, our theory uses a spatially uniform model of the mixed-layer depth for the computation of the density gradient that is needed in the calculation of the MOC components [Eq. (14)].

Fig. 7 shows the spatial distribution of the ML depth: the contours represent the annual means provided by the Levitus 94 climatology. This map indicates the large difference between the subtropical and polar regions. These differences are significantly reduced here because the plotted data are the annual averages and this filters out the seasonal variations. The observations in Fig. 7 suggest that the mixed-layer density can be approximated by the density at the sea surface. This idea is supported by the plot in Fig. 8, which gives the annually- and zonally-averaged ML depth with its temporal standard deviation computed over the monthly mean values.

On the other hand, as shown in Table 1, the temporal variations of density tend to significantly increase as the chosen depth is closer to the sea surface. Thus, in order for $\sigma(h)$ to accurately represent the mixed-layer density distribution throughout the year, we have to choose depth *h* large enough to have a low temporal standard deviation. Moreover, a deeper level within the ML is more relevant for describing the density layer of the MOC in the ocean interior.

Thus, a compromise must be found in order to select a depth which is almost always and everywhere within the mixed-layer and at which the density temporal variability is relatively low. The depth chosen for this study is 40 meters, based on Fig. 8 and Table 1. Note also that the 40 m depth is not within the ML only in the equatorial region and in the Arctic Ocean. The equatorial area is excluded from our analysis: we only consider regions where $\sigma > \sigma_0$ and the technique derived in the previous chapter does not describe the overturning in the upper tropical thermocline where $\sigma < \sigma_0$. Since the North Pole region is mostly covered by ice, the density forcing at the sea surface there will not be taken into account in our computations.

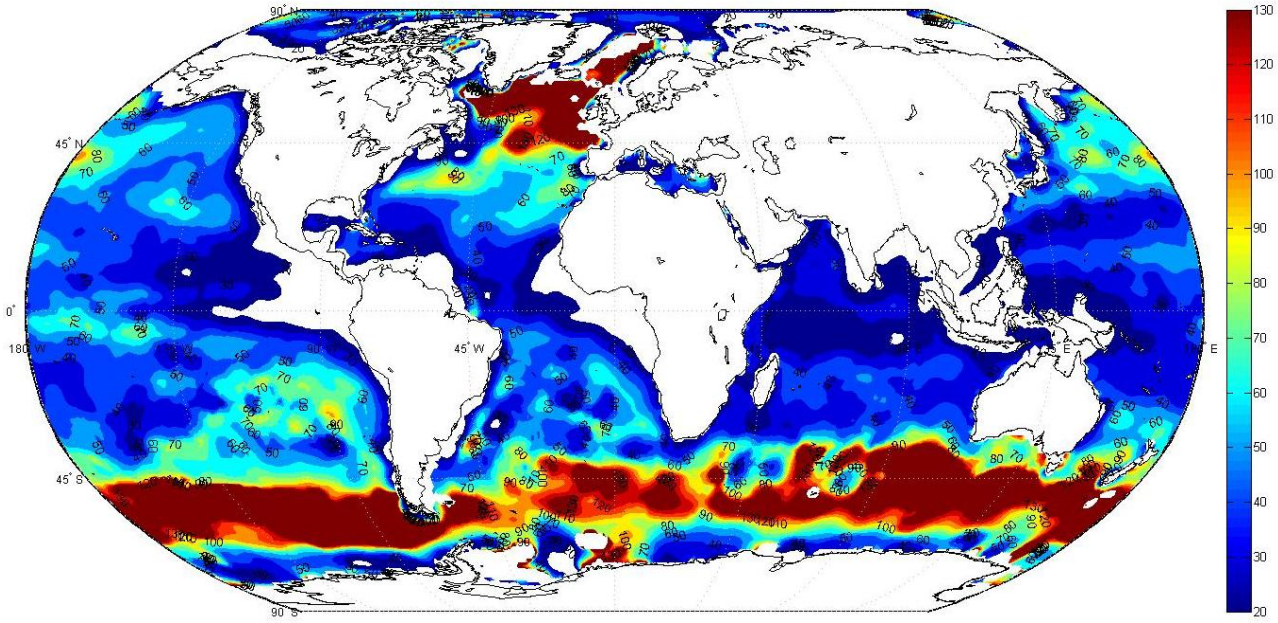

Figure 7. Annual mean of the oceanic mixed-layer depth given in meters and based on Levitus 94 climatology. White areas represent the continents and coastal regions where the mixed-layer depth is less than 20 m.

In order to more accurately represent the ML density, the small effect of the pressure on the density must be removed; hence, the potential density anomaly at 40 m is used for the computations. The potential density anomaly (σ_θ) is related to the potential density (ρ_θ in $kg\ m^{-3}$) as follows:

$$\rho_\theta = 1000 + \sigma_\theta$$

Note that using the potential density field to represent the ML density brings our analysis closer to the conceptual models of the mixed-layer, since this parameter has a lower vertical gradient than density.

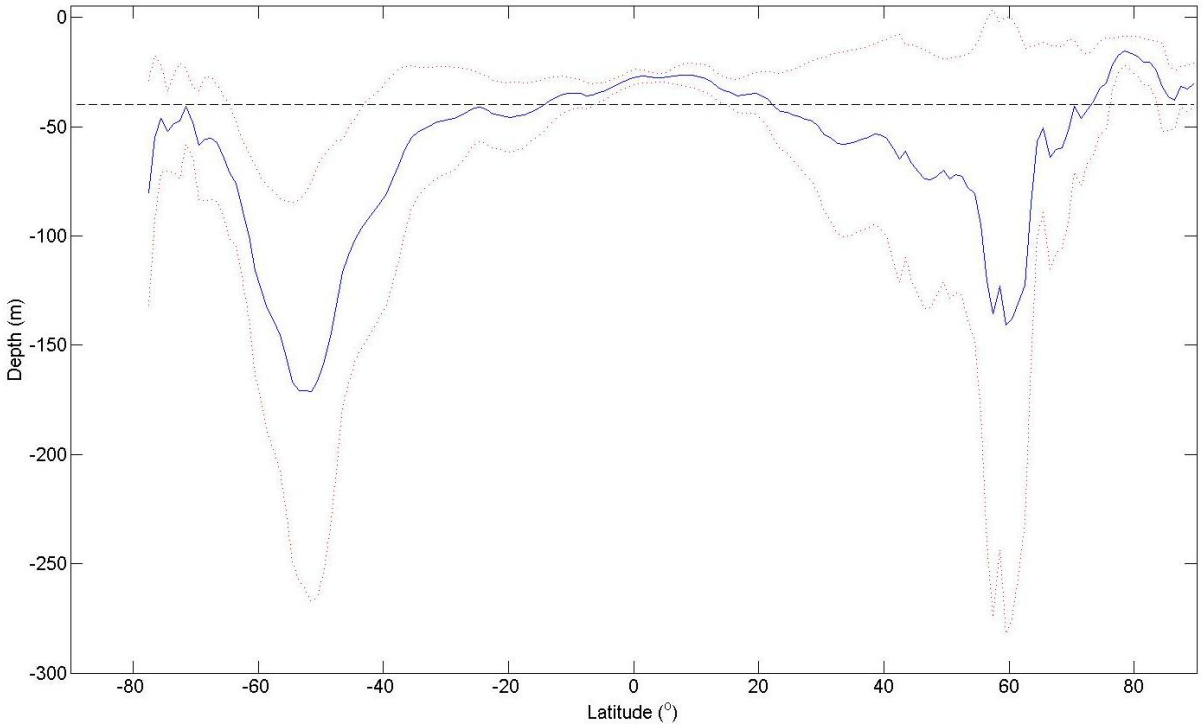

Figure 8. Annual mean and temporal standard deviation of the zonally-averaged mixed-layer depth. The plotted data are based on Levitus 94 climatology. The solid line indicates the zonally- and annually-averaged ML depth distribution and the dotted lines point out its temporal standard deviation computed from the monthly ML depth means. The dashed horizontal line highlights the 40 m depth.

Depth (m)	**Standard deviation of potential density** $\left(\mathbf{kg\ m^{-3}}\right)$
0 (surface)	4.7945
10	0.3995
20	0.3565
30	0.3184
40	0.2670
50	0.2403
75	0.1720
100	0.1349

Table 1. Mean temporal standard deviation of potential density at each characteristic depth of the mixed-layer. These statistical values are computed from the Levitus 94 monthly means of potential density at all grid points of the whole ocean.

2. Levitus Climatology

The oceanic database used in this study, for the potential density distribution at 40 m, as well as temperature and salinity needed in the calculations of the density flux at the sea surface, is Levitus 94 climatology. This database consists of a world atlas of objectively analyzed mean fields of major oceanic parameters at the annual, seasonal, and monthly time scales.

All the analyzed fields are offered on a one-degree latitude-longitude grid at selected standard depth levels from the sea surface to 5500 m depth. The standard levels relative to the ML are 0, 10, 20, 30, 50, 75, 100, 125, 150, 200, 250, and 300 meters. Therefore, for the 40 m potential density anomaly distribution, we have linearly interpolated the 30 m and 50 m analyzed fields.

The atlas datasets have been produced by the Ocean Climate Laboratory (OCL) at the National Oceanographic Data Center (NODC), which is supported by the National Oceanic and Atmospheric Administration (NOAA) Climate and Global Change program to provide quality controlled oceanographic databases. In particular, they include an objective analysis of all the in situ measurements for the period 1900-1992.

The Levitus climatology is considered by all oceanographers to be one of the most reliable databases for the oceanic parameters. It is accessible through the website http://iridl.ldeo.columbia.edu/SOURCES/.LEVITUS94 in NetCDF (Network Common Data Form) format.

3. Potential Density Field

The annual mean distribution of potential density anomaly at 40 meters $\left(\sigma_\theta\left(40m\right)\right)$ from Levitus 94 climatology is given in Fig. 9. The isopycnal contours σ_0 in both hemispheres are highlighted on the map. Based on the definition of σ_0 given in the previous chapter and the monthly mean fields of $\sigma_\theta\left(40m\right)$ [not shown here], the value of σ_0 has been estimated at $\sigma_0 = 24.2$. This value corresponds to the minimum potential density with distinct non-intersecting northern and southern contours over the whole ocean and throughout the year (i.e., on every chart of $\sigma_\theta\left(40m\right)$ monthly means).

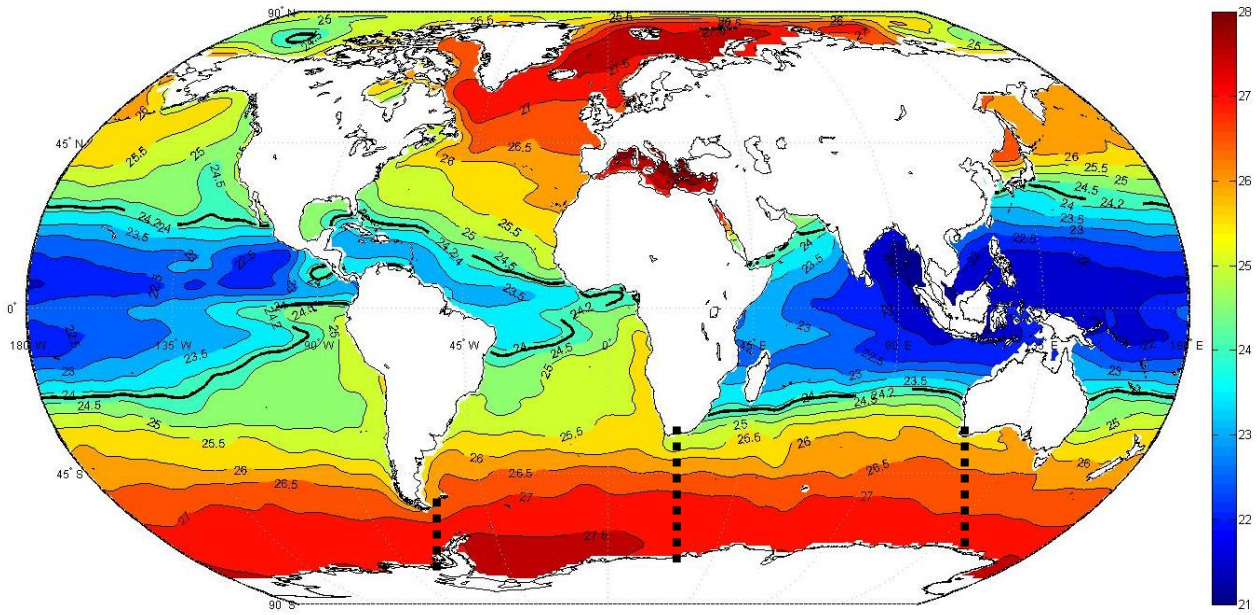

Figure 9. Annual mean distribution of potential density anomaly at 40 m depth. The dimensionless displayed data have been computed from Levitus 94 climatology. The thick solid lines point out the northern and southern contours of σ_0 $(\sigma_0 = 24.2)$. Dotted lines indicate partitioning of the world ocean into the individual basins.

B. DENSITY FLUX AT THE SEA SURFACE

1. Definition

The second surface quantity used in the computation of the residual flux is the air-sea density flux (B in $kg\ m^{-2}s^{-1}$). As shown previously in Eq. (1), this flux is composed of two terms, the thermal part (B_1) and the freshwater component (B_2):

$$B = -\frac{\alpha H}{C_p} + \beta\rho_0 \frac{(E-P)S}{1-S}$$

$$B_1 = -\frac{\alpha H}{C_p} \tag{33}$$

$$B_2 = \beta\rho_0 \frac{(E-P)S}{1-S} \tag{34}$$

Note that many studies dealing with fluxes at the sea surface refer to the buoyancy flux: this latter may be obtained from the density flux by simply multiplying *B* by the constant $-\frac{g}{\rho_0}$, with *g* being the gravity constant $\left(9.8\ m/s^2\right)$ and ρ_0 the standard seawater density $\left(1025\ kg\ m^{-3}\right)$. Indeed, buoyancy *b* is defined as $b=-\frac{g}{\rho_0}\rho$, where ρ is the seawater density.

The parameters C_p, α and β, which are, respectively, the specific heat capacity, the thermal and saline expansion/contraction coefficients of seawater, are not constant and depend on temperature, salinity, and pressure:

$$\begin{cases}\alpha=\alpha\left(T,S,p\right)\\ \beta=\beta\left(T,S,p\right)\\ C_p=C_p\left(T,S,p\right)\end{cases}$$

Therefore, the temperature (*T*) and salinity (*S*) distributions at the sea surface (where the hydrostatic pressure *p* is equal to 0), which are available in Levitus 94 climatology, will be used for determining the air-ocean density flux. The three coefficients are then calculated on the basis of the UNESCO algorithms for computation of fundamental properties of seawater (1983).

The heat flux from the atmosphere into the ocean (*H*), the evaporation (*E*) and precipitation (*P*) rates are obtainable in meteorological databases. In particular, the following fields may be found in the different climatological databases:

- Net solar energy flux at the sea surface $\left(Q_S\right)$;
- Net longwave radiation at the sea surface $\left(Q_L\right)$;
- Latent heat flux $\left(H_L\right)$;
- Sensible heat flux $\left(H_S\right)$;
- Total precipitation at the surface $\left(P\right)$, which is sometimes divided into two fields (large-scale and convective precipitation).

Note that, for the four thermal fluxes $\left(Q_S,Q_L,H_L,H_S\right)$, the convention used here associates positive values to upward fluxes (from the ocean into the atmosphere).

The five parameters described above allow us to compute the heat flux from the atmosphere into the ocean (H in $W\ m^{-2}$) and the evaporation and precipitation difference (E-P in $m\ s^{-1}$) field through the following equations:

$$H = -Q_S - Q_L - H_L - H_S \tag{35}$$

and

$$E - P = \frac{H_L}{\rho_0 L_e} - P \tag{36}$$

where L_e is the specific latent heat for evaporation $\left(L_e \approx 2.5\text{x}10^6\ J\ kg^{-1}\right)$.

2. Atmospheric Databases

Four different databases have been used to compute H and E-P. We compare their climatology and the corresponding predictions of the MOC components. This comparison answers two essential questions: the quality control of the results and their sensitivity to the observational fields.

- The **European Center for Medium-range Weather Forecast (ECMWF) Re-Analysis (ERA-40)** is a global analysis of many observations and satellite data streams for the period September 1957 through August 2002. This dataset contains 56 surface and single-level variables on an equally-spaced global 2.5 degree latitude-longitude grid, with all variables reported four times a day. In particular, the ERA-40 atlas, the web-version of which was released on 6 February 2006, describes the climate from 1979 through 2001, which is the period with the best and most time-consistent product quality for the entire globe. For this reason, this study uses monthly means of each parameter listed above from January 1979 through December 2001. The data may be downloaded from http://dss.ucar.edu/datasets/ds118.0. Note that the data are provided there in GRIB format (binary code for exchange of processed data).

- The **joint National Centers for Environmental Prediction (NCEP) and National Center for Atmospheric Research (NCAR) re-analysis** project has performed data assimilation using historical data from January 1948 to the present. Particularly, the NCEP-NCAR Climate Data Assimilation System 1 (NCEP-NCAR CDAS-1) provides monthly means of each needed parameter from

January 1949 up to the current month on an equally-spaced global latitude-longitude grid containing 94x192 points. In order to be consistent with the ECMWF climatology, we use the subsets from January 1979 through December 2001 in this study. These datasets may be obtained at http://iridl.ldeo.columbia.edu/SOURCES/.NOAA/.NCEP-NCAR/.CDAS-1 in NetCDF format (Network Common Data Form).

- The **Global Air-Sea heat and momentum flux Climatology from the Southampton Oceanography Centre (SOC-GASC97)** provides climatologic sea surface fluxes based on in situ reports within the COADS 1A (Comprehensive Ocean Atmosphere Dataset 1A), a global dataset containing of order 30 million surface observations from ships an buoys collected over the period 1980-1993. It is important to note that the quality of the fields is known for having a strong spatial dependence that reflects the global distribution of ship observations. Quality is likely to be high in the well-sampled North Atlantic and North Pacific oceans but, it decreases in the Southern Hemisphere. In particular, south of 40 S, the errors in the fields are likely to be large and the existence of spurious features, which have been generated during the objective analysis of the original raw distributions, must be pointed out. The data are available on an equally-spaced global one-degree latitude-longitude grid, in NetCDF format, at http://iridl.ldeo.columbia.edu/SOURCES/.SOC/.GASC97. The dataset documentation is accessible from this website.

- The **Da Silva atlas of Surface Marine Data 1994 (SMD94)** provides the monthly climatology of the near-surface atmospheric properties over the global ocean. Covering the period of January 1945 through December 1989, this database is made from individual observations in COADS 1A and an objective analysis using Barnes' weight function, which is the same response function used in Levitus 94 Climatology. It was produced at the University of Wisconsin-Milwaukee (UWM) by A. M. da Silva and C. C. Young in collaboration with S. Levitus from the National Oceanic and Atmospheric Administration (NOAA) / National Oceanographic Data Center (NODC). The datasets are available on an

equally-spaced global one-degree latitude-longitude grid, in NetCDF format, at http://iridl.ldeo.columbia.edu/SOURCES/.DASILVA/.SMD94. The dataset documentation is accessible from this website.

3. Distribution of the Density Flux at the Sea Surface

Based on Eqs. (1), (33), (34), (35), and (36), the density flux at the sea surface has been computed from each of the four databases. Figs. 10, 11, 12, and 13 show the density flux distributions respectively from ECMWF re-analysis, NCEP/NCAR re-analysis, SOC-GASC97, and DaSilva-SMD94 climatology. In each figure, the thermal and freshwater components (respectively B_1 and B_2) are also displayed.

Over most of the oceans, the density flux seems to be driven by thermal forcing. Figs. 10, 11, 12, and 13 show that the distributions of total density flux B and its thermal part B_1 look similar. Moreover, by looking at their magnitudes, we see that B_1 is generally the dominant part of B. This observation is supported by the zonal means of annually-averaged values that are given, respectively for each meteorological database, in Figs. 14, 15, 16, and 17.

Thus, from a global prospective, thermal forcing dominates the freshwater forcing and controls the density flux at the sea surface. However, as shown in Figs. 18, 19, 20, and 21, which provide the annually-averaged distribution of $\log\left(\frac{|B_1|}{|B_2|}\right)$ for each database, the zonal variability is large. In some places, especially in subtropical and polar regions, B_2 greatly exceeds B_1. These observations become more critical when we consider seasonal fields [not shown here].

Figs. 10, 11, 12, and 13 show the same regions of high density flux: these are in general the Western Boundary Currents (WBC) and the equatorial band. Indeed, in the regions of the warm Gulf Stream, Kuroshio Current, Agulhas Current, and East Australian Current, the heat loss by the ocean into the atmosphere is large, which causes the upper ocean to gain density. These currents advect heat from the tropics towards the poles, and energy exchanges with the atmosphere occur in their paths.

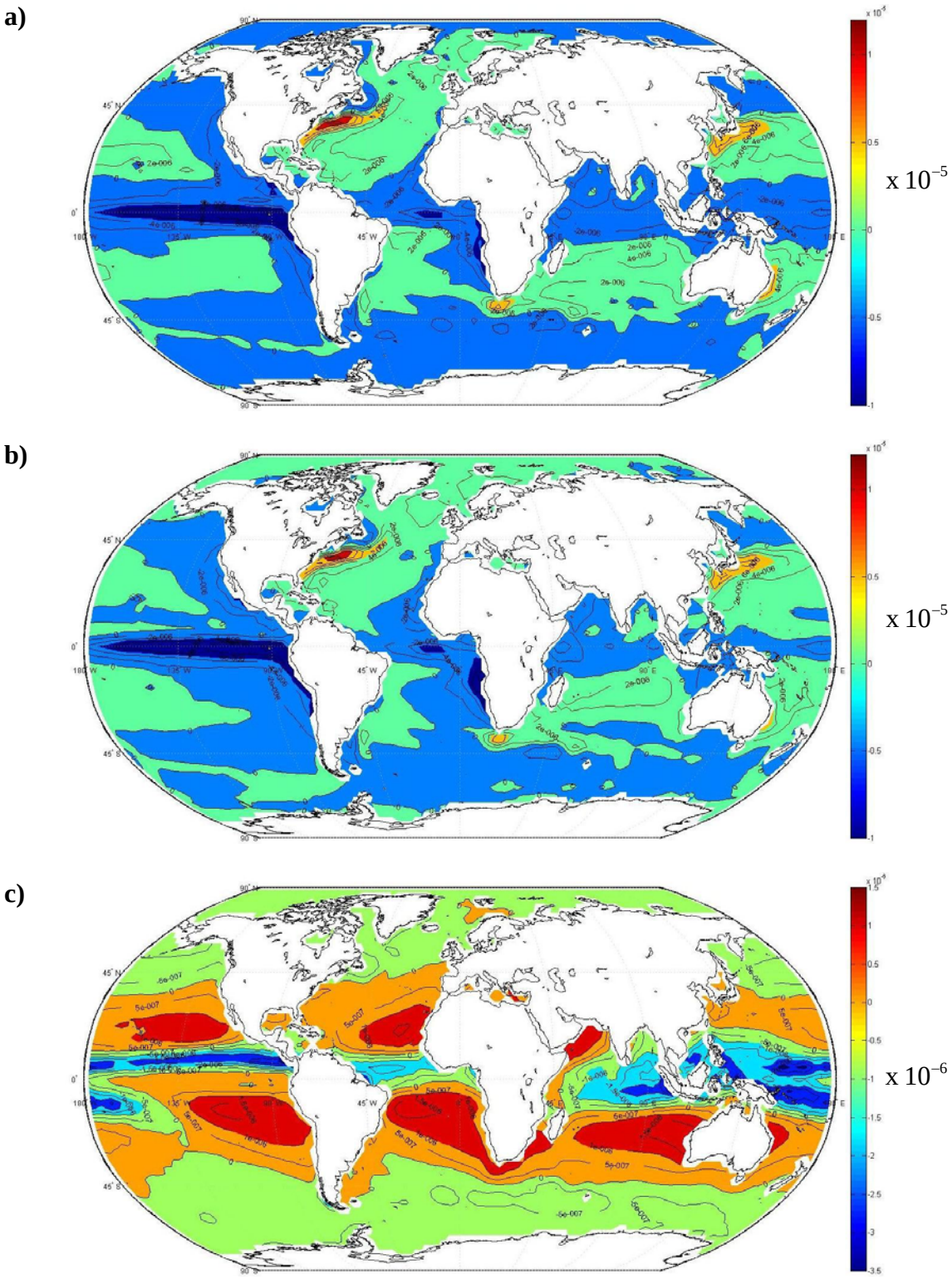

Figure 10. Sea surface density flux from ECMWF climatology. Positive values correspond to density gain by the ocean. The displayed values are in $kg\ m^{-2}s^{-1}$ (a) Total density flux B (b) Thermal component B_1 (c) Freshwater component B_2.

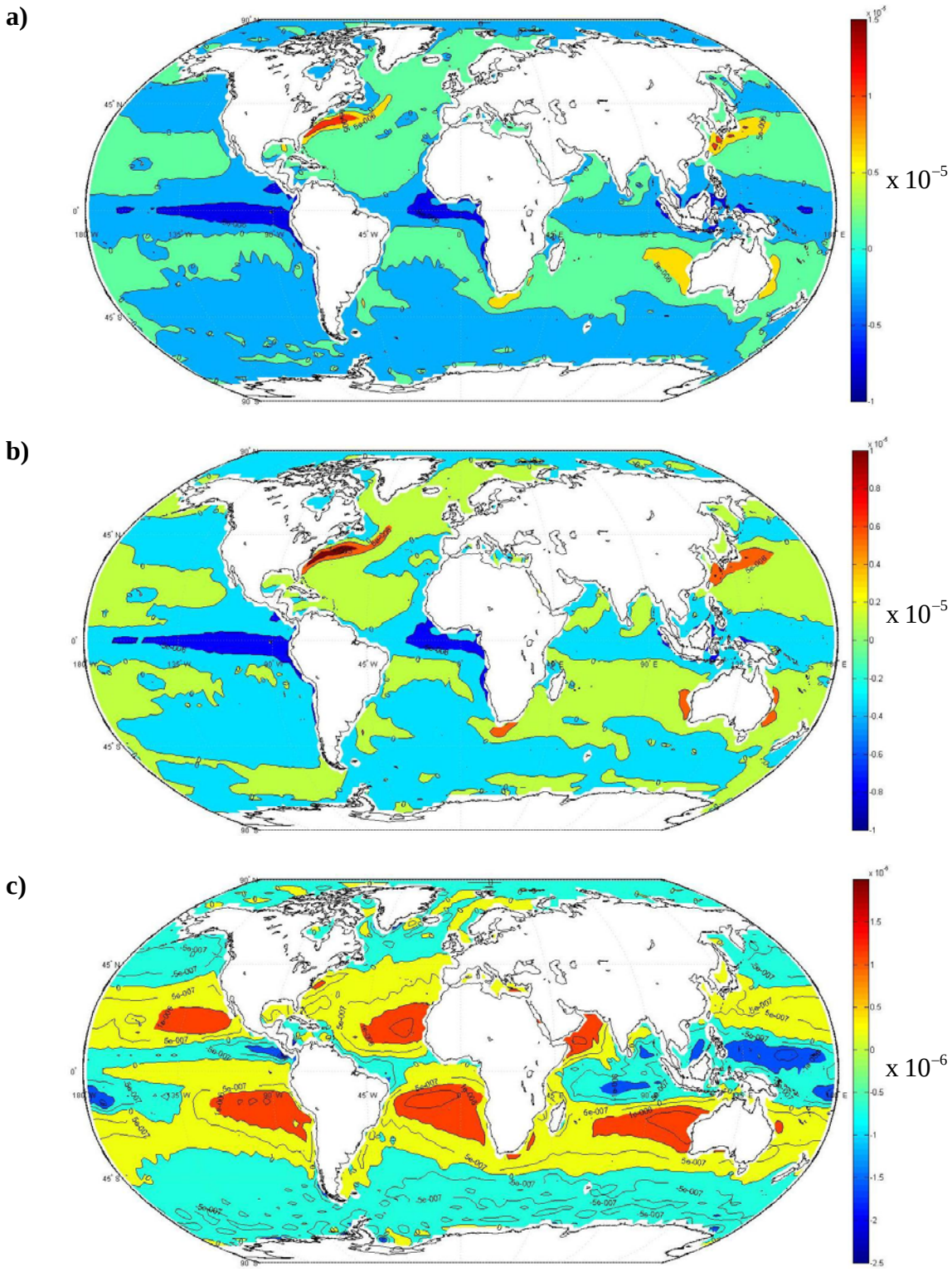

Figure 11. Same as Fig. 10, but from NCEP/NCAR re-analysis (same period as ECMWF climatology: 1979-2001).

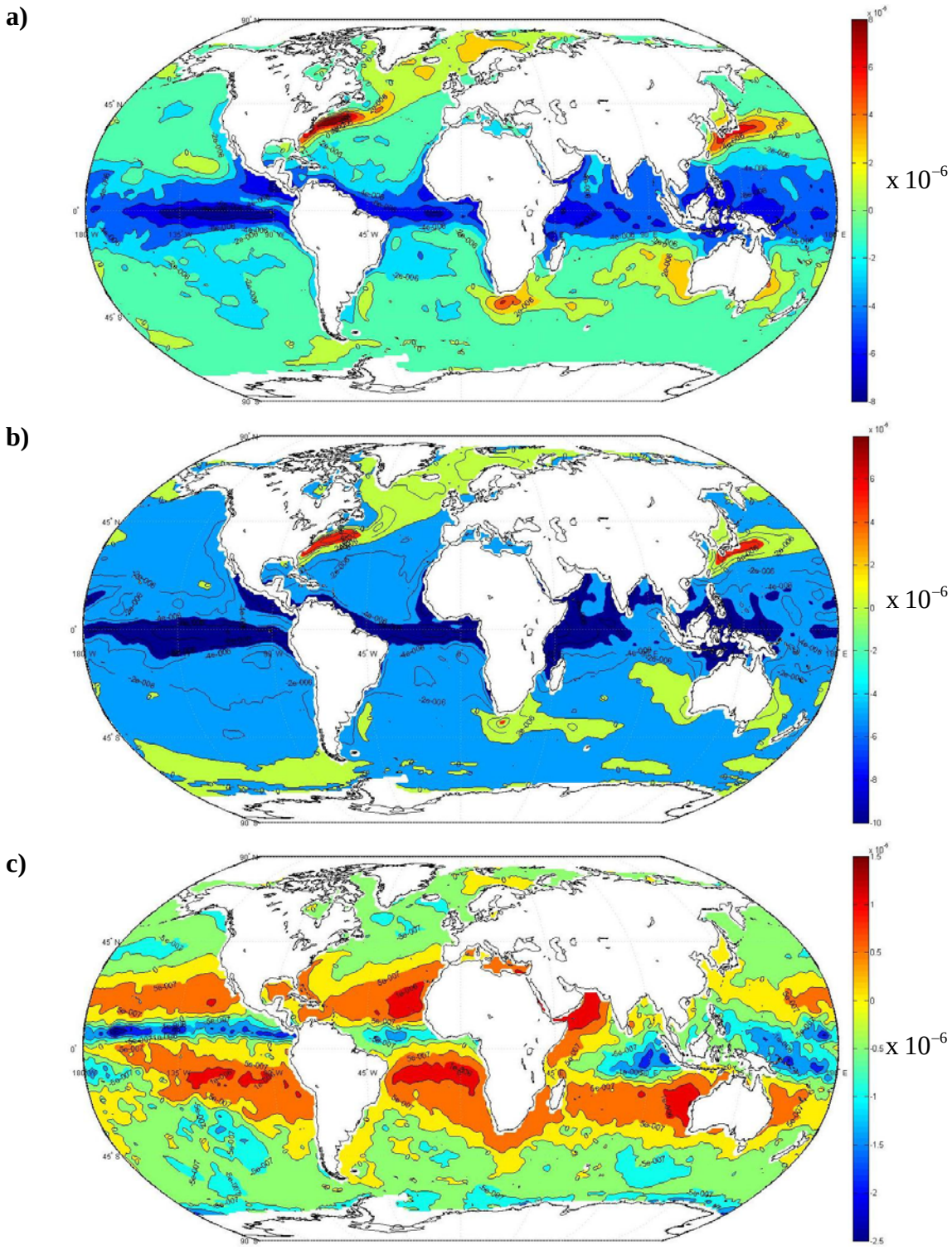

Figure 12. Same as Fig. 10, but from SOC-GASC97 climatology (period: 1980-1993).

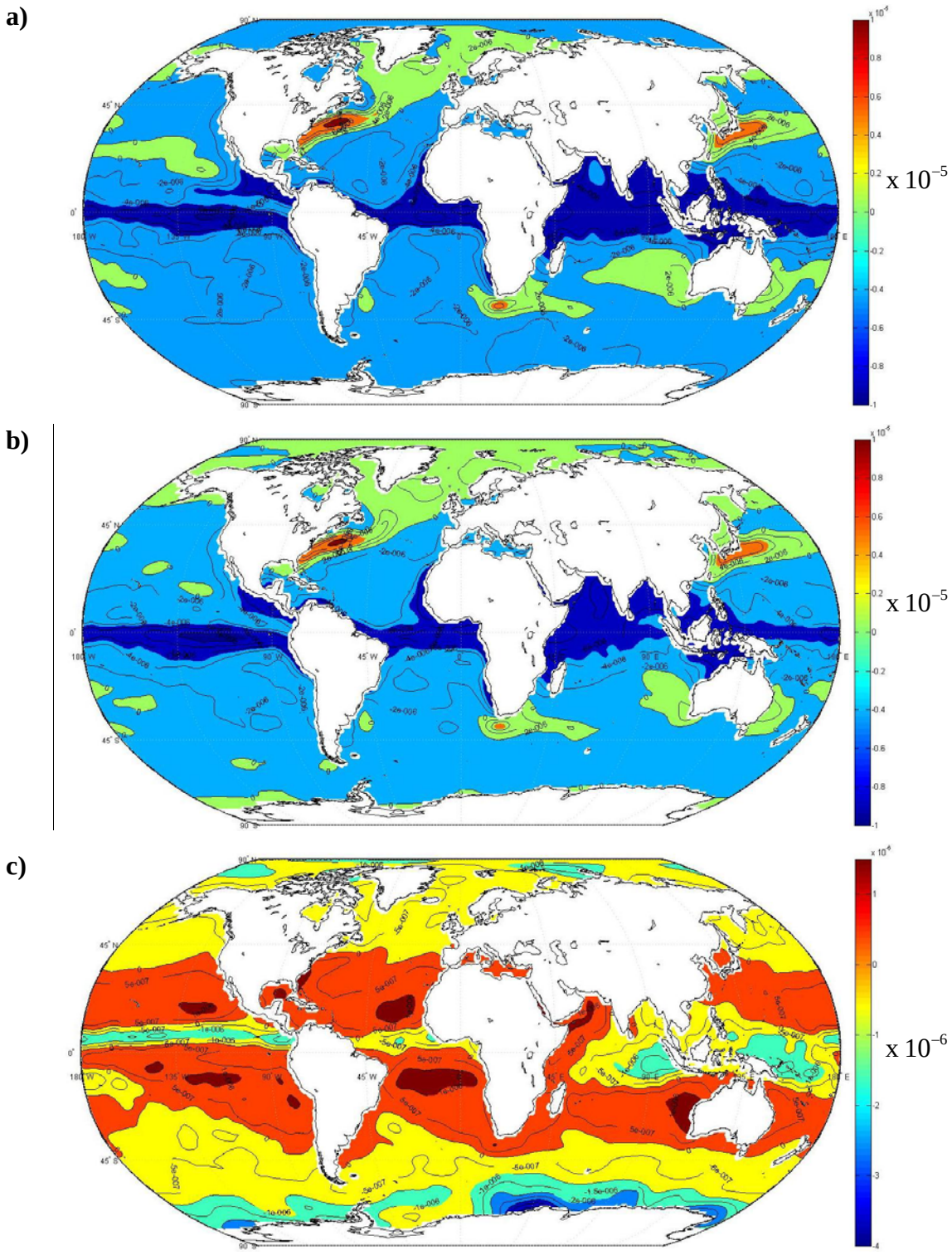

Figure 13. Same as Fig. 10, but from DaSilva-SMD94 climatology (period: 1945-1989).

Along the equator, the upwelling induced by the Ekman divergence brings cold water to the upper ocean and leads to vigorous downward heat fluxes from the warm tropical air above the surface. The negative oceanic density flux, caused by thermal forcing, is enhanced by the large precipitation within the Inter-Tropical Convergence Zone (ITCZ) band, which is, on average, centered on the equator.

Concerning the freshwater contribution, the large evaporation and the weak precipitation in subtropical regions generates a strongly positive contribution to the density flux at the surface. These regions are characterized by high sea-level pressure and persistent coverage of low-level non-precipitating clouds. On the other hand, over the equatorial band (mean position of the ITCZ) and in the sub-polar areas, precipitation is greater than evaporation, resulting in negative oceanic density flux.

The four databases considered in this study provide the same overall picture of the surface density flux distribution. However, significant quantitative differences are noted in some regions for the density flux components B_1 and B_2.

It is generally agreed that ECMWF and NCEP/NCAR are the two most reliable among these four climatologic databases. A number of studies have compared these two re-analysis datasets, and many of them (for instance, Bromwich and Fogt 2004) have suggested that ERA-40 seems to have better skills than NCEP/NCAR regarding analyzed fields after 1978 (the beginning of the modern satellite era). This may be explained by a better assimilation of satellite data within ECMWF than in NCEP/NCAR, which is largely constrained by the station observational network. Thus, ECMWF is particularly useful for the high latitudes.

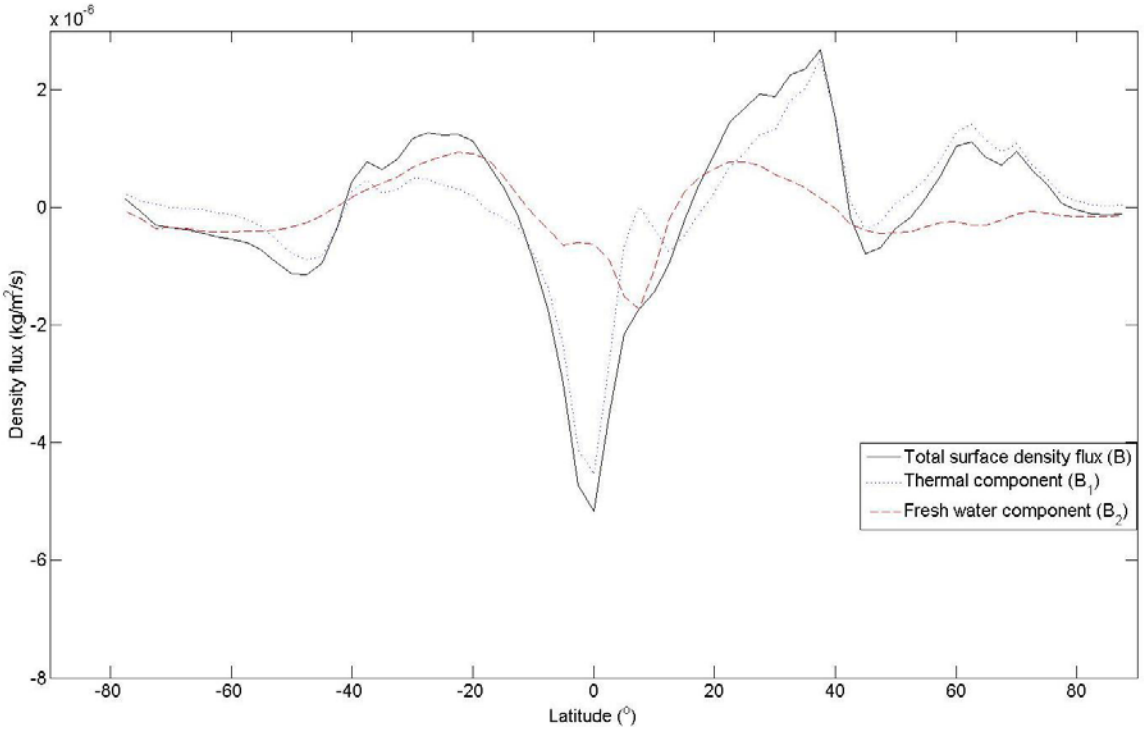

Figure 14. Zonal means of annually-averaged density flux B at the sea surface and of its two components B_1 and B_2 from ECMWF climatology (1979-2001).

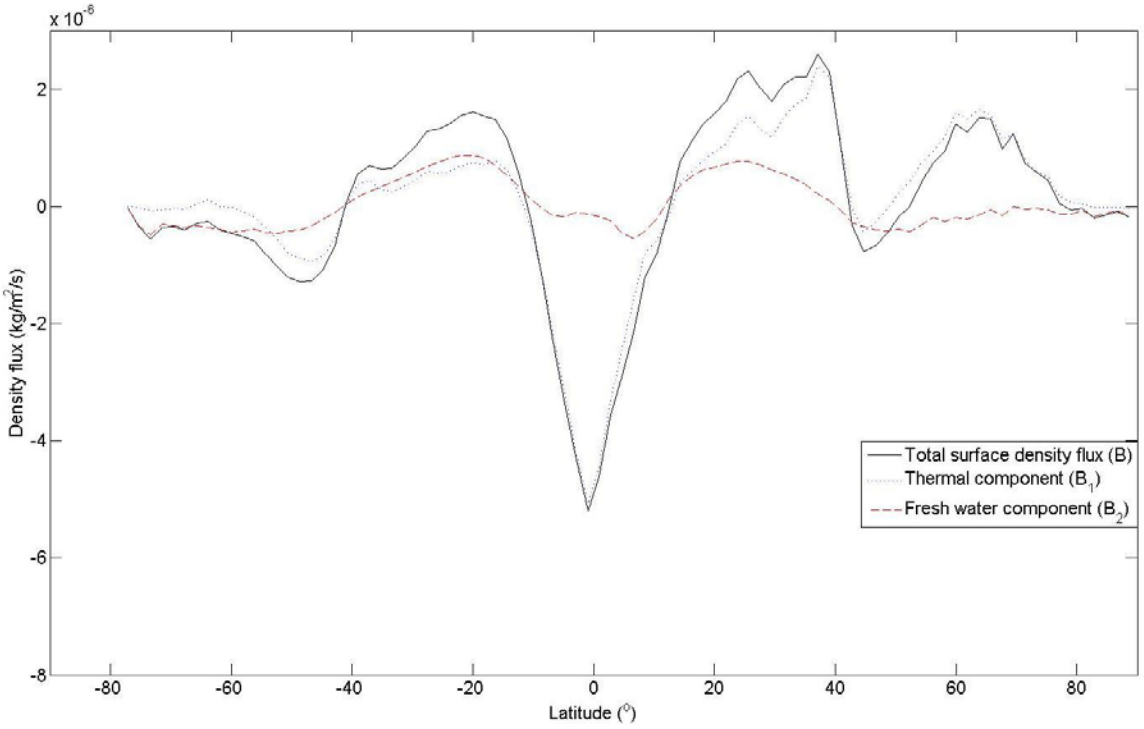

Figure 15. Same as Fig. 14, but from NCEP/NCAR re-analysis (1979-2001).

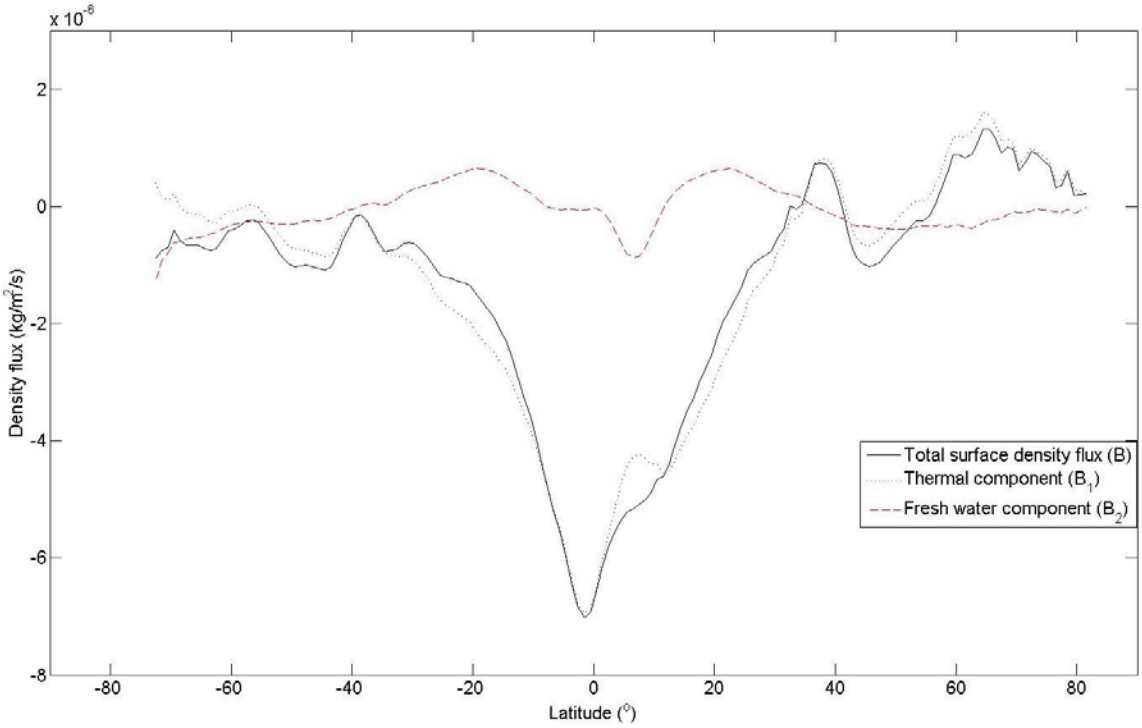

Figure 16. Same as Fig. 14, but from SOC-GASC97 climatology (period: 1980-1993).

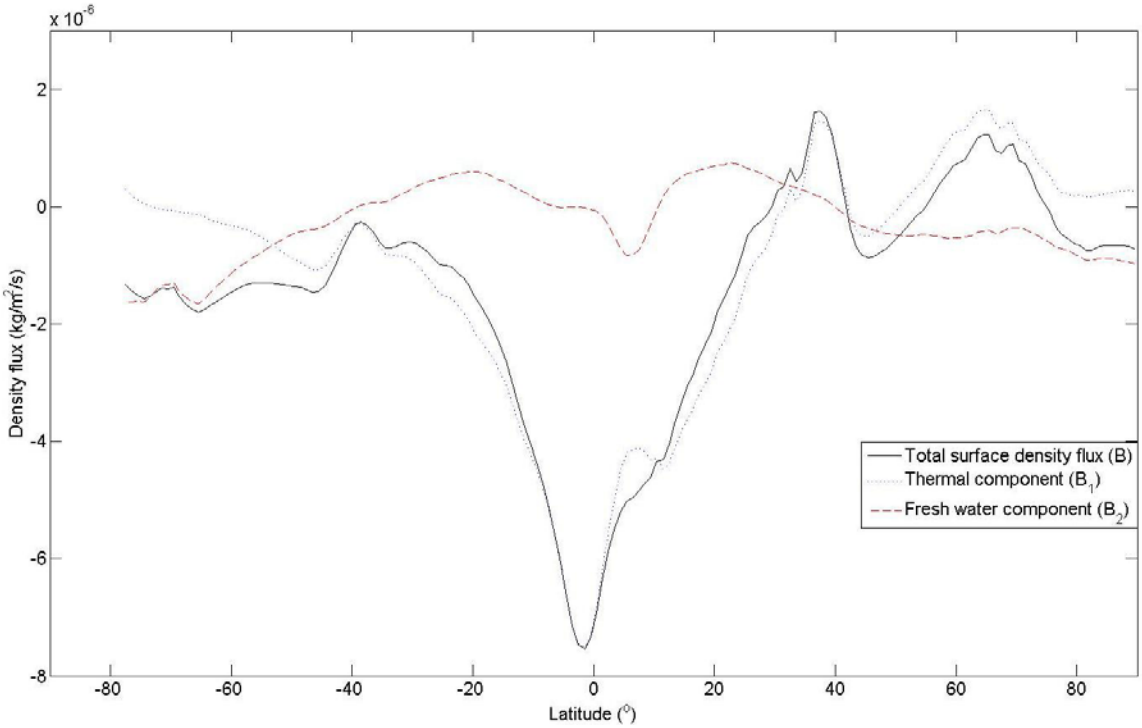

Figure 17. Same as Fig. 14, but from DaSilva-SMD94 climatology (period: 1945-1989).

Based on the foregoing considerations, ECMWF re-analysis has been chosen as the reference meteorological database in this study. This choice is supported by the charts in Fig. 22, which display the differences between the annually-averaged density fluxes obtained from ECMWF re-analysis and those computed from the other datasets. Indeed, ECMWF appears to be a good compromise between NCEP/NCAR, DaSilva-SMD94, and SOC-GASC97. NCEP/NCAR provides higher density flux than ECMWF by the subtropical west coast of major continents and over a large part of the subtropical North Atlantic Ocean. On the other hand, DaSilva-SMD94 and SOC-GASC97 give smaller values than ECMWF over all tropical and subtropical oceans expect for some west coast regions. These features are observed for almost all latitudes, as indicated by the zonal means of these density flux differences in Fig. 23.

Table 2 provides the global mean value of the density flux differences to assess the global accuracy of each meteorological database versus ECMWF. These values support the choice of ECMWF as the reference climatologic database for this study.

	Mean density flux difference $\left(\mathbf{kg\ m^{-2}s^{-1}}\right)$
$B\left(NCEP/NCAR\right)-B\left(ECMWF\right)$	$1.8716\text{x}10^{-7}$
$B\left(SOC-GASC97\right)-B\left(ECMWF\right)$	$-1.3075\text{x}10^{-6}$
$B\left(DaSilva\right)-B\left(ECMWF\right)$	$-1.3756\text{x}10^{-6}$

Table 2. Global averages of density flux differences between ECMWF re-analysis and the other databases.

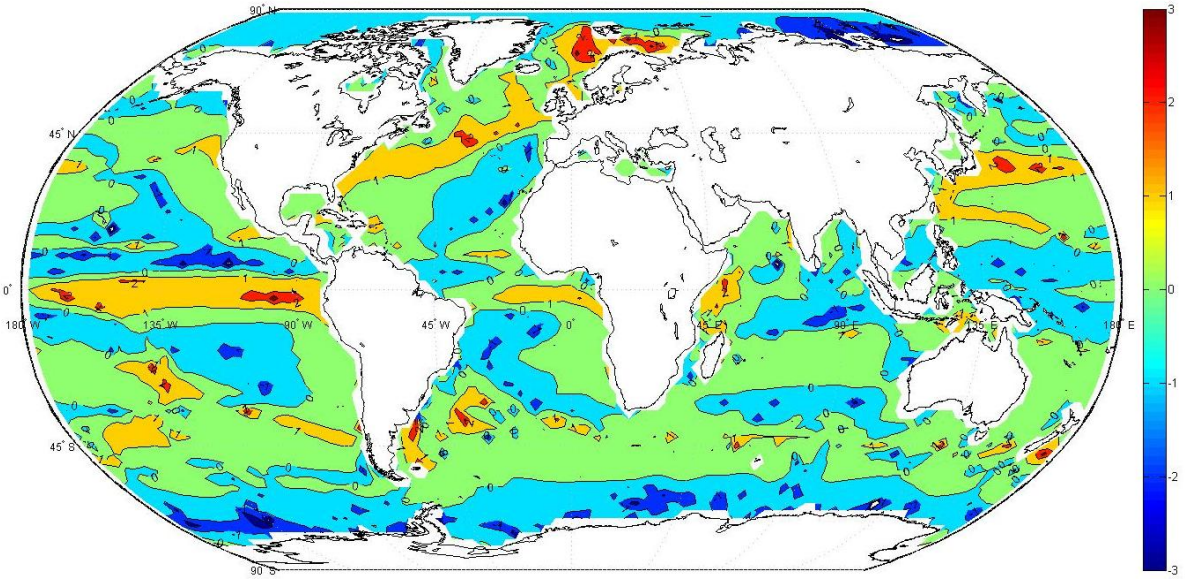

Figure 18. Annual-mean distribution of $\log\left(\frac{|B_1|}{|B_2|}\right)$ from ECMWF climatology (1979-2001).

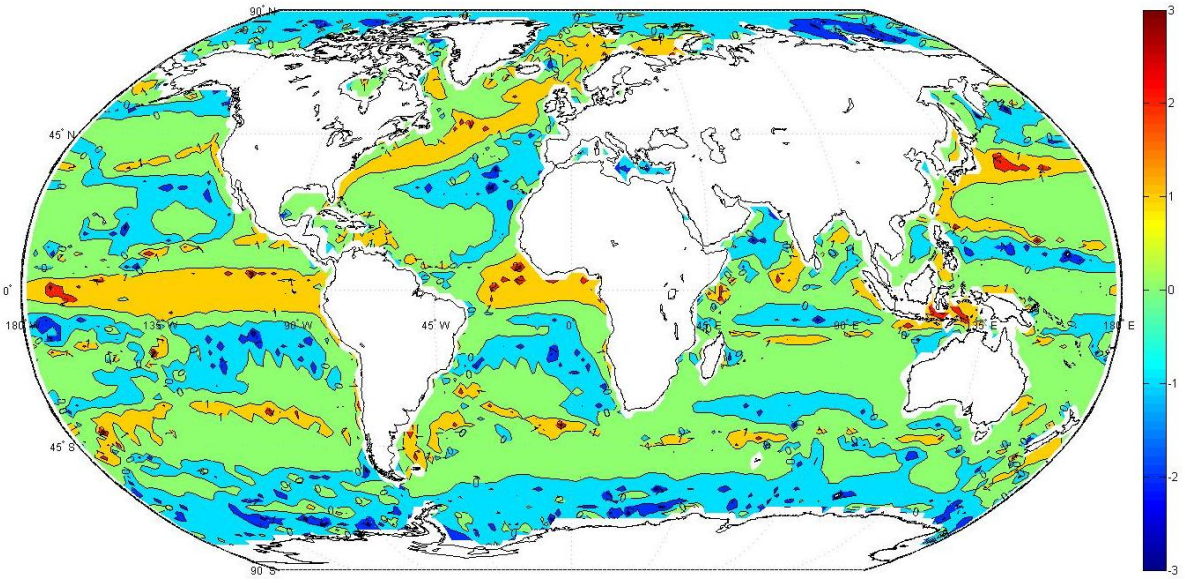

Figure 19. Same as Fig. 18, but from NCEP/NCAR re-analysis (1979-2001).

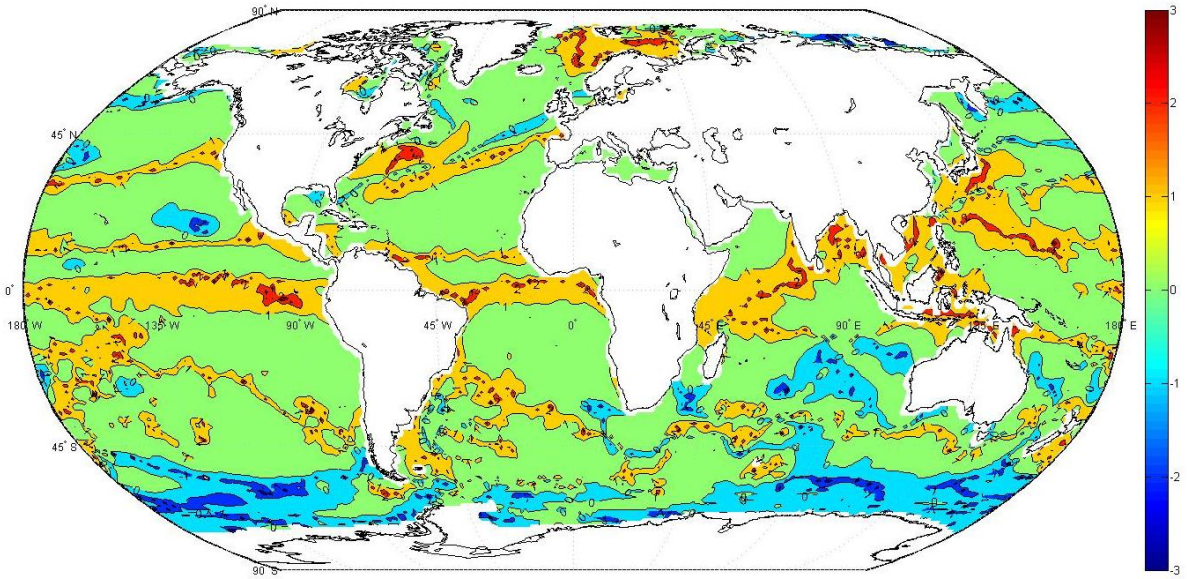

Figure 20. Same as Fig. 18, but from SOC-GASC97 climatology (period: 1980-1993).

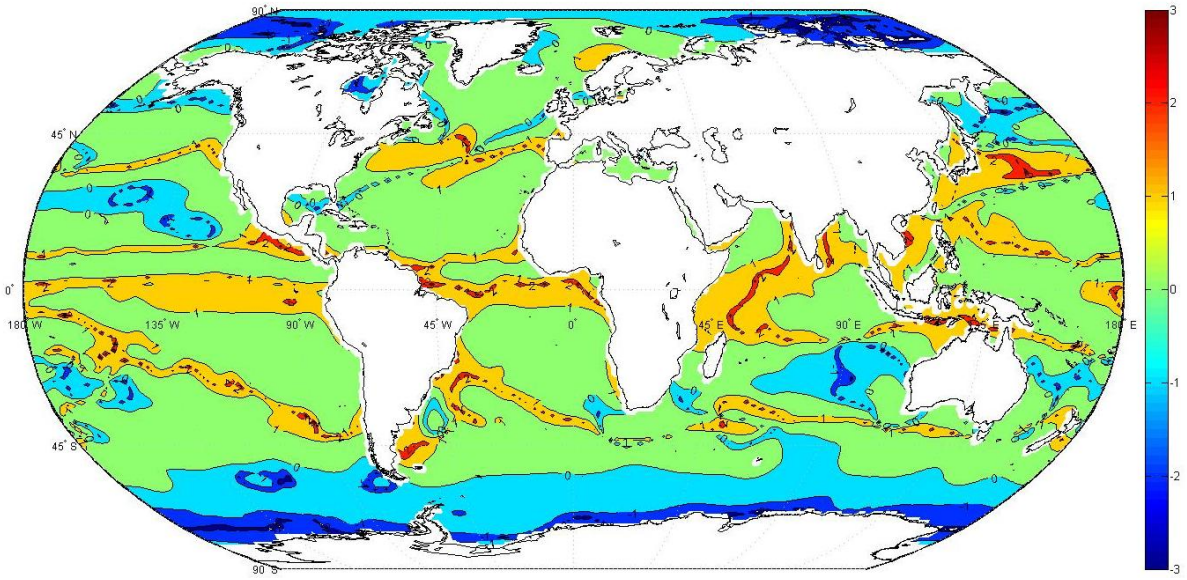

Figure 21. Same as Fig. 18, but from DaSilva-SMD94 climatology (period: 1945-1989).

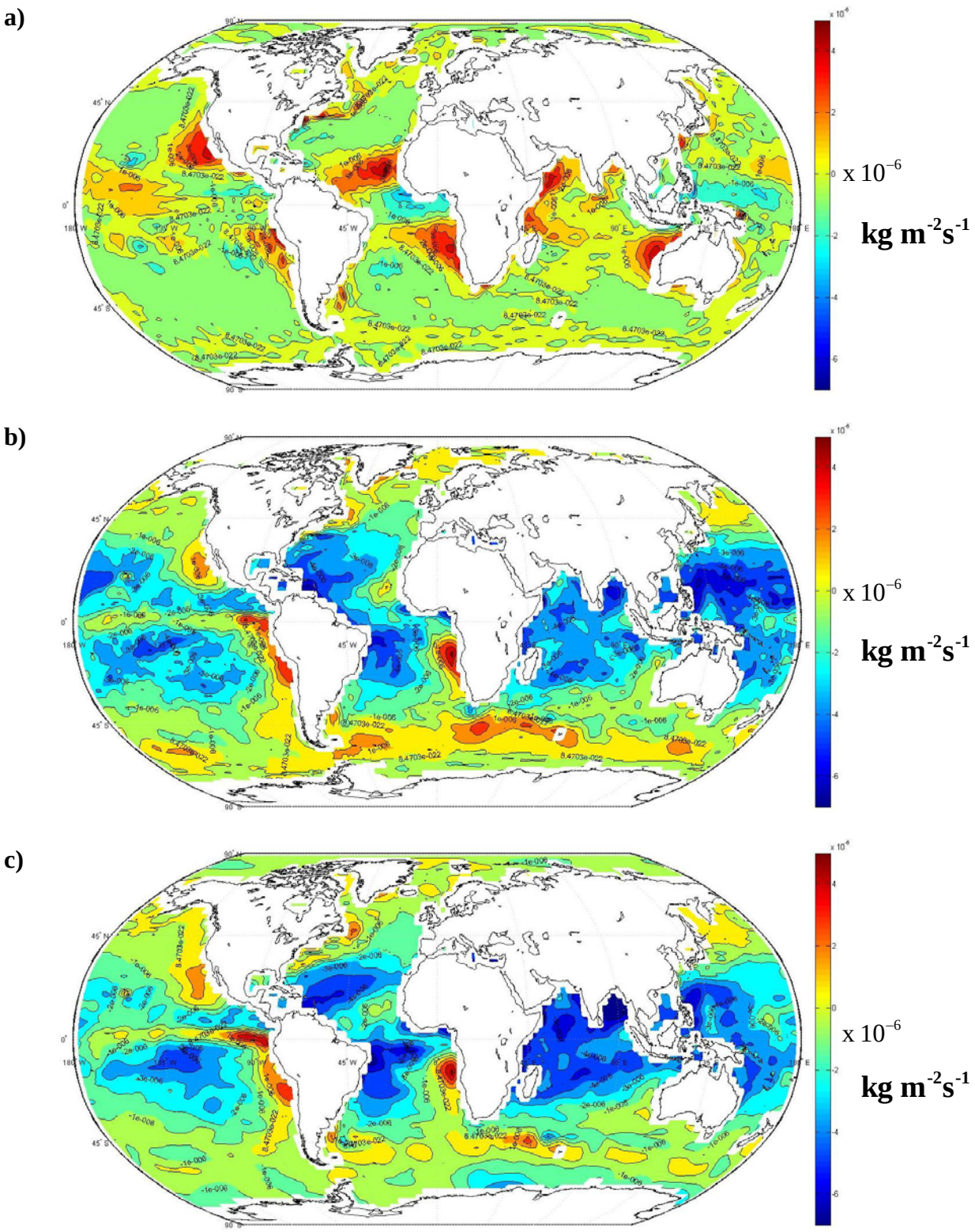

Figure 22. Differences in the surface density flux (a) $\left[B(NCEP/NCAR)-B(ECMWF)\right]$ (b) $\left[B(SOC-GASC97)-B(ECMWF)\right]$ (c) $\left[B(DaSilva)-B(ECMWF)\right]$.

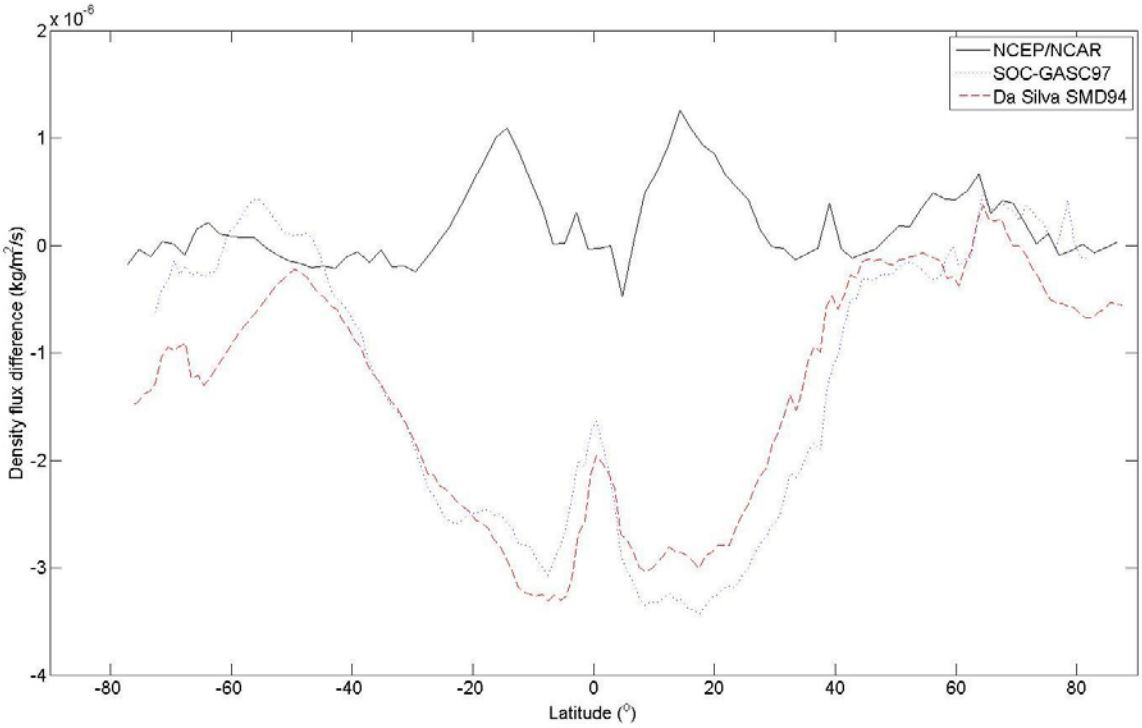

Figure 23. Zonal means of the differences in the surface density flux: $\left[B(NCEP/NCAR)-B(ECMWF)\right]$, $\left[B(SOC-GASC97)-B(ECMWF)\right]$, and $\left[B(DaSilva)-B(ECMWF)\right]$.

C. MOMENTUM FLUX AT THE SEA SURFACE

As described in section II-F, the computation of the Ekman flux requires the zonal and meridional components of the wind stress $\vec{\tau}$ at the sea surface, denoted by τ_{0x} and τ_{0y} respectively. Three databases have been used for the wind stress components: ECMWF re-analysis, NCEP/NCAR re-analysis, and DaSilva-SMD94 climatology, with the same periods of record as those defined for the density flux calculations. The computed Ekman flux provides a convenient check of the residual flux in regions where the eddy activity is weak.

IV. RESULTS AND ANALYSIS

A. GLOBAL OCEAN

Fig. 24 plots the zonally-averaged meridional cross-section, in which the climatological potential density anomaly contours, computed from Levitus94 database, are displayed. This cross-section is similar to the meridional cross-sections of individual oceans and shows a density distribution that is analogous to the schematic in Fig. 6b.

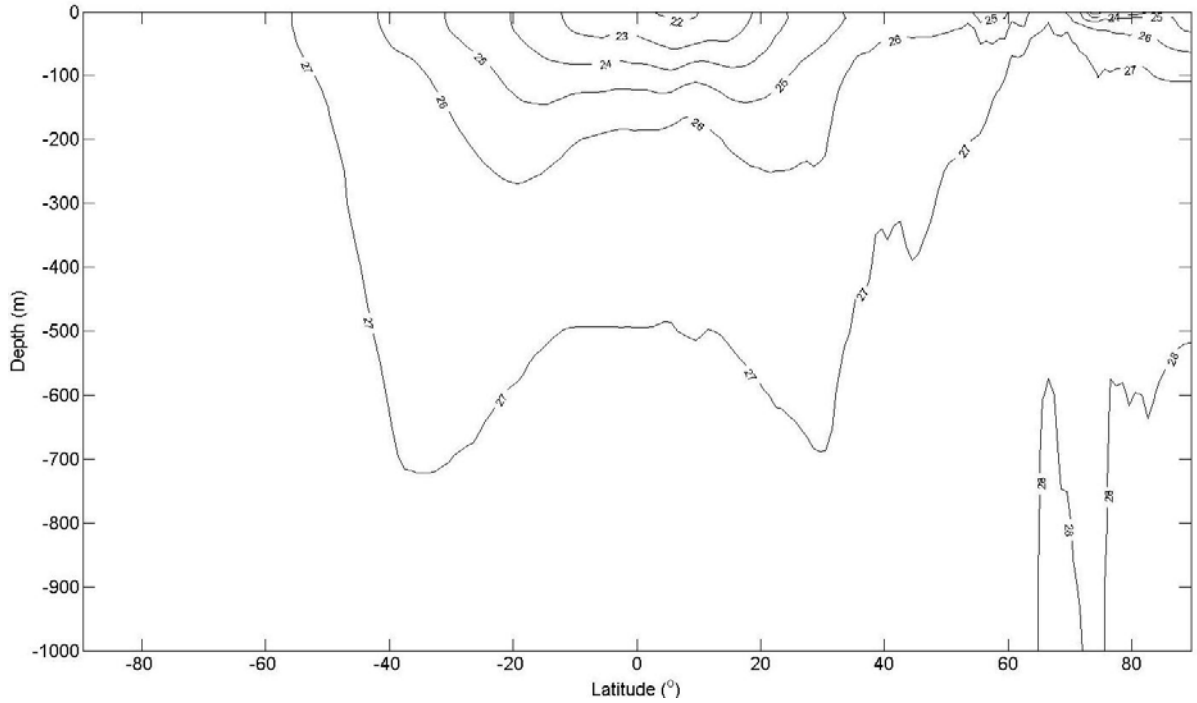

Figure 24. Zonally-averaged potential density anomaly (dimensionless) for the upper 1000 meters of the ocean. The data have been computed from the Levitus 94 climatology.

An advantage of applying the diagnostic model to the global configuration is that, unlike the individual basins, the water mass budget of the global ocean does not contain the contribution from the external sources or sinks. The density range considered for the

full ocean-wide residual flux budget extends from $\sigma_0 = 24.2$, determined in the previous chapter, to $\sigma_{\max} = 28.3$, the highest density of the ice-free sea surface area.

1. Diapycnal Volume Flux

The diapycnal interior flux (V_d), computed from the four meteorological databases using Eq. (21) and Eq. (22), is plotted in Fig. 25. Its general pattern and average value of 3.5 *Sv* (one Sverdrup is defined by $1\ Sv = 10^6\ m^3 s^{-1}$), obtained from the ECMWF climatology (reference database), are consistent with the earlier estimates by the Walin-type calculations (Donners et al. 2005).

For $\sigma < 26.1$, $V_d(\sigma)$ is positive, which implies an upward integrated flux across the σ isopycnal surfaces in the ocean interior. This result is a consequence of the strong low-latitude upwelling and the net upward air-sea heat flux in mid-latitude regions. Indeed, as indicated in Eq. (14), a positive density flux into the ocean (induced by a net upward air-sea flux) leads to a positive value of $F(\sigma)$ in each hemisphere, which implies water mass transformation to higher densities within the mixed-layer.

The diapycnal flux V_d then changes sign and remains negative over the density anomaly interval [26.1, 27.6]. This may be interpreted as a convergence of the residual flow within the mixed-layer in this density range. The negative values of V_d are associated with the strong sinking motion of Antarctic Intermediate Waters (AAIW) and Sub-Antarctic Mode Waters (SAMW), which occurs along the Antarctic Circumpolar Current (ACC), characterized by a potential density anomaly of about 27; indeed, the cross-isopycnal flux V_d has a negative peak value at $\sigma \approx 27.1$.

For $\sigma > 27.1$, V_d increases with σ and becomes positive from $\sigma = 27.6$. In fact, the strong downwelling along the ACC is compensated by the large-scale upwelling of North Atlantic Deep Water (NADW) and North Pacific Deep Water (NPDW), which takes places in the Southern Ocean, between the ACC and the Antarctic continent. Thus, our diagnostic results in Fig.25 are consistent with the distribution of water masses over the whole ocean, sketched in Fig. 2.

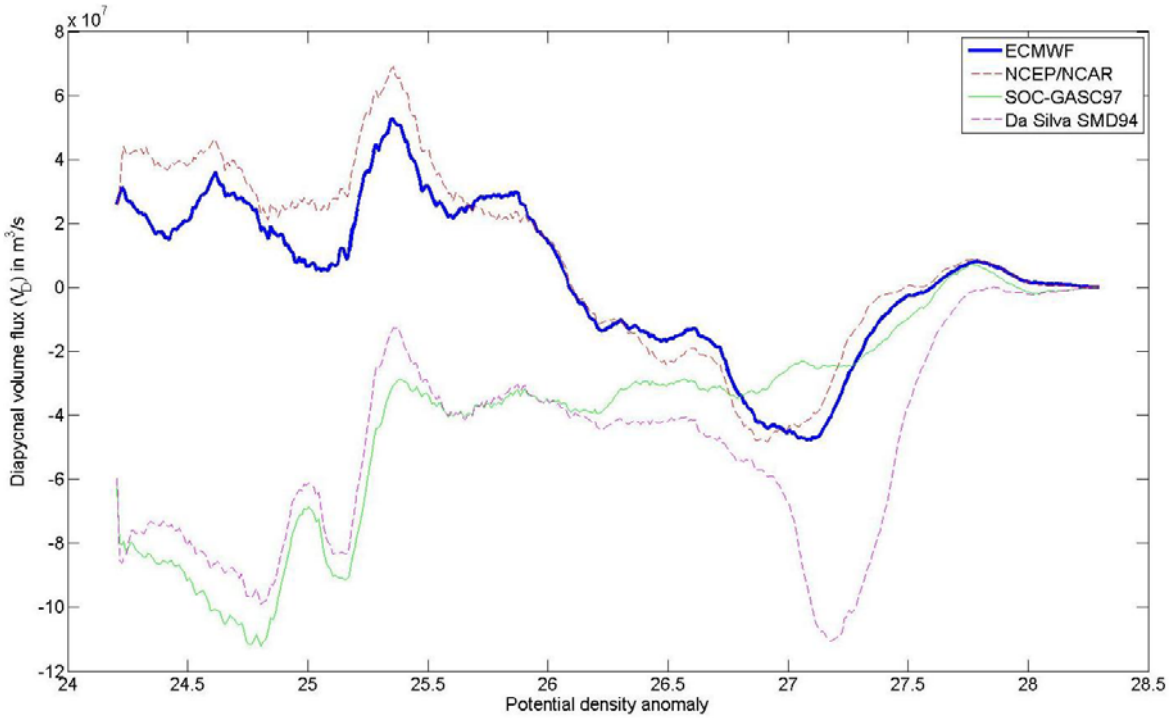

Figure 25. Diapycnal interior flux V_d in the global ocean computed from the four meteorological databases.

Fig. 25 also highlights the strong discrepancies among the V_d values obtained from the four climatologic databases. Only ECMWF and NCEP/NCAR datasets result in V_d profiles consistent with the previous results (Donners et al. 2005). However, NCEP/NCAR values are comparatively too high at low density anomalies $(\sigma < 26)$.

SOC-GASC97 and Da Silva SMD94 databases generally provide inconsistent V_d profiles. This result could be expected, since, as described in the previous chapter, the air-sea fluxes in these two databases are questionable for a large part of the whole ocean.

Table 3 gives the average cross-isopycnal flow differences between values obtained from ECMWF re-analysis and those computed from the other databases, over the potential density anomaly interval [24.2, 28.3]. This table should be compared with Table 2, which provides the global averages of density flux differences between ECMWF climatology and the other databases. The comparison shows that the diapycnal volume

flux estimates are critically dependent on the density flux accuracy. Indeed, as shown in Fig. 26, the absolute diapycnal volume flux accuracy is empirically related to the absolute mean density flux accuracy, by the following equation:

$$\left|\overline{V_D diff}\right| = 5.38\text{x}10^{25}\left|\overline{Bdiff}\right|^3 - 7.48\text{x}10^{19}\left|\overline{Bdiff}\right|^2 + 3.90\text{x}10^{13}\left|\overline{Bdiff}\right| \qquad (37)$$

where $\overline{V_D diff}$ is the average diapycnal volume flux accuracy, $\overline{Bdiff}$ is the mean density flux accuracy, and all the coefficients in Eq. (37) are measured in the corresponding MKS units.

	Mean diapycnal volume flux difference $\left(\mathbf{m^3 s^{-1}}\right)$
$V_D\left(NCEP/NCAR\right) - V_D\left(ECMWF\right)$	$5.0470\text{x}10^6$ (≈ 5 *Sv*)
$V_D\left(SOC - GASC97\right) - V_D\left(ECMWF\right)$	$-4.3530\text{x}10^7$ ($\approx$-43.5 *Sv*)
$V_D\left(DaSilva\right) - V_D\left(ECMWF\right)$	$-5.2320\text{x}10^7$ ($\approx$-52 *Sv*)

Table 3. Means of diapycnal volume flux differences between ECMWF re-analysis and the other databases.

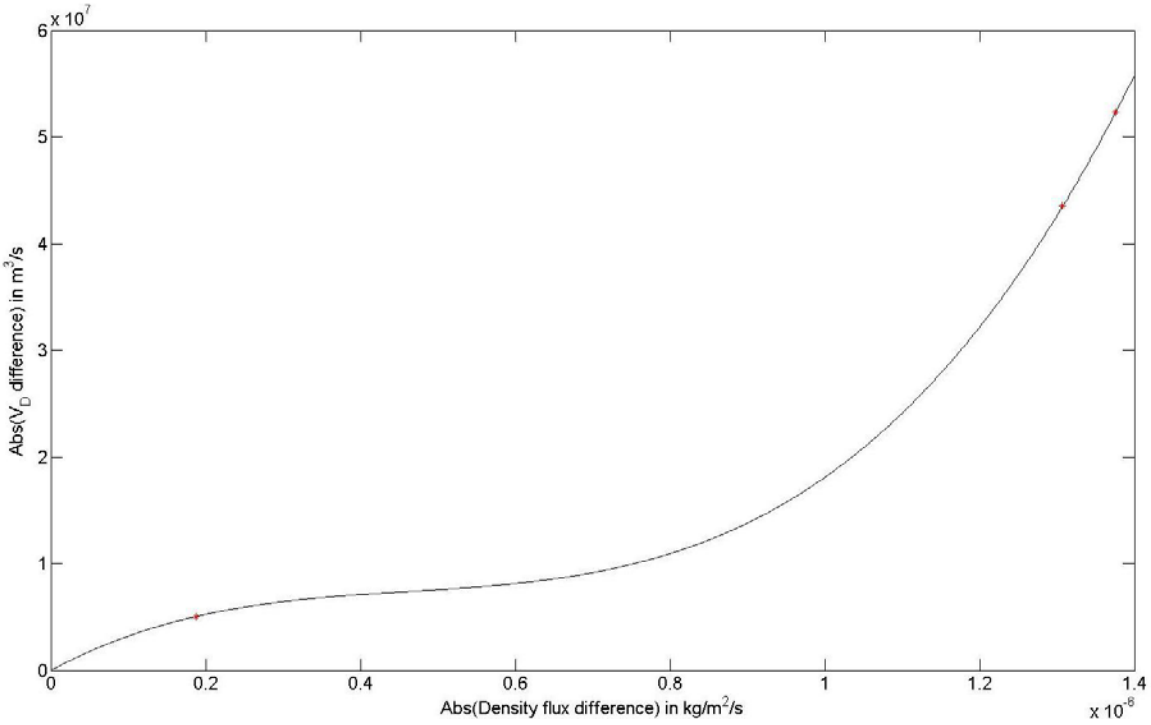

Figure 26. Empirical relation between the absolute mean density flux accuracy and the absolute average diapycnal volume flux accuracy. The red dots represent the differences in the density flux means and in the associated diapycnal volume flux averages between, from left to right, NCEP/NCAR and ECMWF, SOC-GASC97 and ECMWF, and Da Silva SMD94 and ECMWF, respectively.

2. Adiabatic Advection

Fig. 27 gives the distributions of the along-isopycnal interior flux (V_a), computed from the four meteorological databases using Eqs. (21), (23), and (25). The plots display the residual (total) fluxes and their Ekman components. These plots should be interpreted with caution, since they represent the integrated isopycnal interior flux over the potential density anomaly range $[\sigma, \sigma_{\max}]$. Thus, changes in the direction of the MOC circulation (northward or southward) are observable by maxima and minima in the V_a profiles.

The direction of the overturning at each σ is determined by sign of $\left(-\frac{\partial V_a}{\partial \sigma}\right)$. Since V_a is defined by $V_a(\sigma) = \frac{1}{2}\left[V_N(\sigma) - V_S(\sigma)\right]$ [Eq. (25)], an increasing (decreasing) V_a from $\sigma_{\max}$ down to σ_0 corresponds to a northward (southward) flux.

Therefore, the total V_a pattern makes it simple to identify the individual components of the isopycnal MOC. Most notably, the southward flux of the North Atlantic Deep Water (NADW) is reflected in the strong decrease in V_a from about $\sigma = 27.6$ to $\sigma = 27.1$. The northward moving water masses originating in the ACC (Antarctic Intermediate Water and the Sub-Antarctic Mode Water) also have a clear signature through the significant increase in V_a from about $\sigma = 27.1$ to $\sigma = 26.1$.

Based on the residual (total) isopycnal flux profile computed from ECMWF climatology, the sketch in Fig. 28 summarizes the mean adiabatic MOC circulation for the whole ocean. Fig. 29 is a schematic of the inferred zonally-averaged meridional cross-section of the whole ocean.

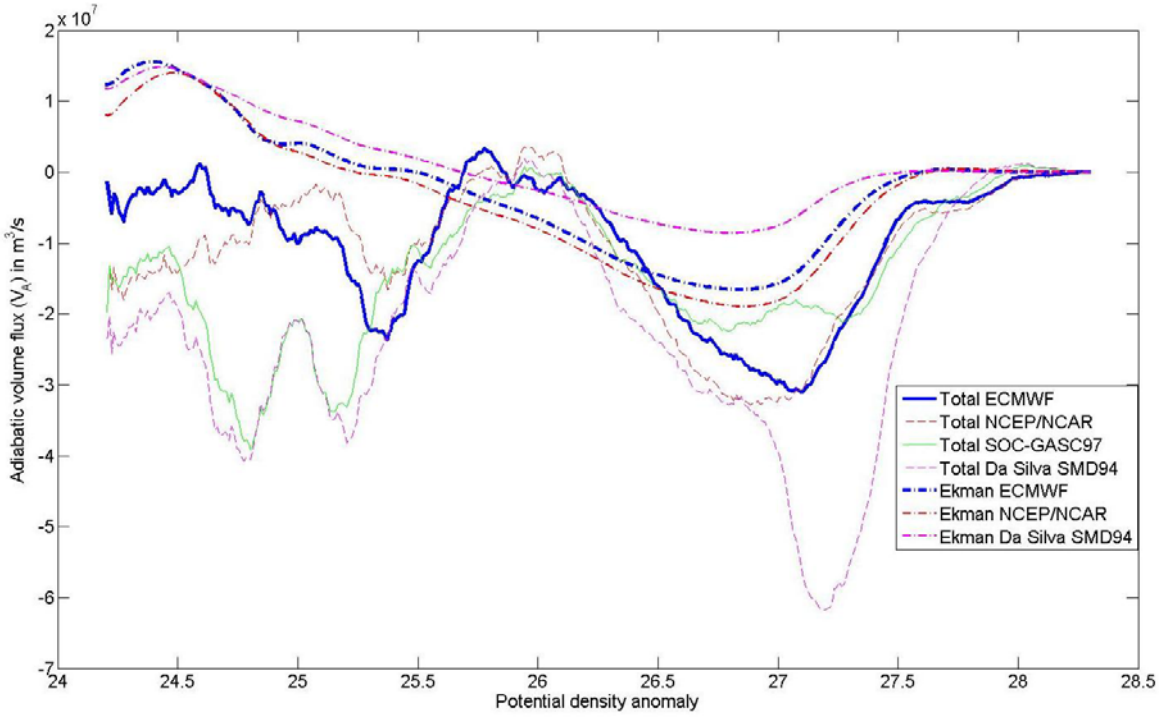

Figure 27. Adiabatic interior flux V_a in the global ocean computed from the four meteorological databases.

The V_a profiles in Fig. 27 shows the pattern of the meridional overturning that is generally consistent, in terms of magnitude and direction, with earlier numerical and observational studies.

It is also important to point out that signs and magnitudes of V_a computed from the total flux and their wind-driven components based on the Ekman transport are poorly correlated. One of the interpretations of this result is that the global MOC adiabatic component may not be mainly driven by mechanical forcing generated by winds, and the eddy contribution is essential for the maintenance of meridional overturning.

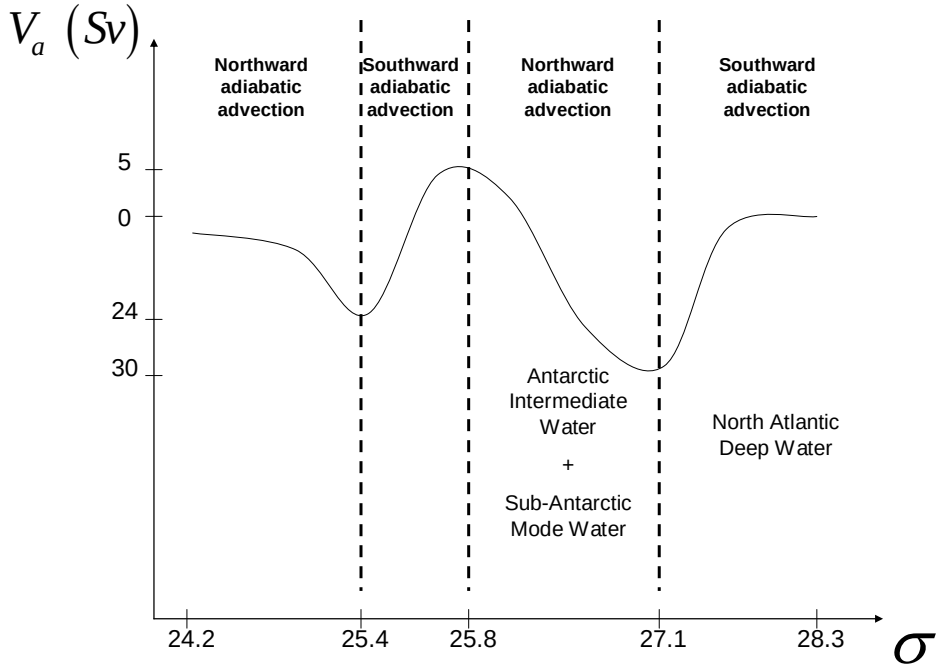

Figure 28. Schematic of the adiabatic meridional overturning circulation in the global ocean.

The V_a profile computed form the reference climatology (ECMWF) indicates that the integrated adiabatic advection over the whole density range $[\sigma_0, \sigma_{\max}]$ is almost zero. This implies that, as expected, the northward and southward interior fluxes balance each other in this density interval, lending more credence to the proposed diagnostics.

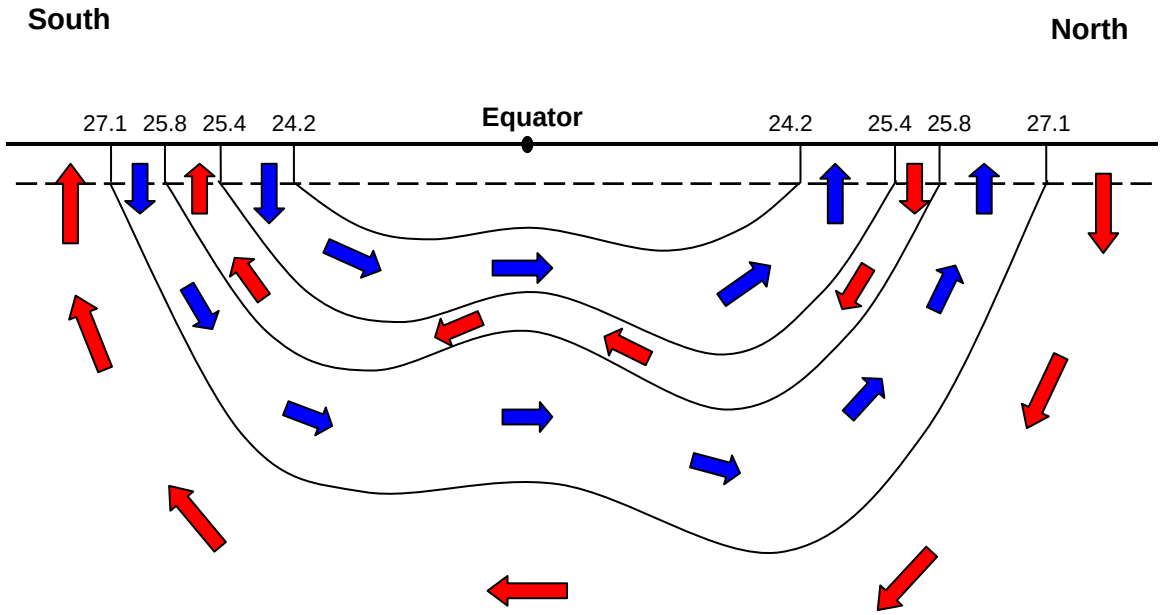

Figure 29. Schematic of the zonally-averaged meridional cross-section of the global ocean and the associated MOC. Red arrows label southward adiabatic advection and blue arrows depict northward adiabatic advection.

In addition, Fig. 27 highlights the discrepancies among the V_a values obtained from the four climatologic databases. The differences in the sea surface density flux between these datasets do not result in as large changes in V_a profile as those in the V_d computations. Moreover, we still observe that, similar to V_d plots (Fig.25), the V_a profiles based on ECMWF and NCEP/NCAR climatology are relatively close to each other, while those calculated from SOC-GASC97 and Da Silva SMD94 have significant differences.

Table 4 gives the average along-isopycnal flux differences between values obtained from ECMWF re-analysis and those computed from the other databases, over the potential density anomaly interval [24.2, 28.3]. As in section IV-A-1, results in this table should be compared with those in Table 2. This comparison shows that the estimates of isopycnal volume flux are much less dependent on the density flux accuracy than are those of diapycnal volume flux. Indeed, the V_a differences among the different databases are much lower that the corresponding V_d differences. Unlike V_d, no coherent

empirical function relating the absolute mean density flux accuracy and the absolute average adiabatic flux accuracy was found. This result could be expected since signs of mean density flux differences and mean isopycnal volume flux differences are not correlated [see Tables 2 and 4].

	Mean isopycnal volume flux difference $\left(\mathbf{m^3 s^{-1}}\right)$
$V_A\left(NCEP/NCAR\right)-V_A\left(ECMWF\right)$	$-1.2506\text{x}10^6$ ($\approx$-1 *Sv*)
$V_A\left(SOC-GASC97\right)-V_A\left(ECMWF\right)$	$-4.0233\text{x}10^6$ ($\approx$-4 *Sv*)
$V_A\left(DaSilva\right)-V_A\left(ECMWF\right)$	$-1.1483\text{x}10^7$ ($\approx$-11*Sv*)

Table 4. Means of isopycnal volume flux differences between ECMWF re-analysis and the other databases.

3. Adiabatic Flux Ratio

Table 5 gives the adiabatic flux ratios computed from each meteorological climatology using Eq. (28). Here, the adiabatic flux ratios from ECMWF and NCEP/NCAR are about 3.5 and 3.0, respectively. Their magnitudes support the theory that the global Meriodional Overturning Circulation has a dominant adiabatic component. The SOC-GASC97 and Da Silva SMD94 values are provided here only for references without further interpretation, since their corresponding V_d and V_a profiles appear to be inconsistent with the real oceanic circulation.

Database	**Adiabatic flux ratio** γ **(dimensionless)**
ECMWF	3.5018
NCEP/NCAR	3.0288
SOC-GASC97	1.4552
Da Silva SMD94	2.3247

Table 5. Adiabatic flux ratios for the global ocean computed from the four meteorological databases.

B. ATLANTIC OCEAN

If we limit our study of the Atlantic Ocean to the density range for which all isopycnals are zonally bounded by land throughout the year, the potential density anomaly interval reduces to [24.2, 25.4]. These values are obtained from the analysis of the monthly mean distribution of potential density [not shown]. As mentioned previously, confining the analysis to this density range permits an accurate description of the upper-ocean meridional circulation. This assures the absence of major external sources of water as assumed in the model formulation (section II).

$V_d(\sigma)$ and $V_a(\sigma)$ over the sigma range [24.2, 28.3] (used for the global ocean computations) have also been computed in order to assess the Atlantic contribution to the global MOC, although their pattern in the range [26.5, 28] could be affected by the contribution from the Antarctic Circumpolar Current (ACC).

1. Diapycnal Volume Flux

The diapycnal interior flux (V_d) in the upper Atlantic Ocean, computed from the four meteorological databases using Eq. (21) and Eq. (22), is plotted in Fig. 30. Its average over the potential density anomaly range [24.2, 25.4] is approximately 6.7 *Sv* from the ECMWF climatology (reference database).

Fig. 30 shows that V_d is mostly weak over the density interval [24.20, 25.16]: its values remain between -9 *Sv* and +8 *Sv* (ECMWF). The diabatic volume flux abruptly increases to reach its maximum magnitude (37 *Sv*) at about $\sigma = 25.34$. This peak value corresponds to the high upward net heat flux at the surface of the Gulf Stream. Indeed, the mean potential density anomaly at 40 m depth within the Gulf Stream is $\sigma \approx 25.35$.

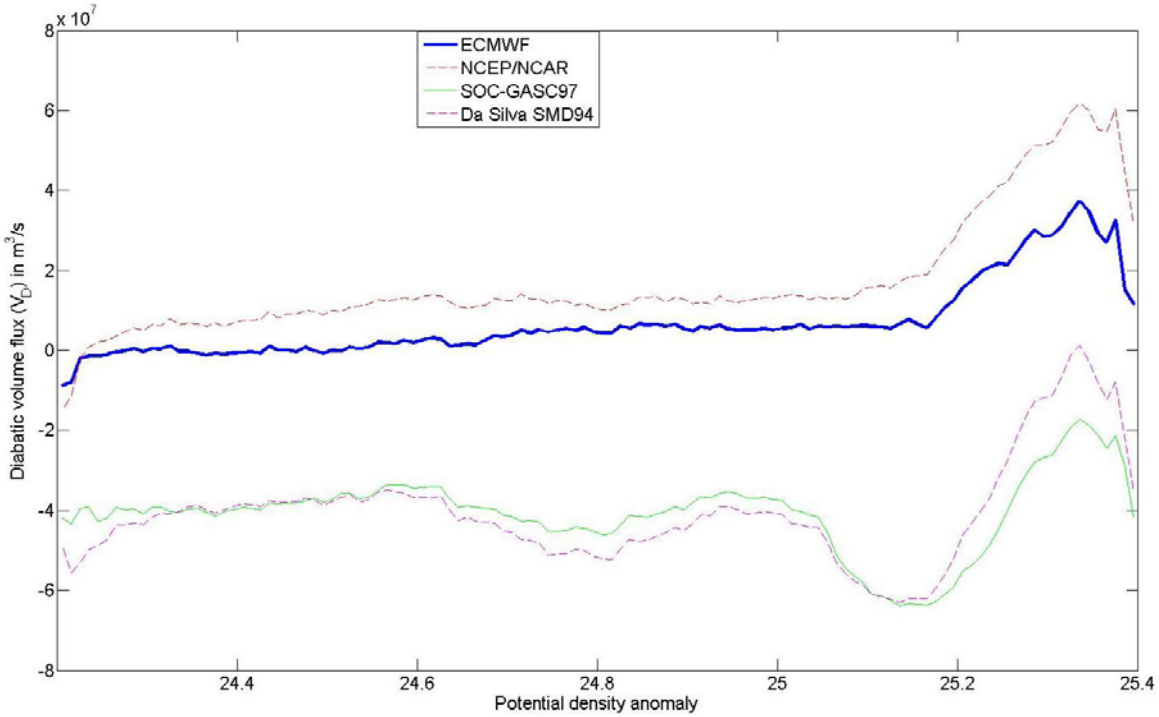

Figure 30. Diapycnal interior flux V_d in the Atlantic Ocean computed from the four meteorological databases.

Similar to the global diapycnal volume flux distribution, we note large discrepancies between the V_d estimates from different databases. Results from ECMWF and NCEP/NCAR re-analyses show many similarities, but NCEP/NCAR density forcing seems to be too high with regard to V_d values. Concerning SOC-GASC97 and Da Silva SMD94 climatologies, the results are again unrealistic, which we attribute to the lack of observational data for the Southern Atlantic Ocean. This last point is illustrated in Fig. 31, where the values of $F(\sigma) = \int_{\sigma} \vec{U} \cdot \vec{n}\, dl$ [defined in Eq. (13)] in the Northern and Southern Hemispheres are given for the four climatologic databases: the differences in F_N values are much lower than those in F_S estimates.

2. Adiabatic Advection

Fig. 32 gives the along-isopycnal interior fluxes (V_a), computed from Eqs. (21), (25), and (27) using the four meteorological databases. Here, $V_a(\sigma)$ estimates represent the integrated isopycnal interior flux over the potential density anomaly range $[\sigma_0, \sigma]$ instead of over the density interval $[\sigma, \sigma_{\max}]$ (as in the global ocean computations).

Changes in the direction of the MOC circulation (northward or southward) are still observable by maxima and minima in the V_a profiles, but, in this case, the direction of the adiabatic advection at each σ is given by the sign of $\frac{\partial V_a}{\partial \sigma}$: $\frac{\partial V_a}{\partial \sigma} > 0$ means a northward flux, and $\frac{\partial V_a}{\partial \sigma} < 0$ corresponds to a southward flux. $V_a(\sigma)$, calculated from ECMWF (reference climatology), shows a weak southward integrated isopycnal flow for $24.20 < \sigma < 25.17$ and then a strong northward flow for $25.17 < \sigma < 25.38$. This points out the predominantly northward residual flow in the Atlantic upper thermocline. Figure 32 also highlights the strong effect of the large and positive density flux (into the ocean) in the Gulf Stream region on the adiabatic flow in the upper Atlantic Ocean.

Concerning the Ekman fluxes, the plots suggest that the MOC in the Atlantic Ocean is not driven by the local mechanical forcing (wind stress). This result is similar to that obtained for the global thermohaline circulation.

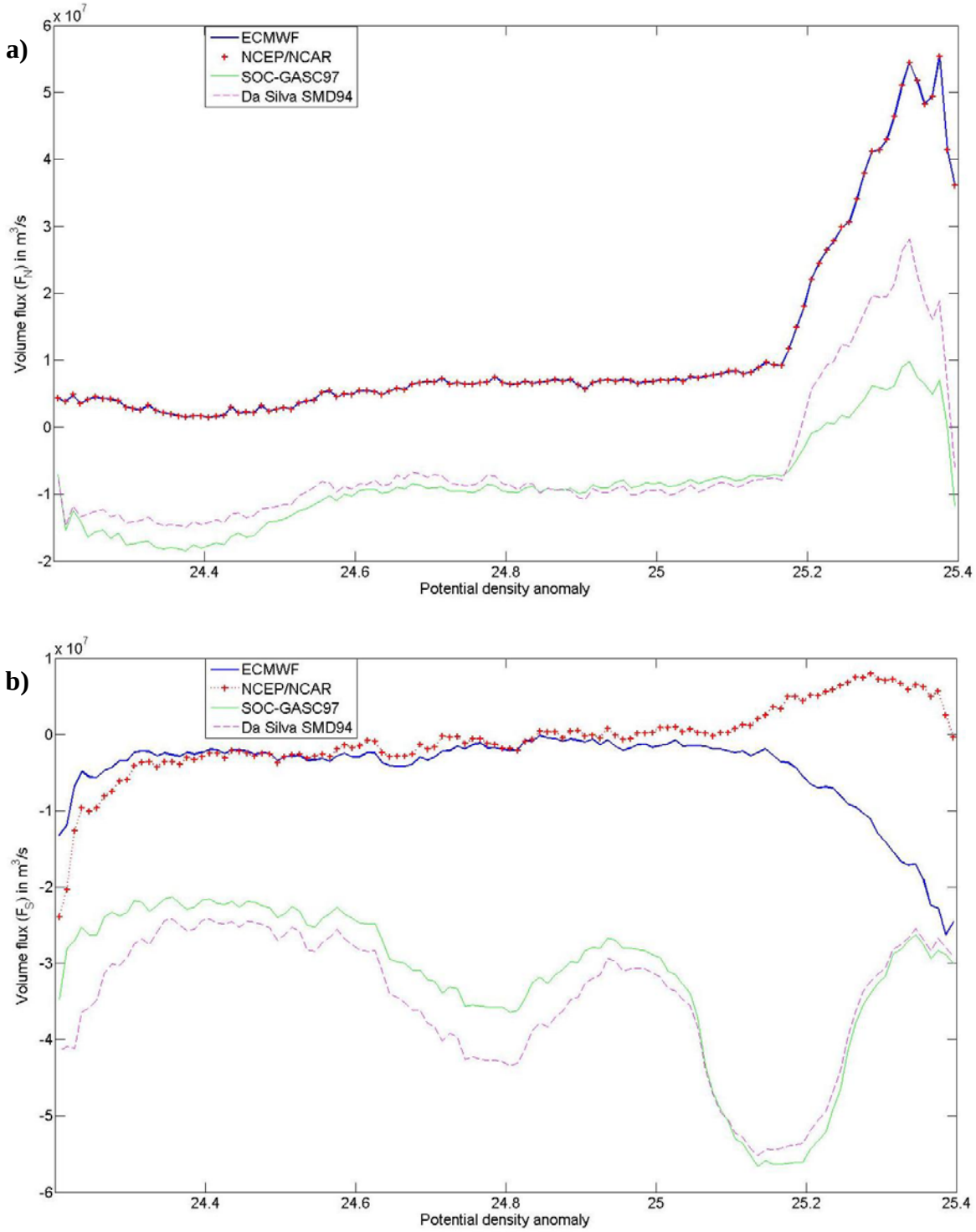

Figure 31. Cross-isopycnal volume flux within the mixed-layer. (a) In the Northern Hemisphere $\left(F_N(\sigma)\right)$. (b) In the Southern Hemisphere $\left(F_S(\sigma)\right)$.

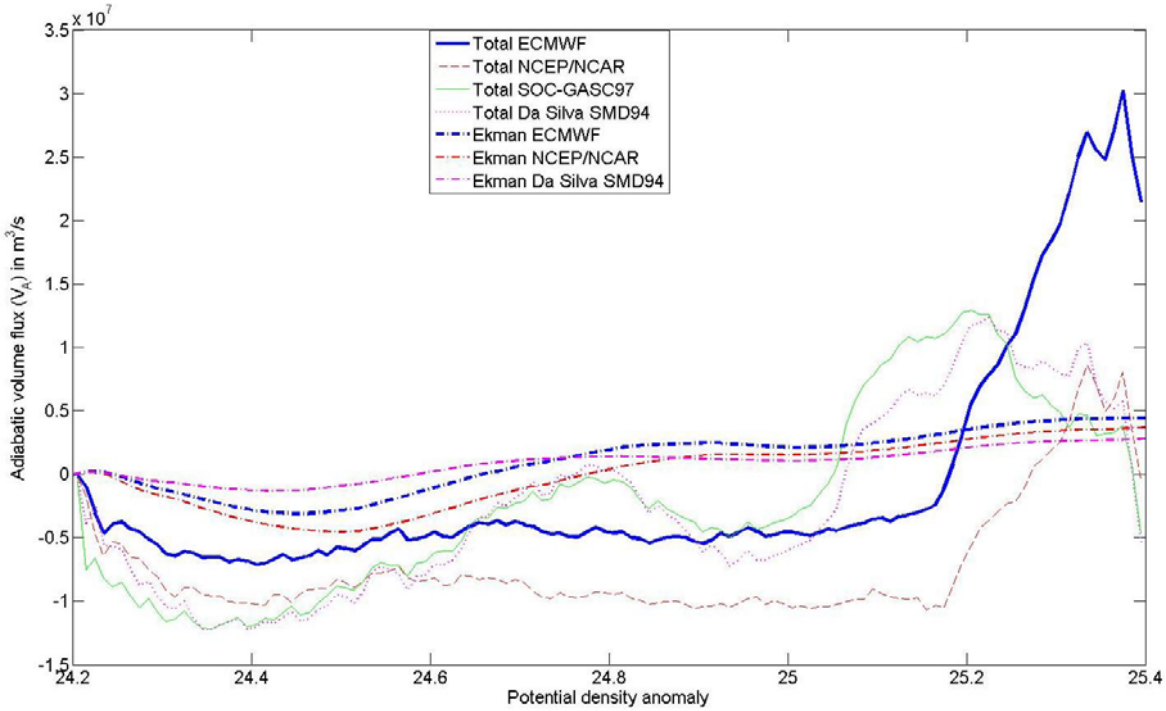

Figure 32. Adiabatic interior flux V_a in the upper Atlantic Ocean computed from the four meteorological databases.

3. Adiabatic Flux Ratio

Table 6 gives the adiabatic flux ratios for the Atlantic basin. This parameter is relatively high ($\gamma \approx 3.6$) for the ECMWF computations, which suggests that the meridional overturning in the Atlantic thermocline is controlled by the adiabatic processes (advection and eddy-transfer). However, the other meteorological databases do not support this hypothesis.

Database	**Adiabatic flux ratio γ (dimensionless)**
ECMWF	3.5675
NCEP/NCAR	1.1484
SOC-GASC97	0.3983
Da Silva SMD94	0.6259

Table 6. Adiabatic flux ratios for the upper Atlantic Ocean computed from the four meteorological databases.

4. Atlantic Contribution to Global MOC

In order to estimate the Atlantic contribution to the global thermohaline circulation, we can compute the diabatic and adiabatic volume fluxes over the density interval [24.2, 28.3] and compare them to the values corresponding to the global ocean.

For this computation, we include in the Atlantic basin the southern ocean between Cape Horn and Cape of Good Hope. Note that this extension of the Atlantic surface adds external sources of water and might lead to uncertainties in V_d and V_a estimates. In particular, we may expect differences on the order of 5-10 *Sv* between the entering ACC flow in the Drake Passage and the exiting flow to the south of Africa. Such differences are not significant relative to the ACC mean volume flux (100 *Sv*), but may be relevant for our results (on the order of 10 *Sv*).

Figures 33 and 34 show $V_d(\sigma)$ and $V_a(\sigma)$ over the potential density anomaly range of [24.2, 28.3]. Note that $V_a(\sigma)$ again represents the MOC adiabatic advection over the density range $[\sigma, \sigma_{\max}]$, as in the global ocean computations.

Comparisons between Figs. 33 and 25 and between Figs. 34 and 27 show many similarities in the sign and magnitude of the MOC components. These similarities suggest that the global pole-to-pole MOC is strongly influenced by the Atlantic Ocean. In particular, the peak values in V_d and V_a profiles at $\sigma \approx 25.35$, which correspond to the Gulf Stream signature, are noticeable on Figs. 25, 27, 33, and 34.

Table 7 provides the adiabatic flux ratios for the entire Atlantic basin. The very high value ($\gamma \approx 4.11$ for ECMWF climatology) supports the conclusion that the meridional overturning in the whole Atlantic Ocean is mainly adiabatic.

Figures 32 and 34 display the discrepancies among the V_a values obtained from the four climatologic databases. Again we see that the differences in $V_a(\sigma)$ are not as large as those observed for $V_d(\sigma)$.

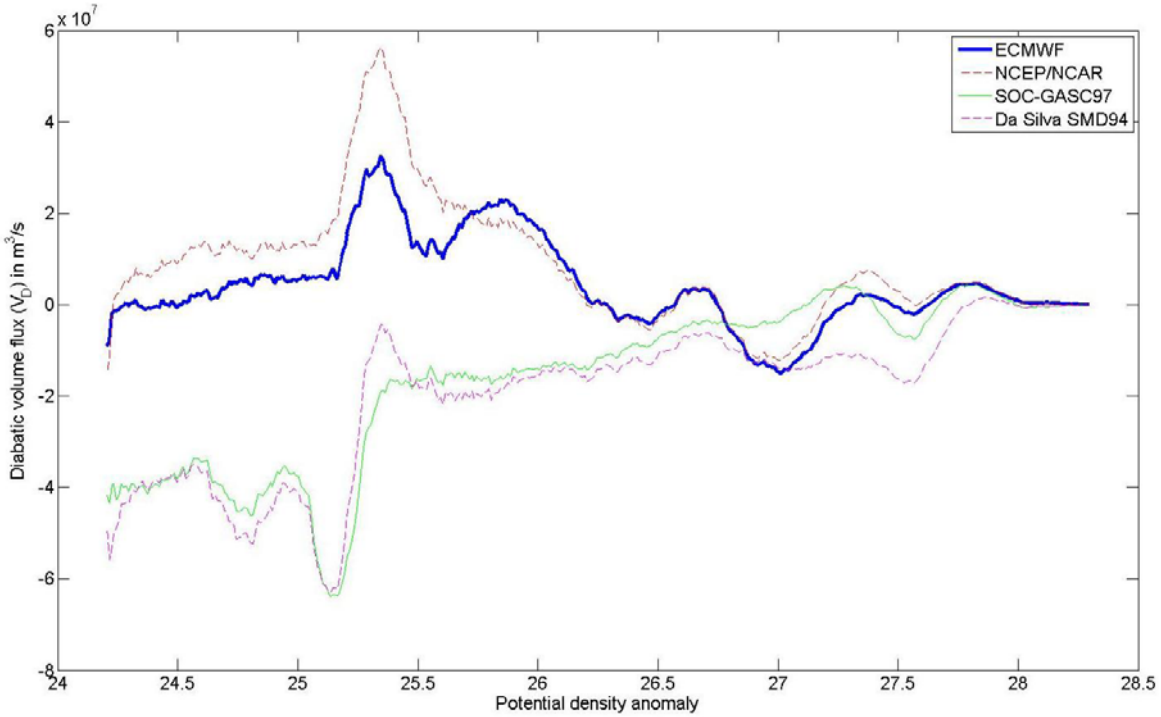

Figure 33. Diapycnal interior flux V_d in the entire Atlantic Ocean computed from the four meteorological databases.

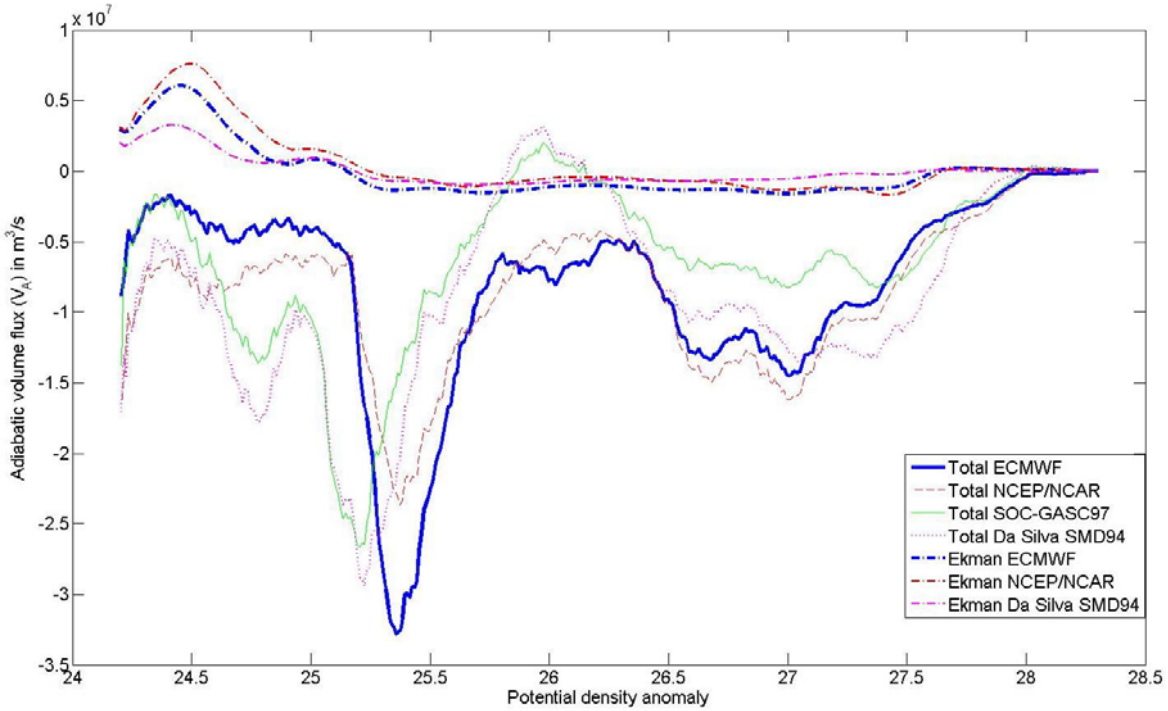

Figure 34. Adiabatic interior flux V_a in the entire Atlantic Ocean computed from the four meteorological databases.

Database	Adiabatic flux ratio γ (dimensionless)
ECMWF	4.1055
NCEP/NCAR	2.5272
SOC-GASC97	1.7821
Da Silva SMD94	2.0053

Table 7. Adiabatic flux ratios for the entire Atlantic Ocean computed from the four meteorological databases.

5. Method Comparison

Section III-A presents two ways for computing the residual flux at the bottom of the mixed-layer. The first method uses integration along the isopycnal contours [Eq. (14)] within the mixed-layer, while the second one computes integrals over the surface bounded by these contours [Eq. (21)].

The two methods are mathematically equivalent, but, in practice, may lead to relatively significant differences in estimates of V_a and V_d, depending on the grid resolution. Therefore, comparing their results gives a consistency check of the estimate accuracy. Note that the second method is more convenient, and for this reason it [Eq. (21)] will be mostly used.

Figure 35 gives $V_d(\sigma)$ and $V_a(\sigma)$ profiles computed by the two methods from ECMWF climatology. These profiles show that V_a and V_d estimates weakly depend on the method used. This is also observed for the adiabatic flux ratios, which are, respectively, $\gamma = 3.6607$ and $\gamma = 3.5675$, for the integration along isopycnal contours and the surface integrals.

a)

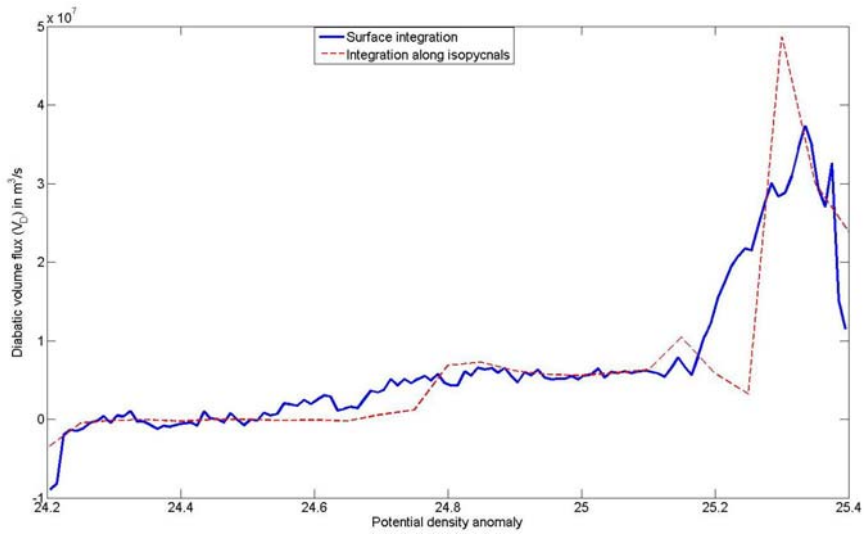

b)

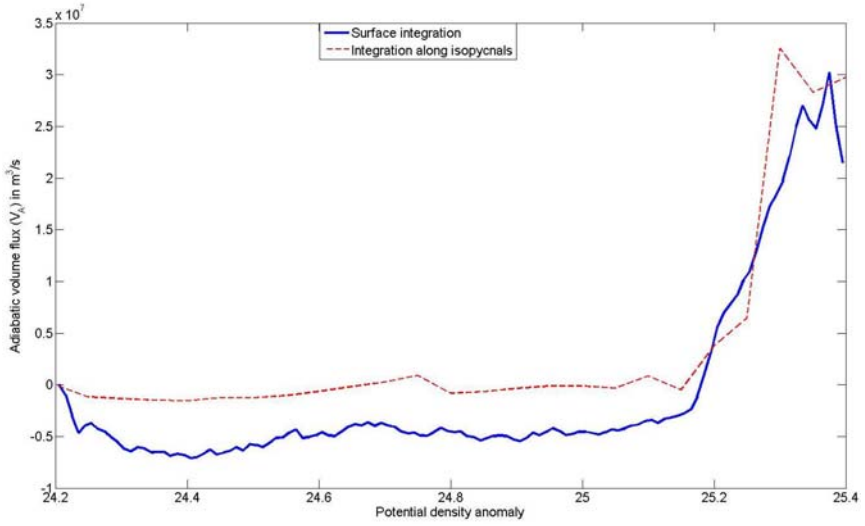

Figure 35. MOC components in the Atlantic Ocean computed from ECMWF climatology. (a) Diapycnal volume flux V_d. (b) Adiabatic volume flux V_a.

C. PACIFIC AND INDIAN OCEANS

The MOC components for the Indian Ocean have not been computed separately. Indeed, the Asian continent constitutes a northern boundary at low latitudes and therefore inhibits any isopycnal transport in the Indian basin, as shown by the distribution of potential density at 40 m depth in Fig. 9.

The large Pacific Ocean and its density field permit a pole-to-pole overturning circulation, which has to be studied. In addition, the numerous "holes" in its western lateral boundaries, and particularly the Indonesian archipelago, make it necessary to take into account the density forcing over the Indian Ocean as a possible source of water mass transformation in the Pacific basin. For these reasons, calculations will be carried out for the Pacific Ocean only and for the combined Indian-Pacific Ocean, and results compared.

Similar to the Atlantic Ocean computations, we first limit our study of the Pacific and Indian Oceans to the density range for which all isopycnals are zonally bounded by land throughout the year: the monthly-averaged potential density distribution [not shown] provides the potential density anomaly range of [23.8, 25.4]. It is also interesting to assess the Pacific and Indian contributions to the global MOC by computing $V_d(\sigma)$ and $V_a(\sigma)$ over the sigma range [24.2, 28.3], used for the global ocean calculations.

1. Diapycnal Volume Flux

The diapycnal interior flux (V_d) in the upper Pacific Ocean is plotted in Fig. 36. Its average value over the potential density anomaly range [23.8, 25.4] is about 3.6 *Sv* (ECMWF climatology). This mean value is less than that computed in the upper Atlantic Ocean, but, at each σ, V_d is generally higher in the Pacific than in the Atlantic.

We note some peak values on the V_d profile, but no characteristic signature of the Kuroshio Current $(\sigma \approx 25.0)$. Indeed, we would have expected a positively high value around $\sigma = 25.0$ due to the high upward net heat flux at the surface of this warm western boundary current [see Fig. 10]. Instead, we observe a negative peak value at $\sigma \approx 25.1$. This result suggests that the Gulf Stream has a much bigger impact on the MOC than the Kuroshio Current. In fact, Fig. 10 indicates that the highest density forcing is in the Gulf Stream region.

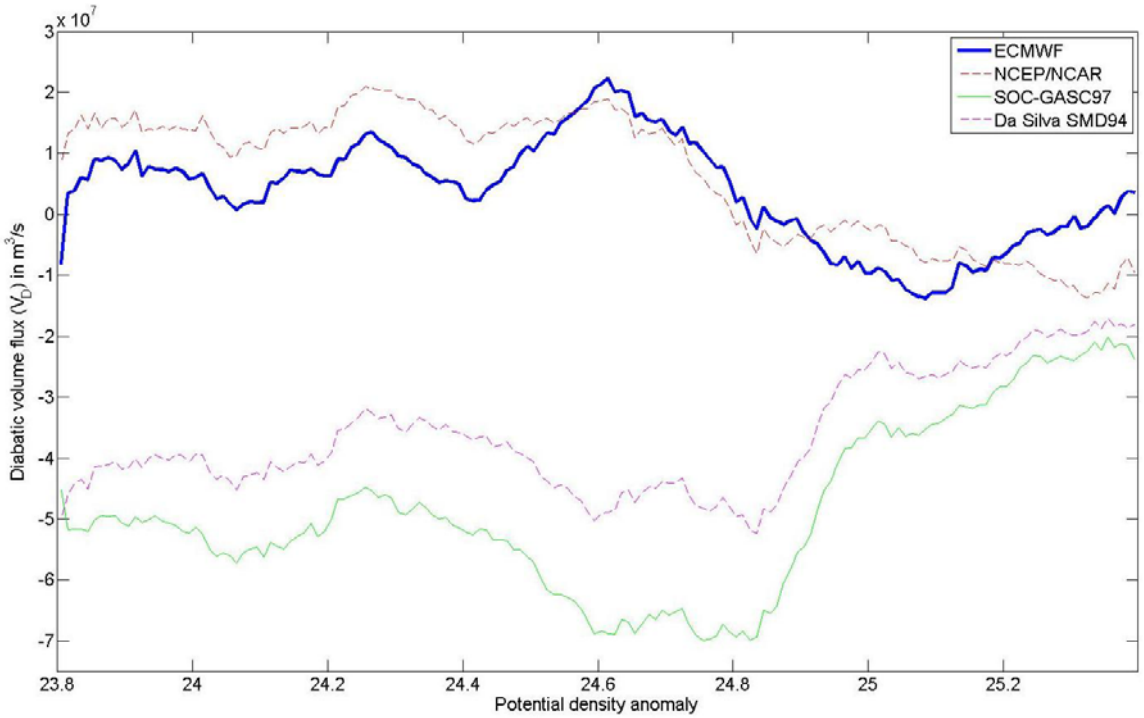

Figure 36. Diapycnal interior flux V_d in the Pacific Ocean computed from the four meteorological databases.

Again, we observe large discrepancies among V_d estimates from the different databases, although results from ECMWF and NCEP/NCAR re-analyses show many similarities. Concerning SOC-GASC97 and Da Silva SMD94 climatologies, the results are again unrealistic, which is most likely due to the lack of observational data for the southern ocean.

The V_d profiles for the combined Indian-Pacific Ocean are close to those for the Pacific Ocean only. As shown in Fig. 37, the major difference is in the value of the diapycnal interior flux, which increases by 13 *Sv* (ECMWF climatology) when the Indian Ocean is taken into account. This implies that the Indian Ocean contribution to $V_d(\sigma)$ is almost constant (about 13 *Sv*) over the sigma range [23.8, 25.4].

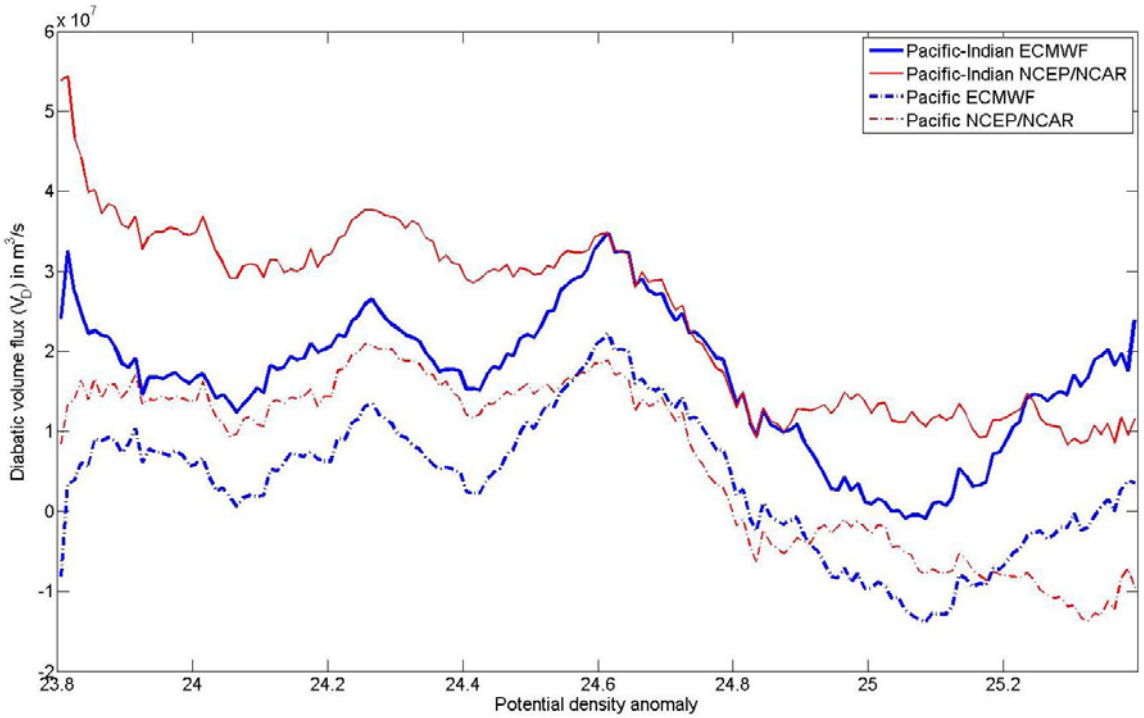

Figure 37. Comparison of the diapycnal interior flux V_d in the Pacific Ocean and in the combined Indian-Pacific Ocean. The values are computed from ECMWF and NCEP/NCAR databases.

2. Adiabatic Advection

Figure 38 shows $V_a(\sigma)$ computed from Eqs. (21), (25), and (27) using the four meteorological databases. In a similar way as in the upper Atlantic calculations, $V_a(\sigma)$ represents here the integrated isopycnal interior flux over the potential density anomaly range $[\sigma_0, \sigma]$. Thus, $\frac{\partial V_a}{\partial \sigma} > 0$ means a northward flux, and $\frac{\partial V_a}{\partial \sigma} < 0$ corresponds to a southward flux.

The integrated isopycnal flux V_a, calculated from ECMWF (reference climatology), is negative over most of the σ range [23.8, 25.4]. This indicates that the residual flow in the Pacific upper thermocline is predominantly southward, with a mean value of -8.6 *Sv*. The differences in $V_a(\sigma)$ computed from the various databases are not as large as in $V_d(\sigma)$, which is consistent with our results for the Atlantic Ocean.

Contrary to the results in the Atlantic and global oceans, the comparison of the ispoycnal Ekman fluxes and the isopycnal residual (total) fluxes suggests that mechanical forcing (wind stress) is the major driving force for the MOC in the Pacific Ocean. Indeed, the Ekman flux dominates the residual flux, with the same sign and tendency, over almost the complete density range. Note that this statement is not valid for the combined Indian-Pacific basin.

The computations for the combined Indian-Pacific Ocean provide V_a profiles that are similar to those for the Pacific Ocean only. As shown in Fig. 39, we observe a nearly uniform Indian Ocean contribution to $V_a(\sigma)$ that is about 12 *Sv* over the entire sigma range [23.8, 25.4].

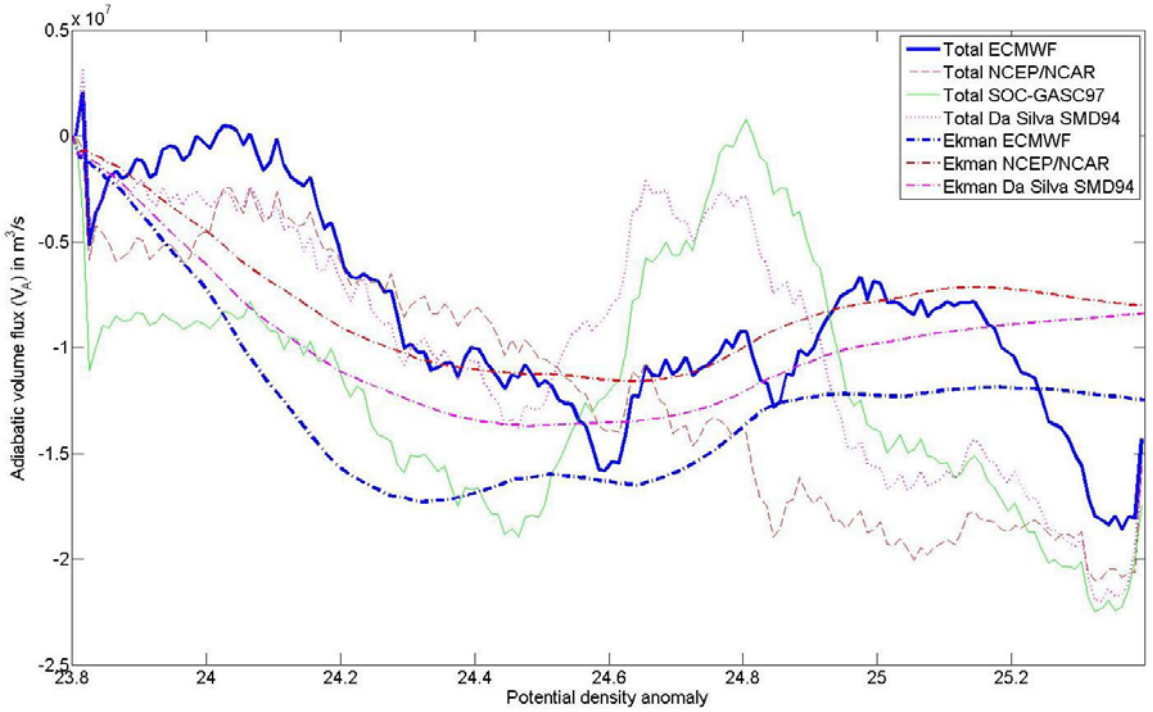

Figure 38. Adiabatic interior flux V_a in the upper Pacific Ocean computed from the four meteorological databases.

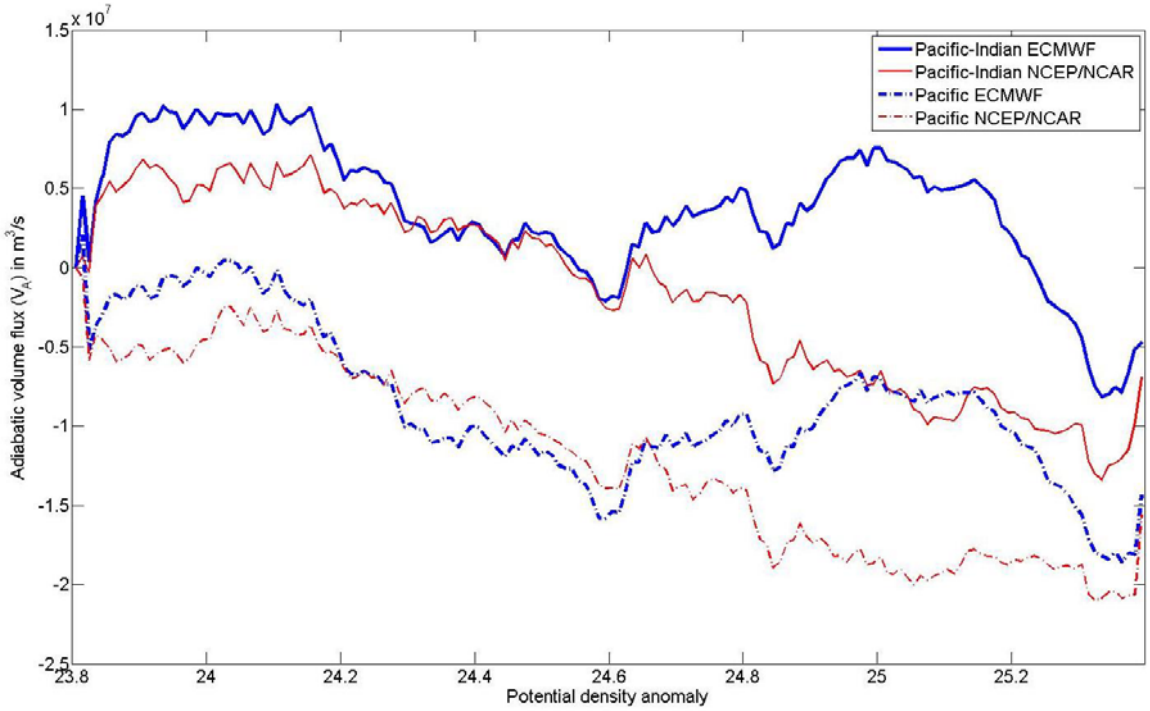

Figure 39. Comparison of the adiabatic interior flux V_a in the Pacific Ocean and in the combined Indian-Pacific Ocean. The values are computed from ECMWF and NCEP/NCAR databases.

3. Adiabatic Flux Ratio

Tables 8 and 9 give the adiabatic flux ratios respectively for the Pacific basin and the combined Indian-Pacific Ocean. This parameter is relatively low in the two oceans: $\gamma \approx 2.45$ (ECMWF computations) in only the Pacific Ocean and $\gamma \approx 1.47$ (ECMWF computations) when we also consider the Indian basin. This suggests that the meridional overturning is still controlled by the adiabatic processes (advection and eddy-transfer) in the Pacific thermocline, whereas it is mostly diabatic in the upper Indian Ocean.

Database	Adiabatic flux ratio γ (dimensionless)
ECMWF	2.4542
NCEP/NCAR	1.4346
SOC-GASC97	0.4461
Da Silva SMD94	0.5854

Table 8. Adiabatic flux ratios for the upper Pacific Ocean computed from the four meteorological databases.

Database	Adiabatic flux ratio γ (dimensionless)
ECMWF	1.4681
NCEP/NCAR	0.7260
SOC-GASC97	0.5042
Da Silva SMD94	0.5683

Table 9. Adiabatic flux ratios for the upper Indian-Pacific Ocean computed from the four meteorological databases.

4. Pacific and Indian Contributions to Global MOC

To estimate the Pacific and Indian contributions to the global thermohaline circulation, Figs. 40, 41, 42, and 43 display $V_d(\sigma)$ and $V_a(\sigma)$ in the Pacific and Indian-Pacific oceans over the density interval of [24.2, 28.3]. The chosen density range includes the southern ocean, where the volume flux of the ACC may result in external sources of water and might lead to uncertainties in V_d and V_a estimates.

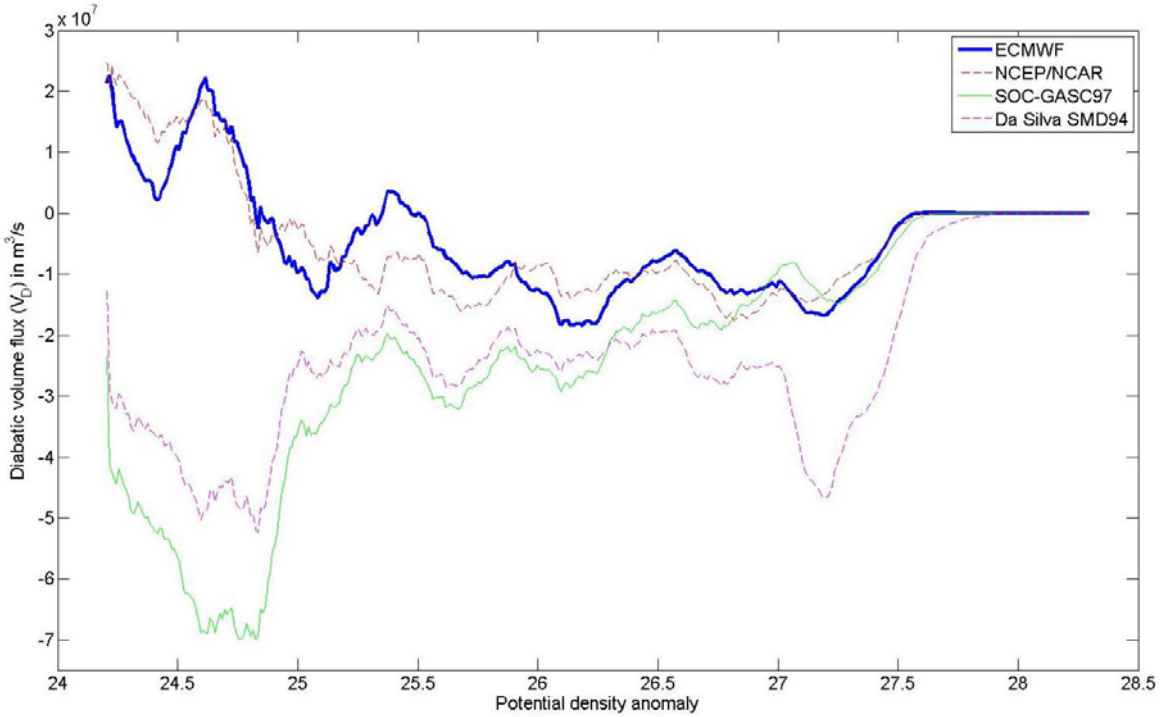

Figure 40. Diapycnal interior flux V_d in the entire Pacific Ocean computed from the four meteorological databases.

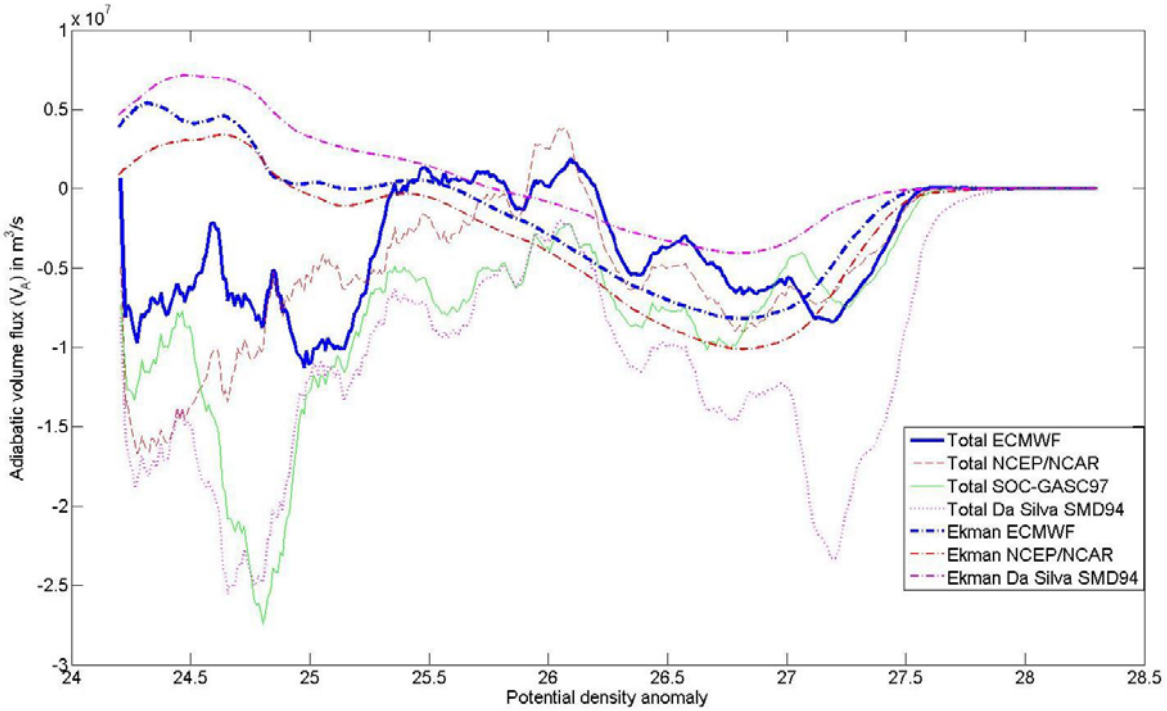

Figure 41. Adiabatic interior flux V_a in the entire Pacific Ocean computed from the four meteorological databases.

In Figs. 41 and 43, $V_a(\sigma)$ represents the integrated adiabatic advection over the density range $[\sigma, \sigma_{\max}]$. In Fig. 41, we see that V_a is dominated by the Ekman flux. Significant differences between V_a and V_{a-EK} occur only for the low densities $(\sigma < 25.3)$: this feature may be partially due to the external water sources in the southern ocean affecting the integrated flow $V_a(\sigma)$. The mechanical forcing (wind stress) also drives the MOC in the combined Indian-Pacific Ocean, except at low densities $(\sigma < 25.2)$. The Ekman flux dominates the residual flux, with the same tendency, over almost all the density range [25.2, 28.3].

The comparisons between Fig. 42 and Fig. 25 and between Fig. 43 and Fig. 27 indicate the large contribution of the density forcing over the Indian Ocean to the global MOC circulation (on both diabatic and adiabatic components). Indeed, the correlations between the global MOC components and those computed over the Pacific Ocean only are relatively low, whereas the same correlations with the combined Indian-Pacific Ocean instead of only the Pacific Ocean are much higher. This result is surprising, since the Indian Ocean is the smallest oceanic basin and its topography also inhibits any pole-to-pole MOC circulation.

Tables 8 and 9 give the adiabatic flux ratios respectively for the whole Pacific basin and the whole combined Indian-Pacific Ocean. Relatively high values of γ indicate that the adiabatic advection is also an important process in the Pacific and Indian Oceans. In particular, the isopycnal volume flux tends to dominate the MOC at high densities (southern ocean).

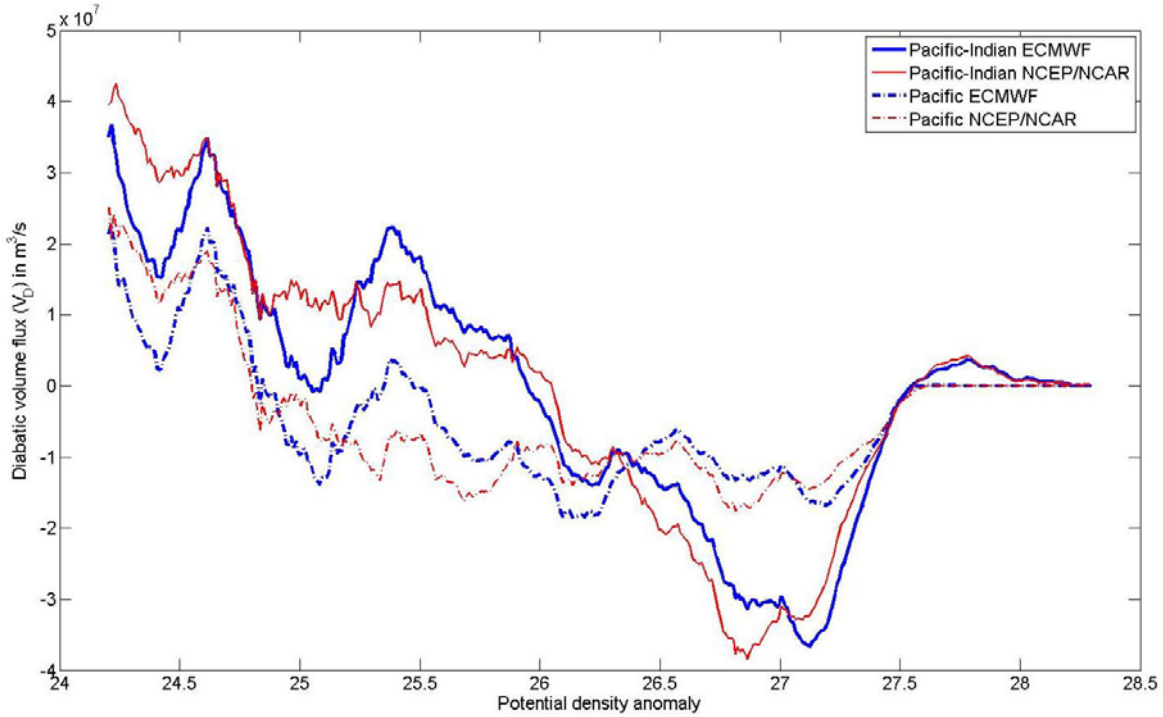

Figure 42. Comparison of the diapycnal interior flux V_d in the entire Pacific Ocean and in the combined Indian-Pacific Ocean. The values are computed from ECMWF and NCEP/NCAR databases.

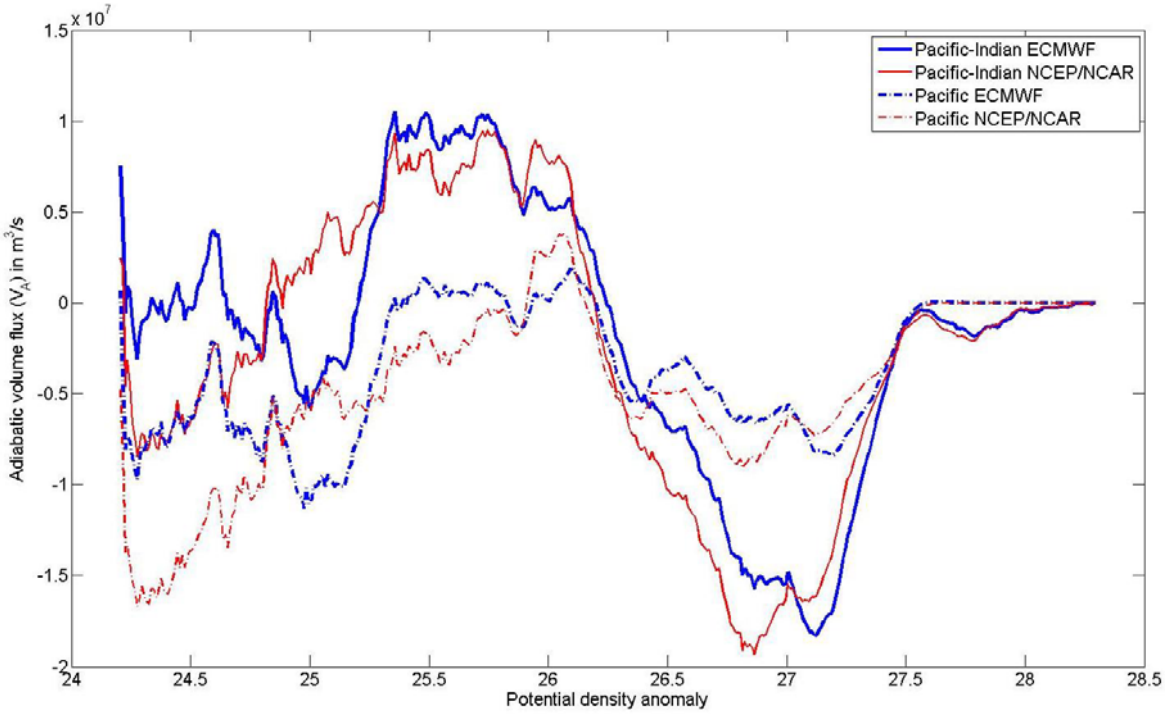

Figure 43. Same as Fig. 42, but for the adiabatic interior flux V_a.

Database	Adiabatic flux ratio γ (dimensionless)
ECMWF	2.5561
NCEP/NCAR	2.8388
SOC-GASC97	0.9889
Da Silva SMD94	1.6378

Table 10. Adiabatic flux ratios for the entire Pacific Ocean computed from the four meteorological databases.

Database	Adiabatic flux ratio γ (dimensionless)
ECMWF	3.0824
NCEP/NCAR	3.1211
SOC-GASC97	1.5104
Da Silva SMD94	2.3517

Table 11. Adiabatic flux ratios for the entire Indian-Pacific Ocean computed from the four meteorological databases.

D. CONSISTENCY OF THE ADIABATIC ADVECTION ESTIMATES

The isopycnal flux $V_a(\sigma)$ is defined by a linear average of two net residual fluxes at the bottom of the mixed-layer [Eq. (25)]. Since this assumption is a critical element of our method for estimating the residual overturning circulation, the formulation for V_a must be tested for consistency.

One way to test V_a estimates is to use an oceanic General Circulation Model (GCM). Indeed, the residual isopycnal advection diagnosed from the air-sea density fluxes can be compared with the V_a values derived directly from the GCM-simulated velocities.

1. Model Characteristics

The model used for this study is based on the GFDL MOM3 code (Pacanowski and Griffies 1999). Its horizontal resolution is two degrees in longitude and latitude. It

covers the whole ocean from 78°S to 84°N and is divided into 25 levels in the vertical direction, with its resolution increasing from 17 m at the surface layer to 510 m at the bottom. The bathymetry of the model is derived from the Scripps Topography. Vertical diffusivity varies from $0.25\text{x}10^{-4}\ m^2s^{-1}$ at the surface to $1.0\text{x}10^{-4}\ m^2s^{-1}$ at the bottom. This profile reflects the increase of the vertical mixing from the thermocline to the deep ocean (Bryan and Lewis 1979) and the intensification of mixing by rough bottom topography (Polzin et al. 1997). Heat and salt transports by mesoscale eddies are parameterized by the Gent-McWilliams scheme (Gent and McWilliams 1990) with coefficients for isopycnal diffusion of tracers and isopycnal thickness of $500\ m^2s^{-1}$. The K-profile parameterization (KPP) scheme (Large et al. 1994) is used to represent turbulent mixing within boundary layers.

The simulated density field at 40 m depth is given in Fig. 44a: due to the coarse resolution of the model, small differences with observations remain at high latitudes of the North Atlantic and in the ice-covered areas. Surface density fluxes are quantitatively consistent with observations, and the largest differences with the observational data appear in regions where the coarse resolution distorts simulations of the currents (at the equator, in the Western Boundary Current areas, and in the Antarctic Circumpolar Current region).

Heat fluxes into the ocean are determined by using conventional bulk formulas and are corrected for stability. Daily values for the two-meter air temperature and humidity, ten-meter wind speed, and zonal and meridional components of the wind stress have been taken from NCEP/NCAR reanalysis for the period of 1979-2001 and climatologic monthly means are used for all other atmospheric variables. Cloud cover and solar radiation are given by the International Satellite Cloud Climatology Project (ISCCP). Freshwater fluxes are taken from Jiang et al. (1999) and include river runoff data. The model is coupled to a thermodynamic sea-ice model (Visbeck et al. 1998).

For the analysis, the 1990 simulation has been chosen: it represents the mean year of the studied period and does not correspond to an El Nino/La Nina event. The density flux distribution computed from the model is given in Fig. 44b.

The MOC estimates provided by the model are generally coherent with the previous studies. In addition, density fluxes, stratification, and velocity fields in GCM-simulation are all dynamically consistent and readily available, which enables us to verify main assumptions of the theory in Section II.

2. Adiabatic Advection

The isopycnal flux has been estimated over the interval [24.4, 28]. This range is determined with the same criteria as those used in Section III-A-3: $\sigma_0 = 24.4$ is the lightest density anomaly whose outcrop forms two non-intersecting contours of surface density throughout the year, and $\sigma_{\max} = 28$ is the highest density of the ice-free sea surface area.

The adiabatic MOC component $V_a(\sigma)$ has been computed in two ways: (i) by using Eq. (26) to infer V_a from the sea-surface density flux, and (ii) by evaluating V_a directly from the meridional velocity distribution. More precisely, for the second calculation, we consider a zonal section exactly at the equator, and the isopycnal transport is obtained by vertically integrating the zonal residual flow (the sum of the Eulerian and eddy-induced velocities of the Gent-McWilliams scheme) starting from $\sigma_{\max}$ towards lighter densities. The sign convention in both calculations is the same as in Section IV-A-2.

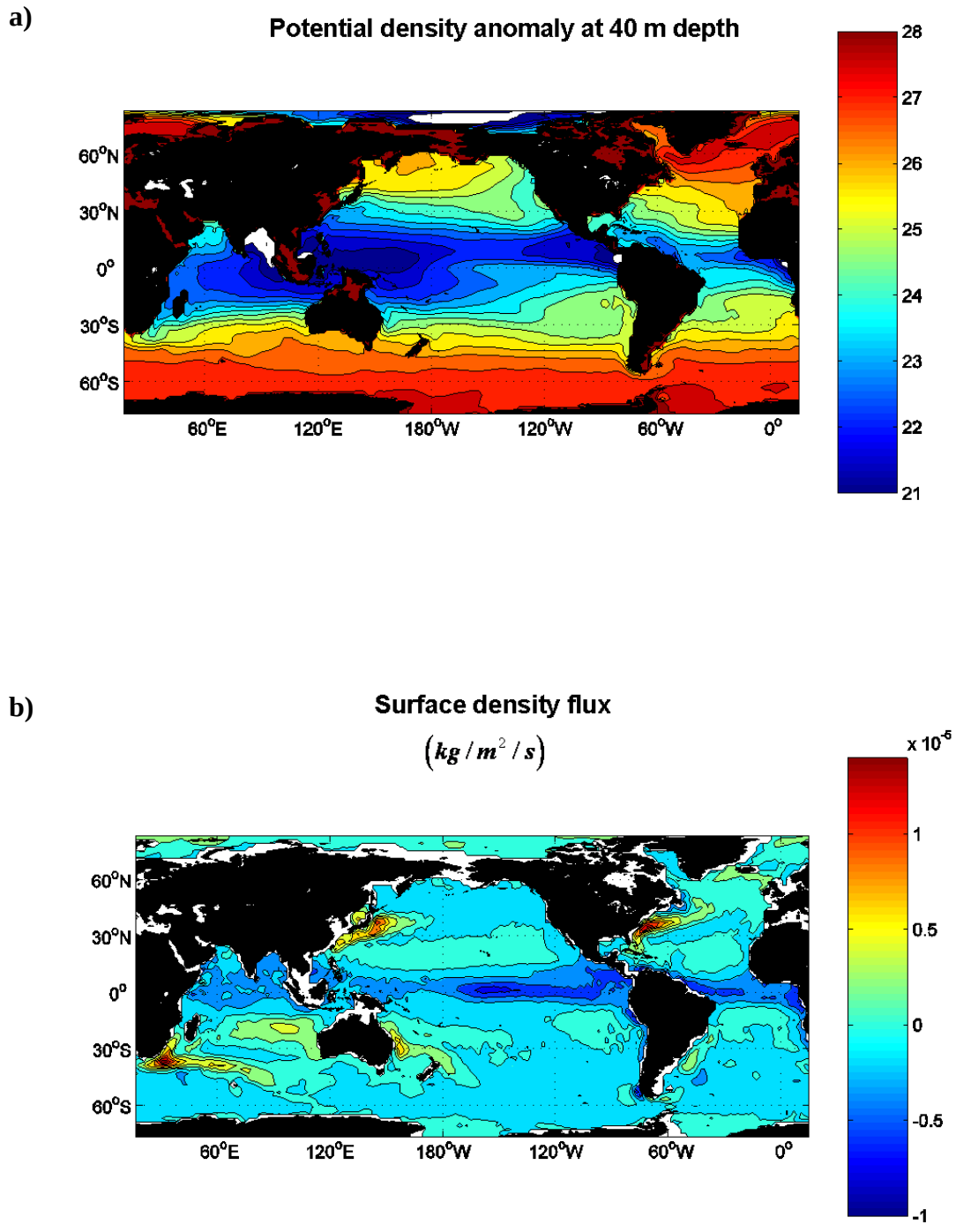

Figure 44. GCM-simulated fields. (a) Potential density anomaly distribution at 40 m depth. (b) Surface density flux from the atmosphere into the ocean (from Radko et al. 2006).

For the individual basin computations, the water mass transport from other basins has been taken into account. In particular, the ACC contribution has been calculated as a divergence of the zonal residual flow within the ACC between 64°W and 18°E, which are the longitudes of, respectively, the Drake Passage and Africa. Over the southern Atlantic area, we observe a negative divergence: this suggests some inflow of water from the ACC into the Atlantic Ocean. This ACC convergence has been incorporated into the V_S term of Eq. (25) for the Atlantic and Indian-Pacific calculations, and the corresponding V_a estimate has been modified accordingly.

Figures 45, 46, and 47 plot $V_a(\sigma)$ for the global ocean, the Atlantic and Indian-Pacific basins, respectively. On these plots, we see that the V_a profiles from the surface density flux (blue curves) and those obtained directly from the velocity distribution at the equator (green curves) match very well, especially for the global calculations. Although some significant differences occur at specific σ values, overall, the results in Figs. 45, 46, and 47 support the diagnostic model for estimating $V_a(\sigma)$, introduced in Section II-D [Eq. (25)].

For the global ocean case, the profile of the adiabatic MOC component computed from observations [Fig. 27] and that based on model calculations [Fig. 45] have many similarities. In particular, we observe on both profiles a positive peak value of 5 *Sv* at $\sigma \approx 25.7$ and a negative peak value at $\sigma \approx 27.1$ in Fig. 27 (observations) and at $\sigma \approx 27.3$ in Fig. 45 (model). However, the magnitude of $V_a(\sigma)$ computed from observations is generally higher than in the model. The V_a profile given by the model does not show any Gulf Stream signature (negative peak value at $\sigma \approx 25.35$), whereas it clearly appears on the observational V_a curve. This may be attributed to poor resolution of WBC Gulf Stream density field by the coarse-resolution GCM.

For the Atlantic Ocean computations, $V_a(\sigma)$ profiles from observations [Fig. 35] and GCM [Fig. 46] are quite similar, but, as mentioned above, they strongly differ at the Gulf Stream densities (around $\sigma = 25.35$).

$V_a(\sigma)$ profiles for the Indian-Pacific Ocean [Fig. 43 and Fig. 47] also show many similarities between the observations and the model output. Again, the magnitude is generally much higher for the climatologic estimates than for the GCM-based analysis.

Concerning the wind-driven component of $V_a(\sigma)$ (Ekman isopycnal flux), the model outputs are characterized by a much larger contribution of this component to the residual (total) isopycnal flux than the observational estimates. However, both the observational results and the model suggest that the local wind-stress forcing does not drive the residual MOC adiabatic advection in the Atlantic Ocean.

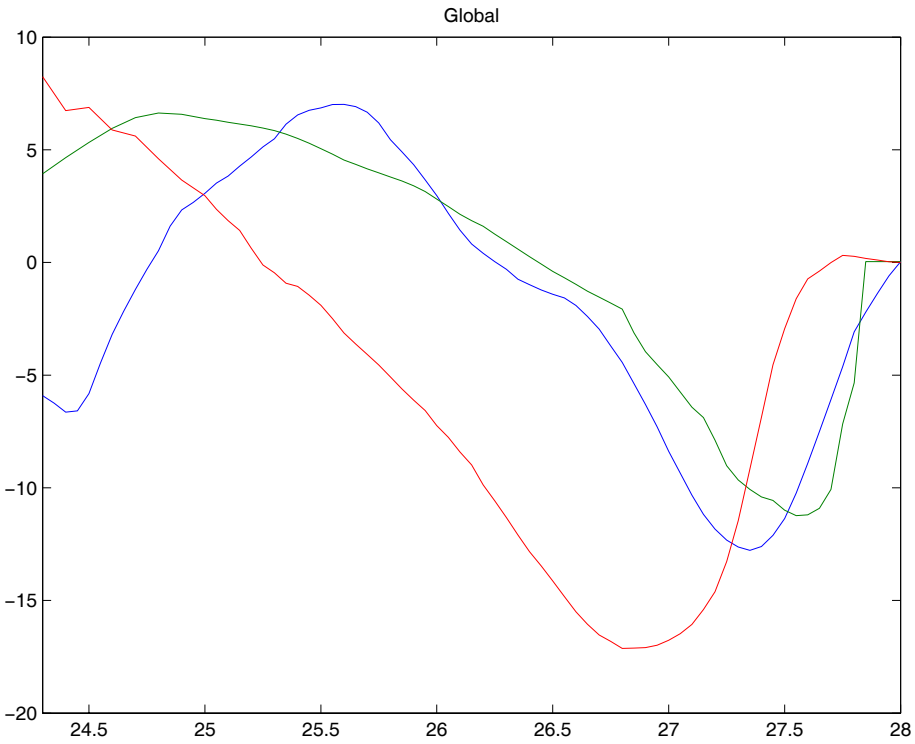

Figure 45. Adiabatic interior flux V_a in the global ocean computed from the GCM. The displayed values are in sverdrups (*Sv*). The blue curve represents $V_a(\sigma)$ computed from the simulated surface density flux. The green curve gives $V_a(\sigma)$ obtained directly from the velocity distribution at the equator. The red curve is the wind-driven component of $V_a(\sigma)$ (Ekman adiabatic interior flux) [from Radko et al. 2006].

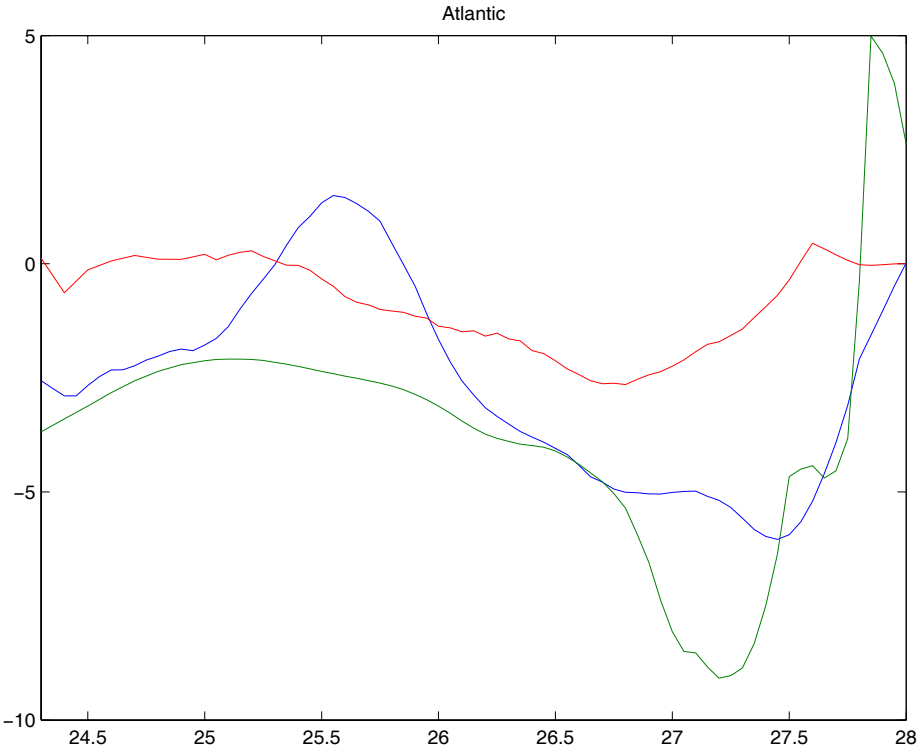

Figure 46. Same as Fig. 45, but for the Atlantic Ocean.

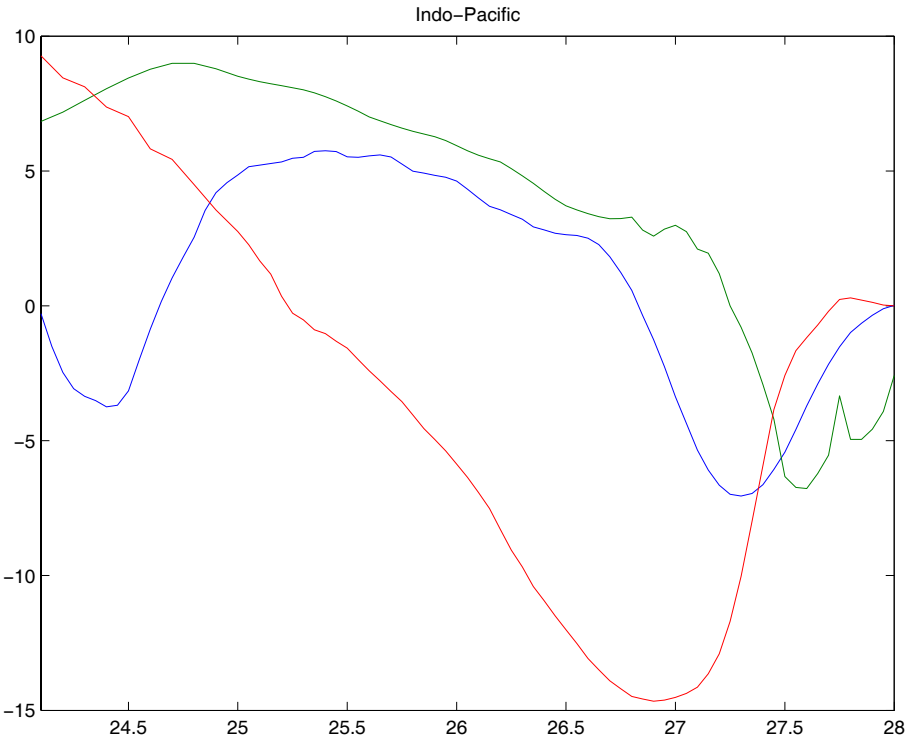

Figure 47. Same as Fig. 45, but for the Indian-Pacific Ocean.

V. DISCUSSION AND CONCLUSIONS

The oceanic Meridional Overturning Circulation (MOC) is accompanied by the diabatic transformation of water masses and interacts with the air-sea buoyancy fluxes (Walin 1982). The two major mechanisms for water mass transformation are the interior diapycnal diffusion and the diabatic processes in the upper mixed-layer. Their relative importance is still uncertain and much debated. The classical view (e.g., Robinson and Stommel 1959; Munk 1966) emphasizes the water mass transformation in the ocean interior and implicitly assigns it a critical role in maintenance of the meridional overturning. This idea was challenged by a number of modeling studies (e.g., Bryan 1987), which demonstrate that reproducing overturning of realistic strength via diffusive mechanisms requires unrealistically high values of vertical mixing. Mechanical forcing by winds, on the other hand, appears to be an essential ingredient of the thermohaline system; neglecting the wind stress in multi-century simulations, for instance, leads to a complete shutdown of the conveyor belt circulation (Timmermann and Goosse 2004). These findings suggest that the interior diffusion may not be as critical for maintenance of the MOC as adiabatic processes (wind forcing, advection, and eddy transfer). This latter statement has gained considerable attention recently (Toggvieler and Samuels 1998; Marshall and Radko 2003; Radko 2006), but requires independent and objective support.

The diagnostic analysis in this study may help to resolve this dispute by quantifying the magnitude and distribution of the isopycnal MOC component (V_a) and relating it to the surface forcing fields. While the isopycnal transport is not reflected in the interior water mass transformation, it interacts with the diabatic mixed-layer, making it possible to infer its pattern directly from the sea surface data. The theoretical framework is based on the residual mean theory that takes into account adiabatic transfer by the geostrophic eddies. As indicated in the schematic diagram in Fig. 6b, each density layer in our model can be thought of as a “leaky pipe” that is connecting the two hemispheres and is pumped at its two ends with different forces. It is this difference in

pumping that ultimately determines the direction and the average transport of the flow through the pipe, although a certain amount of water "leaks" in the interior due to diabatic processes.

This study is mainly focused on the along-isopycnal volume flux V_a, representing the adiabatic advection within a specific density layer. $V_a(\sigma)$ has been defined as the linear average of the two net residual fluxes at the bottom of the mixed-layer in the Northern and Southern hemispheres. Moreover, considerable attention is given to properties of the diapycnal flux $V_d(\sigma)$, representing the integrated flux across the isopycnal surface σ in the ocean interior. Since the residual flow is assumed to be non-divergent, it is exactly equal to the net volume flux from the ocean interior into the mixed-layer within the area defined by the mixed-layer density condition $\sigma_m < \sigma$.

In addition to the computations of the adiabatic and diabatic interior fluxes, the adiabatic flux ratio defined in Eq. (28) has been used to determine the dominant component of the MOC. This parameter appears to represent accurately the relative strength of the two components by considering the averages of the volume fluxes. However, it is very sensitive to the accuracy of the observational fields and also to the considered density range. For this reason, the values of the adiabatic flux ratio γ must be interpreted with caution.

For the Atlantic, our results show that along-isopycnal volume fluxes greatly exceed the corresponding diapycnal transport ($\gamma \approx 4.11$ for ECMWF climatology). These findings support the notion that the dynamics of the meridional overturning in the Atlantic Ocean are dominated by the adiabatic processes (advection and eddy-transfer). For the Pacific, the analysis suggests that the effects of the water mass transformation and along-isopycnal advection are mostly comparable ($\gamma \approx 2.56$ for ECMWF climatology). For the global ocean, the results suggest that the global thermohaline circulation is dominated by the adiabatic advection ($\gamma \approx 3.50$ for ECMWF climatology).

In addition to quantifying the strengths of the MOC components, this study offers some insight into the mechanics of the pole-to-pole meridional overturning. The total

along-isopycnal residual circulation (V_a) is divided into two distinct components: the mean advection (V_{a-EK}), also called the wind-driven component of V_a, and the eddy-driven component. The GCM results point out that V_a is controlled by the mean advection, directly associated with the Ekman pumping, everywhere except in the Atlantic Ocean. On the contrary, the observational results show that the Ekman advection is comparatively weak and not correlated with the residual adiabatic advection, except in the Pacific Ocean; this emphasizes the global dominance of the eddy-driven advection in the adiabatic interior flux.

It is also essential to keep in mind that the application of the water mass transformation theory to the sea surface data is greatly restricted by the observational uncertainties: the air-sea fluxes in various datasets may differ by as much as a factor of two or more. However, this limitation is not nearly as severe for the isopycnal MOC component (V_a) as it is for the diapycnal flux (V_d). V_a estimates are based on the difference between the air-sea fluxes at the Northern and Southern outcrops of each isopycnal surface. Therefore, for $V_a(\sigma)$ computations, our method results in a partial cancellation of systematic errors in flux measurements. In fact, the four climatologic databases (ECMWF, NCEP/NCAR, SOC-GASC97, and Da Silva SMD94) are mutually consistent in terms of predicting the isopycnal transport V_a.

Several databases have been used in this study: Levitus 94 for the oceanic parameters, ECMWF, NCEP/NCAR, SOC-GASC97, and Da Silva SMD94 for the air-sea fluxes. This has permitted a quality control of the results and an assessment of the sensitivity of the calculations to the observational fields. Furthermore, the computations based on GCM-simulated parameters has validated our method of estimating the adiabatic interior flux $\left(V_a(\sigma)\right)$.

Statistical calculations in this study offer suggestions for the database selection and for the optimal choice of the operational parameters in diagnostic models. In particular, the mixed-layer density here is represented by the potential density anomaly at 40 m depth, and ECMWF re-analysis appears to be the best compromise regarding the accuracy of fluxes at the sea surface.

Finally, this study offers new insights into mechanics of the thermohaline circulation and its interaction with the atmosphere. These insights are supported by an agreement (Section IV) between our results and the corresponding estimates of the oceanic circulation from in-situ measurements and from the earlier Walin-type diagnostic calculations (Donners et al. 2005).

LIST OF REFERENCES

Aguado, E., and J.E. Burt, 2005: *Understanding Weather and Climate*, 4th Ed., Prentice-Hall, 560pp.

Andrews, D. G., and M. E. McIntyre, 1976: Planetary waves in horizontal and vertical shear: the generalized Eliassen-Palm flux and the mean zonal acceleration. *J. Atmos. Sci.*, **33**, 2031-2049.

Boccaletti G., R. Ferrari, D. Ferreira, A. Adcroft, and J. Marshall, 2005: The vertical structure of the oceanic heat transport. *Geophys. Res. Lett.*, **32**, L10603, 1-4.

Bromwich, D. H., and R. L. Fogt, 2004: Strong trends in the skill of the ERA-40 and NCEP/NCAR reanalyses in the high and midlatitudes of the Southern Hemisphere, 1958-2001. *J. Climate*, **17**, 4603-4619.

Bryan, F., 1987: Parameter sensitivity of primitive equation ocean general circulation models. *J. Phys. Oceanogr.*, **17**, 970-985.

Bryan, K., and L.J. Lewis, 1979: A water mass model of the world ocean. *J. Geophys. Res.*, **84**, 2503-2517.

Donners, J., S. S. Drijfhout, and W. Hazeleger, 2005: Water mass transformation and subduction in the South Atlantic. *J. Phys. Oceanogr.*, **35**, 1841-1860.

Edwards, C. A., and J. Pedlosky, 1998: Dynamics of nonlinear cross-equatorial Flow. Part I: Potential Vorticity Transformation. *J. Phys. Oceanogr.*, **28**, 2382-2406.

Gent, P.R., and J.C. McWilliams, 1990: Isopycnal mixing in ocean circulation models. *J. Phys. Oceanogr.*, **20**, 150-155.

Gnanadesikan, A., 1999: A simple predictive model for the structure of the oceanic pycnocline. *Science*, **283**, 2077-2079.

Henning, C. C., and G. Vallis, 2004: The effects of mesoscale eddies on the main subtropical thermocline. *J. Phys. Oceanogr.*, **34**, 2428-2443.

Jiang, S., P. H. Stone, and P. Malanotte-Rizzoli, 1999: An assessment of the Geophysical Fluid Dynamics Laboratory ocean model with coarse resolution: Annual-mean climatology. *J. Geophys. Res.*, **104**, 25623-25645.

Josey, S., E. Kent, and P. Taylor, 1999, New insights into the ocean heat budget closure problem from analysis of the SOC air-sea flux climatology. *J. Climate*, **12**, 2856-2880.

Karsten, R., and J. Marshall, 2002: Constructing the residual circulation of the ACC from the observations. *J. Phys. Oceanogr.*, **32**, 3315-3327.

Large, W.G., J.C. McWilliams, and S.C. Doney, 1994: Oceanic vertical mixing: A review and a model with a nonlocal boundary layer parameterization. *Rev. Geophys.*, **32**, 363-403.

Ledwell, J. R., A. J. Watson, and C. S. Law, 1993: Evidence for slow mixing across the pycnocline from an open ocean tracer-release experiment. *Nature*, **364**, 701-703.

Luyten, J., J. Pedlosky, and H. Stommel, 1983: The ventilated thermocline. *J. Phys. Oceanogr.*, **13,** 292-309.

Marshall, J., H. Jones, R. Karsten, and R. Wardle, 2002: Can eddies set ocean stratification? *J. Phys. Oceanogr.*, **32,** 26-38.

Marshall, J., and T. Radko, 2003: Residual-mean solutions for the Antarctic Circumpolar Current and its associated overturning circulation. *J. Phys. Oceanogr.*, **33**, 2341-2354.

Munk, W., 1966: Abyssal recipes. *Deep Sea Res.*, **13**, 707-730.

Munk, W., and C. Wunsch, 1998: Abyssal recipes II: Energetics of tidal and wind mixing. *Deep-Sea Res.*, **45A,** 1977-2010.

Pacanowski, R. C., and S. M. Griffies, 1999: MOM 3.0 manual. Documentation user's guide and reference manual, NOAA/Geophysical Fluid Dynamics Laboratory, Princeton, NJ.

Polzin, K.L., J.M. Toole, J.R. Ledwell, and R.W. Schmitt, 1997: Spatial variability of turbulent mixing in the abyssal ocean. *Science*, **276**, 93-96.

Radko, T., and J. Marshall, 2004: Eddy-induced diapycnal fluxes and their role in the maintenance of the thermocline. *J. Phys. Oceanogr.*, **34**, 372-383.

Radko, T., and J. Marshall, 2006: The Antarctic Circumpolar Current in three dimensions. *J. Phys. Oceanogr.*, **36**, 651-669.

Radko, T., 2006: A mechanism for establishment and maintenance of the meridional overturning in the upper ocean. *J. Mar. Res.*, **65**, in press.

Radko, T., P.-Y. Daré, and I. Kamenkovitch, 2006: Inferring the isopycnal component of the meridional overturning from the air-sea fluxes. *J. Phys. Oceanogr.,* To be submitted.

Robinson, A. R., and H. Stommel, 1959: The oceanic thermocline and the associated thermohaline circulation. *Tellus,* **11,** 295-308.

Roemmich, D. and C. Wunsch, 1985: Two transatlantic sections: Meridional circulation and heat flux in the subtropical North Atlantic Ocean. *Deep-Sea Res.*, **32**, 619–664.

Samelson, R. M., 2004: Simple mechanistic models of middepth meridional overturning. *J. Phys. Oceanogr.*, **34**, 2096-2103.

Schmitt, R. W., P. S. Bogden, and C. E. Dorman, 1989: Evaporation minus precipitation and density fluxes for the North Atlantic. *J. Phys. Oceanogr.*, **19,** 1208-1221.

Speer, K., and E. Tziperman, 1992: Rates of water mass formation in the North Atlantic Ocean. *J. Phys. Oceanogr.*, **22,** 93-104.

Speer, K., H.-J. Isemer, and A. Biastoch, 1995: Water mass formation from revised COADS data. *J. Phys. Oceanogr.*, **25,** 2444-2457.

Speer, K., S.R. Rintoul, and B. Sloyan, 2000: The diabatic Deacon cell. *J. Phys. Oceanogr.*, **30**, 3212-3222.

Stommel, H., 1961: Thermohaline convection with two stable regimes of flow. *Tellus*, **13,** 244-230.

Talley, L., 2003: Shallow, intermediate and deep overturning components of the global heat budget. *J. Phys. Oceanogr.*, **33,** 530-560.

Timmermann, A. and H. Goosse., 2004: Is the wind stress forcing essential for the meridional overturning circulation? *Geophys. Res. Lett.*, **31**, L04303.

Toggweiler, J. R., and B. Samuels, 1998: On the ocean's large-scale circulation near the limit of no vertical mixing. *J. Phys. Oceanogr.*, **28**, 1832-1852.

Toole J.M., K.L. Polzin and R. W. Schmitt, 1994: Estimates of diapycnal mixing in the abyssal ocean. *Science*, **264**, 1120-1123.

Trenberth, K. E., and J. M. Caron, 2001: Estimates of meridional atmosphere and ocean heat transports. *J. Climate*, **14**, 3433-3443.

Tziperman, E., 1986: On the role of interior mixing and air–sea fluxes in determining the stratification and circulation of the oceans. *J. Phys. Oceanogr.*, **16,** 680-693.

Visbeck, M., H. Cullen, G. Krahmann, and N. Naik, 1998: An ocean model's response to North Atlantic Oscillation-like wind forcing. *Geophys. Res. Lett.*, **25**, 4521-4524.

Walin, G., 1982: On the relation between sea-surface heat flow and thermal circulation in the ocean. *Tellus*, **34,** 187-195.

Webb, D. J., and N. Suginohara, 2001: Vertical mixing in the ocean. *Nature*, **409,** 37.

Welander, P., 1986: Thermohaline effects in the ocean circulation and related simple models. In *Large-Scale Transport Processes in Oceans and Atmosphere*, ed. J.
Whitehead, J. A., 1995: Thermohaline ocean processes and models. *Annu. Rev. Fluid Mech.*, **27**, 89-113.

Wunsch, C., and R. Ferrari, 2004: Vertical mixing, energy, and the general circulation of the oceans. *Ann. Rev. Fluid. Mech.*, **36**, 281-314.

INITIAL DISTRIBUTION LIST

1. Defense Technical Information Center
   Ft. Belvoir, Virginia

2. Dudley Knox Library
   Naval Postgraduate School
   Monterey, California

3. Timour Radko
   Department of Oceanography
   Naval Postgraduate School
   Monterey, California

4. Qing Wang
   Department of Meteorology
   Naval Postgraduate School
   Monterey, California

5. Mary L. Batteen
   Department of Oceanography
   Naval Postgraduate School
   Monterey, California

6. Philip A. Durkee
   Department of Meteorology
   Naval Postgraduate School
   Monterey, California

7. Tom Murphree
   Department of Meteorology
   Naval Postgraduate School
   Monterey, California

8. Albert Le Roux
   Centre Militaire d'Océanographie
   Service Hydrographique et Océanographique de la Marine
   Brest, France

9. Yves Morel
   Centre Militaire d'Océanographie
   Service Hydrographique et Océanographique de la Marine
   Toulouse, France